CHAPTER

10

Two Optical Techniques Sensitive to Gradients of Optical Path Difference: The Method of Caustics and the Coherent Gradient Sensor (CGS)

Ares J. Rosakis

Graduate Aeronautical Laboratories
California Institute of Technology
Pasadena, CA 91125

General Introduction

In this chapter we discuss two optical techniques [caustics and coherent gradient sensor (CGS)] sensitive to gradients of optical path difference. In solid mechanics applications both caustics and CGS provide measures of in-plane gradients of out of plane displacements (reflection) or in-plane gradients of stresses (transmission).

The physical principles governing the two methods are presented and their remarkable similarities are discussed in detail. The applicability of the two methods in the experimental study of both elastic and elastic-plastic fracture problems is investigated. Particular attention is paid to the elastodynamic fracture applications of both methods. This preference is motivated by the fact that both techniques are ideal candidates for use in conjunction with high-speed photography. Indeed both CGS and caustics do not suffer from severe light loss problems that may be detrimental when exposure times of the order of nanoseconds are required. In addition, both methods involve relatively simple experimental arrangements and minimal specimen preparation.

The chapter also concentrates in the limitations associated with the interpretations of caustics and CGS patterns. The classical interpretation of op-

tical patterns on the basis of the assumptions of either K_I^d dominance or J dominance is critically discussed and its limitations are analyzed in great detail. For linear elastic solids, these limitations include the effect of near-tip three dimensionality as well as the negative influence of transient effects on the establishment of K_I^d dominant regions surrounding the near-tip three-dimensional zone. By relaxing the assumptions of K_I^d dominance and steady state, we present alternative means of extracting fracture parameters from both caustics and CGS.

Finally, we present experimental evidence, obtained by means of both methods, that lead to the following general conclusion regarding experimental dynamic crack growth studies:

Contrary to conventional wisdom, K_I^d dominance in the vicinity of dynamically propagating cracks appears to be the exception rather than the rule. It is thus critically important that interpretation of experimental data under assumed K_I^d-dominance, steady-state, or two-dimensional conditions be carefully justified prior to attributing physical credence to the observed phenomena.

A.1 Introduction (Caustics)

The optical method of caustics is a widely used technique in experimental solid mechanics. In the area of fracture mechanics, in particular, it has been one of the primary tools of investigation of both quasistatic and catastrophic failure, starting with the pioneering works of Manogg [1,2], and continuing over the years through the efforts of Theocaris and co-workers [3–11], Kalthoff and co-workers [12–18], Rossmanith [19-24], Zhang and Ravi-Chandar [25], Ravi-Chandar and Knauss [26], and Rosakis and co-workers, [27–38] among others. Extensive reviews of the subject have been provided by Theocaris [7] and Kalthoff [18]. Also, a special issue of the *International Journal of Lasers and Optics in Engineering* [39] has been devoted to caustics and provides a snapshot of current research applications of the technique.

The technique has several advantages over other optical methods which are mainly related to its simplicity. It requires a simple optical experimental setup which does not involve the use of diffraction optics. It can be used easily either in transmission or in reflection modes. Data analysis is simple and does not require the use of complicated image processing techniques. The simplicity of the technique makes it an ideal candidate for high-speed photography applications. In particular, the fact that the physical principle of caustics does not hinge on the availability of a coherent, monochromatic light source has allowed for the use of high-speed camera systems, which utilize white light illumination (for example, spark gap cameras of the Cranz–Schardin type). In addition, the lack of complicated optical compo-

nents, such as diffraction gratings, beam splitters, etc., in a caustics setup ensures minimal light intensity losses which are crucial for successful high-speed photography. Indeed, in such applications, light intensity is of the essence since the exposure times involved are often very short (of the order of nanoseconds).

As currently used in fracture studies, the method of caustics is subject to two sets of simplifying assumptions, one in the analysis of the optical technique and the other regarding the nature of the mechanical fields under study. The limitations introduced by the simplifications in the optical analysis of the method of caustics as well as an exact geometrical optics interpretation of the technique are discussed in Rosakis and Zehnder [33]. It turns out that the simplified analysis deviates from the exact geometrical analysis in only relatively extreme regimes, and, for the most part, the simplified optical analysis is adequate. The corresponding issue regarding the assumptions made about the mechanical fields under study, however, is more troublesome. Typically, interpretation of caustics data in fracture mechanics is done under the assumption that crack-tip deformation is well described by two-dimensional, steady-state, asymptotic models. To the extent that these assumptions are violated in a laboratory specimen, caustics data are prone to misinterpretation and error.

In this section, we shall describe the method as is currently used in elastostatic, elastodynamic and elastic-plastic fracture studies, with particular emphasis given to the approximations involved. We will then review some of the attempts that have been made in the recent past toward rectifying errors incurred due to such approximations. We will start by considering the effect of crack-tip three dimensionality on the analysis of the optical patterns. We will also discuss the possible inadequacy of asymptotic descriptions of crack-tip deformation. For dynamic crack growth studies in particular, we will discuss the shortcomings of the classical interpretation of caustics which is based on the assumption of K_I^d dominance. It will be demonstrated that the assumptions regarding the dynamic crack-tip mechanical fields, under which interpretation of caustics data is customarily made is a potential source of large errors especially in the presence of highly transient crack-tip motion histories (initiation, arrest, interreaction with stress waves, etc.). An analysis of dynamic caustic patterns utilizing a transient, higher-order description of near-tip mechanical fields will also be presented. In conclusion, the use of caustics for the measurement of the J integral in elastic plastic fracture applications will be discussed.

A.2 The Physical Principle

In the original work on transmitted caustics by Manogg [1], there exists implicit assumptions which limit the applicability of the results. These assump-

tions have been carried through in most of the subsequent application of the technique with very little or no explanation. In this section, the exact equations of the optical mapping will be derived and the approximations that appear in the caustics literature will be discussed in detail.

Consider a plate specimen of uniform thickness in the undeformed state. Let its middle cross section occupy the x_1, x_2 plane of an orthonormal Cartesian coordinate frame $\{0; x_1, x_2, x_3\}$. The specimen is such that it causes nonuniform gradients in the optical path when light is transmitted through it, or reflected from its surface. For a plate specimen made of a transparent material, the gradients in the optical path are due to nonuniform gradients in the thickness of the plate and also due to gradients in the refractive index of the material in the specimen interior. For a specimen made of an opaque material, the gradients in optical path are only due to nonuniform surface elevations of the plate. In experimental solid mechanics, both gradients of refractive index and thickness are related to gradients in the stress state which are induced when loads are applied to the boundary of the initially undeformed plate.

Consider further, a coherent light bundle traveling in the $-x_3$ direction normally incident on the plate as illustrated in Fig. 10.1. This is equivalent to a family of plane waves incident on the plate. A light ray is parallel to the vector normal to a surface representing wave fronts of light. If $S(x_1, x_2, x_3)$ represents the optical path of the light ray, then the wave front is given by $S(x_1, x_2, x_3) = \text{const}$. The vector $\nabla S(x_1, x_2, x_3)$, where ∇ is the three-dimensional gradient operator, is normal to S, and thus is parallel to the ray passing through S at point (x_1, x_2, x_3). For a specimen made of a transparent material, the plane waves travel through the material and are distorted due to the introduced variations in optical path (stress induced refractive index and plate thickness gradients). This causes light rays passing through the material to be deflected. (Equivalently waves reflected from the surface of a plate made of an opaque material are distorted due to stress induced nonuniform surface elevations.)

As will be seen later, under certain conditions (e.g., certain specimen deformation states) the reflected or refracted rays will form an envelope in the form of a three-dimensional surface in space. This surface, which is called the *caustic surface*, is the locus of points of maximum luminosity in the reflected or transmitted light fields.

The deflected rays are tangent to the caustic surface. If a screen it positioned parallel to the $x_3 = 0$ plane, and so that it intersects the caustic surface, then the cross section of the surface can be observed on the screen as a bright curve (the *caustic curve*) bordering a dark region (the *shadow spot*) on the screen. The etymology of the word *caustic* (surface or curve) comes from the Greek Καυστικος, "burning," so called because it denotes the locus of maximum concentration of luminous and thus heating effects.

Consider now a screen placed at a distance z_0 behind the underformed specimen position. The light ray intersecting the plate at the point $\mathbf{x} = (x_1,$

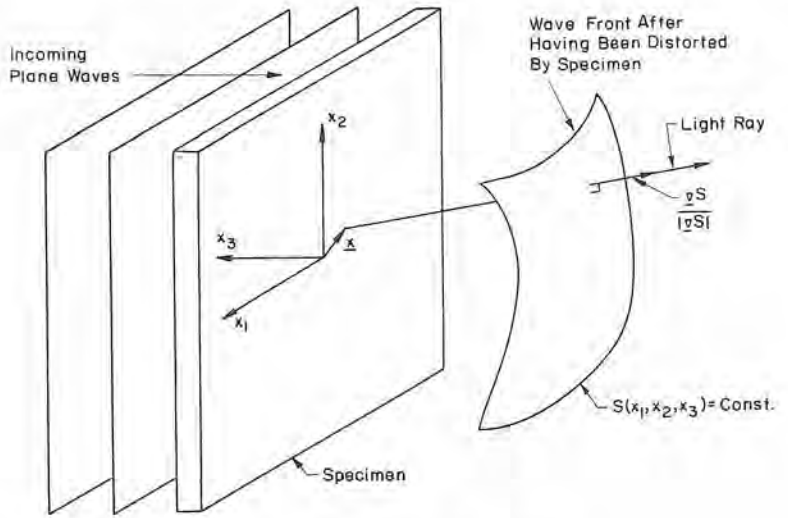

Figure 10.1. Deflection of light by transparent specimen.

x_2) on the specimen, will be mapped on to a point $\mathbf{X} = (X_1, X_2)$ on the screen. The X_1, X_2 coordinate system is identical to the (x_1, x_2) system, except that the origin of the former has been translated by $x_3 = -z_0$, $z_0 \geq 0$. Assuming that the specimen is of infinitesimal thickness and using the geometry of Fig. 10.2, we see that the mapping is given by

$$\mathbf{X} = \mathbf{x} - z_0 \left(\frac{\nabla S(x_1,x_2,0)}{\nabla S(x_1,x_2,0)\cdot \mathbf{e}_3} - e_3 \right), \tag{1}$$

where e_3 is the unit vector along the x_3 axis.

In the original work by Manogg [1], it was assumed that S is described by a family of self-similar surfaces translated in the $-x_3$ direction as in Fig. 10.3. Thus, according to his assumption, S is given by

$$S(x_1,x_2,x_3) = -x_3 - \Delta s(x_1,x_2) = \text{const.}, \tag{2}$$

where $\Delta s(x_1,x_2)$ represents the change in optical path introduced by the plate. The limitations of this assumption become evident if a light ray is followed from a surface S_1 to another, S_2, as in Fig. 10.3. The light ray parallel to the vector normal to S_1 at point P_1 intersects S_2 at P_2. However, the normal at P_2 is not parallel to the normal at P_1 and thus does not coincide with the direction of the light ray. Only for very small angles of deflection, will the normal at P_2 be parallel to the normal at P_1. Thus Manogg's assumption implicitly limits the applicability of his results to *small* ray deflections. As is evident from Fig. 10.4, the wave fronts are actually a family of expanding waves, resulting in light rays which are always normal to the surface. For vary large radii of curvature, i.e., very small deflections, expanding and

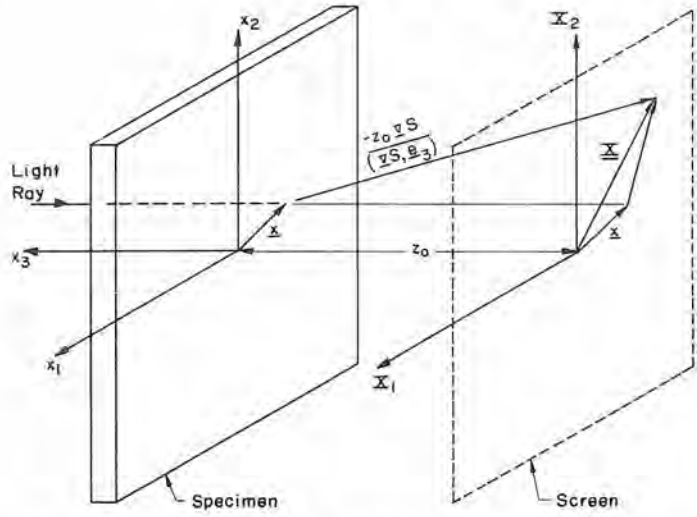

Figure 10.2. Geometrical construction of optical mapping.

translating waves are coincident and S may be approximated by Eq. (2).

With Manogg's [1] assumption and the further assumption of a plate of infinitesimal thickness, the mapping of light rays is found by substituting Eq. (2) into (1) and is given by

$$\mathbf{X} = \mathbf{x} - z_0 \nabla[\Delta s(x_1, x_2)], \tag{3}$$

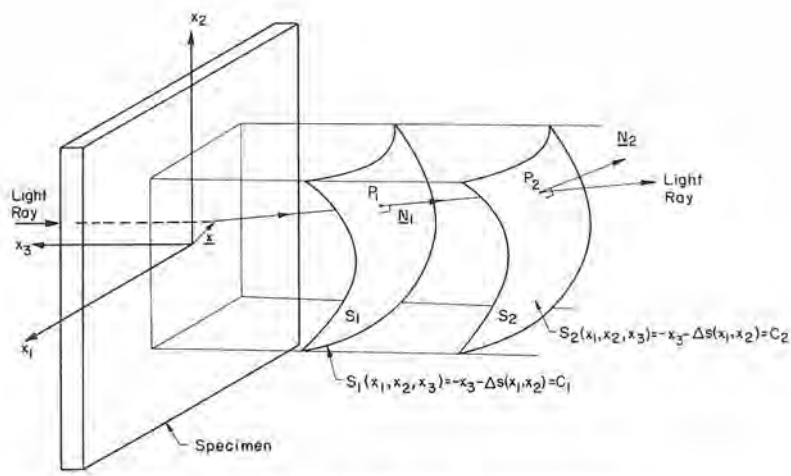

Figure 10.3. Translating wave fronts (Manogg's assumption).

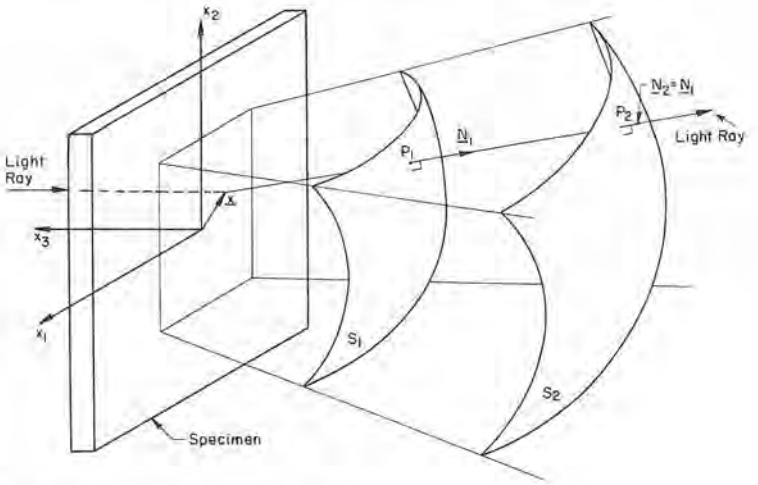

Figure 10.4. Expanding wave fronts.

which is Manogg's original result and is the equation used in the normal evaluation of transmitted caustics for fracture mechanics applications.

The application of caustics to the study of opaque materials requires the reflection of light from the highly polished surface of a planar solid. Theocaris [5] applied Manogg's equation to caustics in reflection by assuming that the change in optical path is given by

$$\Delta s(x_1,x_2) = 2f(x_1,x_2), \tag{4}$$

where $x_3 = -f(x_1,x_2)$ is the equation of the specimen surface. Substituting Eq. (4) into (3) yields

$$\mathbf{X} = \mathbf{x} - 2z_0\nabla f(x_1,x_2). \tag{5}$$

Equation (4) introduces an additional approximation since the actual change in optical path is greater than $2f$, due to the angular deflection undergone. In cases of severe gradients in optical path, the light rays reflected from the plate deviate strongly from parallelism. In such cases Manogg's [1] and Theocaris' [5] assumptions lose validity and a more accurate analysis is required. The exact analysis for reflected caustics is described in detail by Rosakis and Zehnder [33] and is outlined here in the next section.

A.2.1 Caustics by Reflection: The Exact Mapping Equations

In this section, the particular example of caustics obtained by reflection is considered. Caustic images obtained by reflection are associated with changes in the optical path of light rays, introduced due to the nonuniform elevation of a reflector surface. The equations describing the optical map-

ping of points of the reflector on to points of the image plane, also describe transmission caustics, with minor modifications. The basic difference between reflection and transmission is in the nature of the optical path change, which in the latter case is caused by changes in the refractive index of the transparent material in addition to changes in plate thickness.

Consider now a family of light rays, parallel to the x_3 axis, incident on the reflective surface $x_3 = -f(x_1,x_2)$ of an opaque, specularly reflective material, see Fig. 10.5. The reflected light field is recorded by a camera positioned in the front of the reflective specimen surface. The focal plane of this camera, which shall be called the "screen" for convenience, is located *behind* the reflector and intersects the *virtual* extension of the reflected rays at the plane $x_3 = -z_0$, where z_0 is *positive*. The image to be recorded is a *virtual* image, in this case. For a screen located in *front* of the reflector ($x_3 = +z_0$), the image is *real*.

Consider further an incident light ray which intersects the reflecting surface. After reflection from a point $p(x_1,x_2)$ on the polished surface, the ray will deviate from parallelism. The virtual extension of the resulting reflected ray will then intersect the screen at the virtual image point $P(X_1, X_2)$ whose position will depend on the slopes of the reflecting surface at $p(x_1,x_2)$ and on the normal distance z_0. The (X_1,X_2) coordinate system is identical to the (x_1,x_2) system, except that the origin of the former has been translated the distance z_0 to the screen.

If ϕ is the angle between the incident light ray and the normal to the reflector at $p(x_1,x_2)$ and p' is the normal projection of p on to the "screen," then the position vector of the image point P will be given by

$$\mathbf{X} = \mathbf{x} + [(z_0 - f)\tan 2\phi]\mathbf{u}, \tag{6}$$

where

$$\mathbf{X} = X_\alpha e_\alpha, \qquad \mathbf{x} = x_\alpha e_\alpha$$

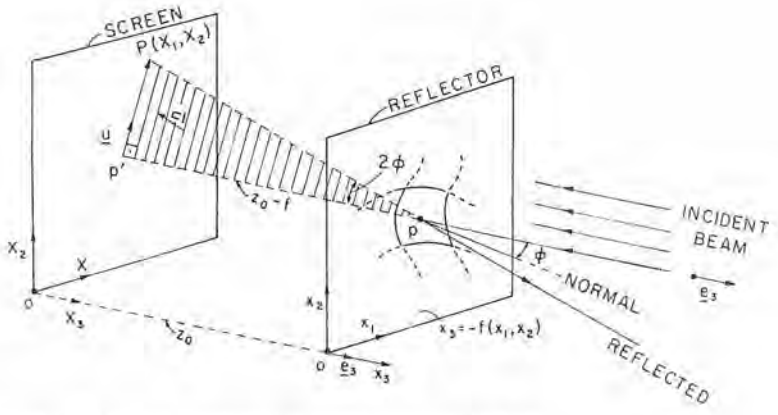

Figure 10.5. Optical mapping for caustics by reflection.

and $\mathbf{u} = \overrightarrow{p'P}/|\overrightarrow{p'P}|$ is the unit vector along $\overrightarrow{p'P}$. Greek indices have the range (1,2).

Also, if $\mathbf{N}$ is the unit normal to the surface $x_3 = -f(x_1,x_2)$ at the point $p(x_1,x_2)$, then $\mathbf{N}$ is equal to $\nabla F/|\nabla F|$ where $F(x_1,x_2) = x_3 + f(x_1,x_2)$. Further, if $\mathbf{e}_3$ denotes a unit vector in the x_3 direction (direction of light incidence), the plane which contains the incident light ray and the corresponding reflected ray will be defined by the normal unit vector $\mathbf{n} = \mathbf{N} \times \mathbf{e}_3/|\mathbf{N} \times \mathbf{e}_3|$. The intersection of this plane with the plane of the "screen" is then the line which has a direction specified by the unit vector $\mathbf{u}$ given by

$$\mathbf{u} = \mathbf{n} \times \mathbf{e}_3 = -\frac{\dfrac{\partial f}{\partial x_1}\mathbf{e}_1 + \dfrac{\partial f}{\partial x_2}\mathbf{e}_2}{\left[\left(\dfrac{\partial f}{\partial x_1}\right)^2 + \left(\dfrac{\partial f}{\partial x_2}\right)^2\right]^{1/2}} = -\frac{\nabla f}{|\nabla f|}. \tag{7}$$

Also, the tangent ϕ between the incident ray and the normal to the reflector can be expressed as

$$\tan\varphi = \frac{\sin\varphi}{\cos\varphi} = \frac{|\mathbf{e}_3 \times \mathbf{N}|}{|\mathbf{e}_3 \cdot \mathbf{N}|} = \left[\left(\frac{\partial f}{\partial x_1}\right)^2 + \left(\frac{\partial f}{\partial x_2}\right)^2\right]^{1/2} = |\nabla f|, \tag{8}$$

By substituting Eqs. (7) and (8) into (6), the position vector of the image point P on the "screen" can be written as

$$\mathbf{X} = \mathbf{x} - 2(z_0 - f)\frac{\nabla f}{1 - |\nabla f|^2}, \qquad z_0 > 0. \tag{9}$$

The above expression describes the optical mapping of points $p(x_1,x_2)$ on the reflector on to point $P(X_1,X_2)$ on the "screen."

Equation (9) can be simplified by introducing assumptions based on the nature of the changes in optical path associated with the specimen studied and depending on the magnitude of z_0. For z_0 sufficiently large, for example, $(z_0 - f)$ is often approximated by z_0. Also, it is often assumed that $|\nabla f|^2 << 1$. In solid mechanics applications, the second assumption has to be justified on the basis of some a priori knowledge of the nature of the deformation fields on a specimen surface. A discussion of the adequacy of the above assumption in fracture mechanics applications is given by Rosakis and Zehnder [33].

The above assumptions reduce the equation of the mapping to the following form

$$\mathbf{X} = \mathbf{x} - 2z_0\nabla f,$$

which is the approximate expression given by Theocaris [5]. For a "screen" situated at $x_3 = +z_0$, the situation is entirely equivalent but the image is now

a real one. Use of a real image results in a change in sign in front of the second term of the right-hand side of Eq. (9). The use of a virtual image in a reflection arrangement, has certain advantages in experimental fracture mechanics as discussed by Beinert and Kalthoff [17].

Given the above approximations and in view of Eqs. (3) and (5) a general expression for the approximate caustics mapping (virtual or real) for both reflection and transmission can be obtained as follows:

$$\mathbf{X} = \mathbf{x} \pm z_0 \nabla[\Delta s(x_1,x_2)], \qquad z_0 > 0, \tag{10}$$

where $\Delta s(x_1,x_2)$ is the optical path difference accumulated at a point $p(x_1,x_2)$ due to the reflection or refraction of a light ray. For the case of reflection of light from the surface of a deformable plate (uniform thickness in the undeformed state)

$$\Delta s(x_1,x_2) = 2f(x_1,x_2) = 2u_3(x_1,x_2),$$

where $u_3(x_1,x_2)$ is the out-of-plane displacement field introduced due to application of loads on the plate. A very illustrative discussion of the relative merits of virtual versus real image usage [choice of sign in Eq. (10)] is given by Beinert and Kalthoff [17].

A.2.2 The Initial Curve and its Significance

Changes in optical path caused by reflection or refraction of parallel light will deflect the light from its original course. Depending on the nature of the optical retardation, the reflected or refracted rays will form an envelope in the form of a three dimensional surface in space. The surface, which is called the *caustic surface*, is the locus of points of maximum luminosity in the reflected or transmitted light fields. The deflected rays are tangent to the caustic surface. When a real or virtual screen is positioned parallel to the $x_3 = 0$ plane and so that it intersects the caustic surface, then the cross-section of the surface can be observed on the screen as a bright curve (the *caustic curve*) bordering a dark region (the shadow spot) on the screen. Two schematic illustrations of the formation of caustics by reflection and transmission from the vicinity of a through crack in an opaque and a transparent plate of uniform thickness is shown in Fig. 10.6. The figure shows the cross section of the plates and light field. The "screen" in Fig. 10.6 (a) is virtual and in a real experimental set up will correspond to the focal plane of a camera placed on the left hand side of the specimen. The "screen" in Fig. 10.6(b) is real.

In the present section, the conditions necessary for the formation of caustic curves are established. The analysis is carried out in reference to a reflection arrangement but the general results hold for both reflection and transmission as long as the appropriate mapping equations are used.

Consider light of intensity $\xi(x_1,x_2)$ incident on the specularely reflective surface of an opaque solid. After reflection, the rays will deviate from par-

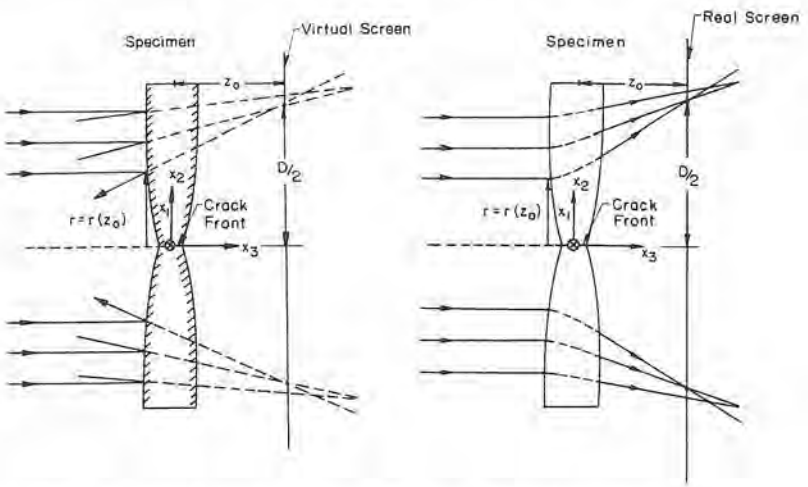

Figure 10.6. Caustic formation in (a) reflection, (b) transmission.

allelism and the reflection process will be described by the mapping equations derived in the previous section [eqs. (9) or (10)]. For perfect reflectivity, the light energy incident on an area D of the highly polished specimen is an invariant of the transformation. Let D' be the image area on the image plane, "screen," corresponding to reflections from area D. Conservation of light energy requires that the total energy E incident onto the area D must equal the total energy E' reaching the area D' of the transformed plane. Thus

$$E = \iint_D \xi(\mathbf{x}) dx_1 dx_2 \tag{11}$$

$$= E' = \iint_{D'} \Xi(\mathbf{X}) dX_1 dX_2,$$

where $\Xi(\mathbf{X})$ represents the light intensity field on the "screen."

Using the equations of the mapping equation (9) and changing variables in the right-hand side of Eq. (11), we obtain

$$E = \iint_D \xi(\mathbf{x}) dx_1 dx_2 \tag{12}$$

$$= E' = \iint_{D'} \Xi[\mathbf{X}(\mathbf{x})] |J(\mathbf{x})| dx_1 dx_2,$$

where $J(\mathbf{x}) = \det(\nabla \mathbf{X})$ is the Jacobian determinant of the transformation Eq. (9). Since expression (12) is true for an arbitrary area D, the integrands involved can be equated, giving

$$\Xi[\mathbf{X}(\mathbf{x}, f)] = \xi(\mathbf{x})/J(\mathbf{x}) = \xi(\mathbf{x})(\det \nabla \mathbf{X})^{-1}. \tag{13}$$

With the equations of the mapping, the Jacobian determinant can be written as

$$J(x) = \det(\nabla \mathbf{X}) = \det\left[\mathbf{1} \pm 2\nabla\left((z_0 - f)\frac{\nabla f}{1 - |\nabla f|^2}\right)\right], \tag{14}$$

where $\mathbf{1}$ is the identity tensor.

Once the equation of the reflecting surface $x_3 = -f(x_1,x_2)$ is given, the value of the Jacobian is completely determined and Eq. (13) can be used to provide the intensity of light at any point on the "screen." The entire image on the screen can thus be predicted. Since the intensity of light reaching the "screen" is inversely proportional to the Jacobian, the vanishing of J in Eq. (13) corresponds to infinite intensity of light on the "screen" plane and the existence of highly luminous curves (caustics) is thus predicted.

The caustic curves therefore correspond to reflections from points on the specularely reflective surface for which the Jacobian determinant vanishes. The loci of points on the reflector on which $J = 0$ are called the *initial curves* and are characterized by the property that rays reflected from their immediate neighborhood are responsible for the generation of the caustic curves. The resulting caustics obtained on the screen are regions of multiple reflection, that is for those points on the caustic curve the mapping Eq. (9) is not invertible and the determinant of the Jacobian matrix is expected to vanish.

Note that J in Eq. (14) depends parametrically on z_0 and thus the initial curve depends on z_0. In the discussion of the numerical work presented by Rosakis and Zehnder [33], z_0 is varied thus varying the initial curve from a curve far from the crack-tip to one very near the crack-tip. This is done to investigate the assumption $|\nabla f|^2 \ll 1$ in fracture mechanics applications.

As indicated earlier the method has potential for use in the study of abrupt changes in optical path introduced by singularities in stress, density, etc. It is of interest, therefore, to carry the investigation one step further and consider some general features of the reflection process in the vicinity of a singularity on the reflecting surface or more generally a singularity in the additional optical path introduced in a medium either by refraction or reflection.

At points far away from such a singularity (as an example, consider a crack-tip) the reflector can be considered almost flat and $\nabla f \to 0$. The second term in Eq. (14) is very small, so $J \to \det\{\mathbf{1}\} = 1$, and $\Xi \to \xi$. Thus, if the intensity of the incident light is uniform, $\xi(\mathbf{x}) = \xi_0$, then uniform intensity of light is predicted on the screen.

As singularity (e.g., crack-tip) is approached, the value of J decreases and the light intensity on the "screen" increases. At some point, J vanishes. The place where that happens is referred to as the *initial curve*.

At the points just inside the initial curve, the determinant in Eq. (14) takes small negative values. As we move closer to the center of the singularity, J decreases further and as $|\nabla f|^2 \to 1$ it tends to $-\infty$. The condition $|\nabla f|^2 = 1$

describes a locus of points referred to by Rosakis and Zehnder [33] as the *interruption curve*.

It is worth noting at this point that at the initial curve there is a reversal of the sign of the Jacobian. This reversal implies "folding" of the mapping. The rays reflected from points on the initial curve map outside the caustic curve. The rays reflected from points inside the initial curve again map outside the caustic. No ray will reach the screen at points inside the caustic and a dark region, the shadow spot, will be created.

In order to investigate the mechanism of reflection more completely, let us consider a two-dimensional reflector $z = -f(x)$ as shown in Fig. 10.7. The function $f(x)$ has a singularity at $x = 0$. Assume that the reflector has a unit depth and that the incident light has a constant intensity represented here by the constant spacing x of the incoming rays.

For this specific case,

$$J = \frac{dX}{dx},$$

where dX is the spacing of the virtual extensions of the reflected rays reaching the "screen." As shown in Fig. 10.7(a), at points away from the singularity $dX \to dx$ and $J \to 1$. As the initial curve is approached, dX decreases and eventually is reduced to zero. Decreased spacing of rays represents high light intensity and a caustic curve is obtained by reflections coming from the vicinity of the initial curve. So far, for points outside the initial curve the mapping is one to one and all points are mapped outside the caustic curve. Right on the initial curve, all points are mapped directly on to the caustic. As we move inside the initial curve, the Jacobian changes sign, and a "folding" of the mapping is observed. This means that, as shown in Fig. 10.7(b), points inside the initial curve map again outside the caustic. At points just

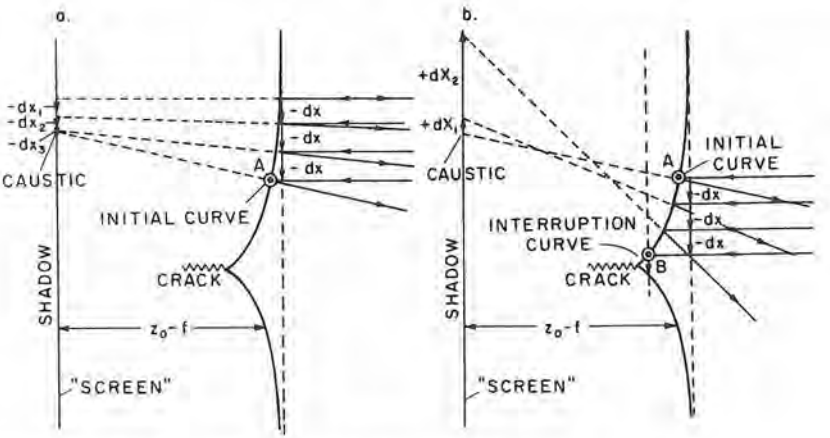

Figure 10.7. Folding of the optical mapping in 2D.

inside the initial curve, the value of J is small and negative (small spacing of rays on "screen"). As we move further in, J becomes larger in magnitude (increased spacing dX) until it reaches the value of $-\infty$ at the interruption curve (point where the slope of the reflector is $\pm 45°$). The main features of the mapping can therefore be summarized as follows:

1. Points on the reflecting surface lying outside the initial curve will map onto points of the "screen" lying outside the caustic.
2. Points on the initial curve will map directly on the caustic.
3. Points lying in the region between the initial and the interruption curve will map again outside the caustic.
4. Points inside or on the interruption curve will not be mapped on the screen.

In other words, there are no points on the reflector that will map inside the caustic curve, and thus a dark region (shadow spot) surrounded by a highly luminous curve (caustic) is formed on the "screen."

Letting $\partial\omega$ denote the initial curve defined in the reflector plane (x_1,x_2) and $\partial\Omega$ denote the caustic curve defined in the screen plane (X_1,X_2) we can write

$$\mathbf{x} \in \omega^+ \cup \partial\omega \cup \omega^- \rightarrow \mathbf{X}(\mathbf{x}) \in \Omega^+ \cup \partial\Omega,$$

$$\mathbf{x} \in \partial\omega \rightarrow \mathbf{X}(\mathbf{x}) \in \partial\Omega,$$

which implies

$$\mathbf{X}^{-1}(\Omega^-) = \emptyset,$$

where ω^+ represents the region outside the initial curve, ω^- represents the annular region between the initial and the interruption curves, and Ω^+,Ω^- are the regions from outside and inside the caustic, respectively.

From the above it is clear that the total intensity at a point $P(X_1,X_2)$ on the "screen" is given by

$$\Xi = \xi\left(\frac{1}{|J|_{x\in\omega^+}} + \frac{1}{|J|_{x\in\omega^-}}\right). \tag{15}$$

The two terms represent the contribution to the intensity at $P(X_1,X_2)$ from rays reflected from regions both outside and inside the initial curve. For example, the intensity at a point far away from the optical singularity on the screen will come from rays reflected at points very far from the deformation singularity where $J_{x\in\omega^+} \rightarrow -1$ and from points very close to the interruption curve where $J_{x\in\omega^-} \rightarrow -\infty$. Thus from Eq. (15) $\Xi(\mathbf{X}) \rightarrow \xi(\mathbf{x})$ (no optical distortion).

At points closer to the optical singularity both terms increase and they both become infinite on the caustic where contributions coming by reflection form both just inside and just outside the initial curve are added.

The discussion provided above can be carried out in an entirely analogous way for the transmission cases. If in addition the small deflection angle assumptions discussed in previous sections are introduced the mapping equations for both reflection and transmission will be given by Eq. (10). These may be used to obtain the equation of the initial curve as follows

$$J(x_1,x_2;z_0) = \det(\nabla \mathbf{X}) = \det[\mathbf{1} \pm z_0 \nabla(\Delta s)] = 0, \tag{16}$$

where $\Delta s(x_1,x_2)$ is the optical path difference ($\Delta s = 2f = 2u_3$ for reflection), and ∇ is the two-dimensional gradient operator. Relation (16) is the necessary and sufficient condition for the existence of a caustic curve.

For fracture mechanics applications which are of relevance in this chapter, the plate specimen contains a stationary or running through-crack and the origin of the coordinate system is often taken to be on the crack front at the specimen center. In such cases the initial curve is found to be a curve completely surrounding the crack-tip, whose exact geometry and size will depend, among other things, on material constitution and on the distance of the specimen to the screen (z_0). Indeed, the initial curve has some interesting properties which are briefly described below.

Since light reflected both from the inside and the outside of the initial curve maps outside the caustic, the area within the caustic remains dark and surrounds a shadow spot on the image plane (screen) which is "roughly" centered at the crack tip obscuring its exact location. An example of a series of caustics and shadow spots obtained by reflection of light from the vicinity of an initiating and dynamically propagating crack in AISI 4340 steel is shown in Fig. 10.8. The specimen is of the three point bend type and is impact loaded in a drop weight tower. The crack-tip speed in this case varies in the range of 1,000–1,500 m/s. The circular rings surrounding the caustic and shadow spot are caustic images of stress waves generated during crack growth. These rings become visible only after the instant of crack initiation.

Since the light that forms the caustic originates from the initial curve, essential information conveyed by the caustic comes from that curve only. Equation (16) defining the initial curve depends parametrically on z_0. Thus, by varying z_0, we may vary the initial curve position. If z_0 is large, the initial curve will be far from the crack-tip. If z_0 is small, the initial curve will be close to the crack-tip. In a practical experimental setup, a camera is often used to record the transmitted or reflected light fields. In this case the object plane of this camera is the "screen" and its distance from the specimen is z_0. In a reflection arrangement, for example, the object plane of the camera is often set behind the specimen surface and thus the image is virtual. Variation of z_0 can thus easily be achieved experimentally by simply varying the object plane of the recording camera system. For $z_0 = 0$ the camera is focused on the specimen plane and no caustic image is obtained [see Eqs. (10) and (14)].

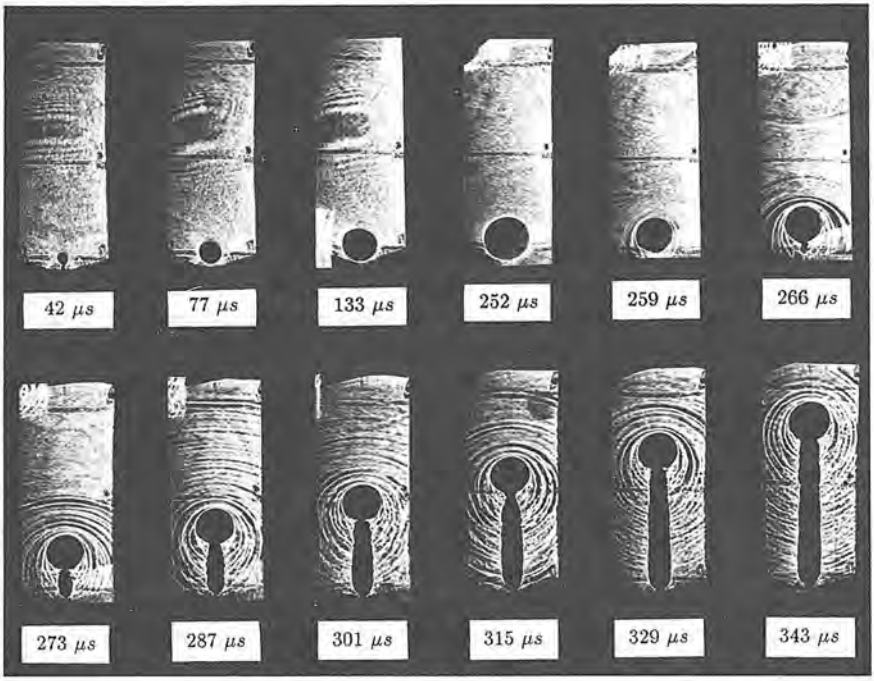

Figure 10.8. Caustics from a dynamically initiating and rapidly propagating crack in a AISI 4340 steel plate.

The dependence of initial curve size on z_0 is an essential property of the method of caustics, and it can be utilized to scan the near-tip region to obtain information regarding the nature of the deformation field at different distances from the crack-tip. This property will be utilized extensively in the following sections.

It should be emphasized at this point that the analysis of caustics presented above is based on concepts of geometrical optics. A very interesting alternative analysis based on wave optics has recently been discussed by Kamath and Kim [40].

A.3 Relation Between Optical Path Difference and Deformation State

In fracture mechanics applications of the optical method of caustics, the relation between the optical path difference and the deformation state is essential in interpreting the experimentally obtained caustic images. The establishment of such a relation allows for the direct measurement of fracture parameters such as the static or dynamic stress intensity factors or the J

integral. This section highlights the assumptions introduced in order to perform such measurements in experimental situations involving plate specimens containing through thickness cracks.

A.3.1 Caustics by Reflection

For opaque plate specimens of uniform thickness, in the undeformed state, caustics are formed by the reflection of light rays from the polished specimen surface. The shape of the caustic curve depends on the near-tip normal displacement u_3 of the plate surface ($f = u_3$), initially at $x_3 = h/2$, where h is the undeformed plate specimen thickness. The change in optical path in this case is given by

$$\begin{aligned} \Delta s(x_1,x_2) &= 2u_3(x_1,x_2,h/2) \\ &= 2h \int_0^{1/2} \varepsilon_{33}(x_1,x_2,x_3)d(x_3/h), \end{aligned} \tag{17}$$

where $\varepsilon_{33} = \partial u_3/\partial x_3$ is the direct strain component in the thickness direction. This relation is independent of constitutive law but assumes infinitesimal deformations.

For an isotropic, homogeneous, linear elastic solid, the above reduces to

$$\begin{aligned} \Delta s(x_1,x_2) &= 2u_3(x_1,x_2,h/2) \\ &= \frac{-2\nu h}{E}\int_0^{1/2}\left[(\sigma_{11} + \sigma_{22})\left(1 - \frac{\sigma_{33}}{\nu(\sigma_{11} + \sigma_{22})}\right)\right]d(x_3/h). \end{aligned} \tag{18}$$

A.3.2 Caustics by Transmission

For transparent plate specimens of uniform thickness in the undeformed state, the optical path change Δs depends on both local changes in thickness and on local changes in refractive index, and can be expressed (Rosakis and Ravi-Chandar [34]) as

$$\begin{aligned} \Delta s(x_1,x_2) &= 2h(n - 1)\int_0^{1/2} \varepsilon_{33}d(x_3/h) \\ &\quad + 2h\int_0^{1/2} \Delta n\, d(x_3/h), \end{aligned} \tag{19}$$

where n is the refractive index of the material in the undeformed state. Up to this point no constitutive information has been utilized. The first term represents the net optical path difference due to changes in plate thickness caused by the strain component ε_{33}. The second term is due to the stress induced change in refractive index of the material. This change in the re-

fractive index Δn is given by the Maxwell relation (see Theocaris [7], Kalthoff [18]),

$$\Delta n(x_1,x_2) = D_1(\sigma_{11} + \sigma_{22} + \sigma_{33}),$$

where D_1 is the stress optic constant and σ_{ij} are Cartesian components of the Cauchy stress tensor. The above relation is strictly true for isotropic linear elastic solids. For such solids the strain component ε_{33} can also be related to the stresses in a straightforward manner and the change in path length becomes

$$\Delta s(x_1,x_2) = 2h\left(D_1 - \frac{\nu}{E}(n-1)\right) \times \int_0^{1/2} \left\{(\sigma_{11} + \sigma_{22})\left[1 - D_2\left(\frac{\sigma_{33}}{\nu(\sigma_{11} + \sigma_{22})}\right)\right]\right\} d(x_3/h), \tag{20}$$

where

$$D_2 = -\left(\frac{\nu D_1 + \nu(n-1/E}{D_1\nu(n-1)/E}\right),$$

E and ν are the Young's modulus and the Poisson's ratio of the material, respectively.

A.3.3 Interpretation of Caustics on the Basis of Plane Stress Analysis

The discussion of the previous section was intentionally kept as general as possible within the assumptions of isotropic linear elasticity. For a cracked linear elastic plate of uniform thickness and finite in-plane dimensions, the optical path difference Δs given by Eqs. (3) and (4) in general will depend on the details of the three-dimensional elastostatic or elastodynamic stress state that would exist at the vicinity of the crack-tip. This will be a function of the applied loading, as well as of the in-plane dimensions and thickness of the specimen. Given the lack of full-field, three-dimensional analytical solutions in fracture mechanics, such information can be obtained only by means of detailed numerical calculations. Such an approach was adopted by Rosakis, Zehnder, and Narasimhan [41] and by Narasimhan and Rosakis [42].

Nevertheless, there exist certain nontrivial special cases for which available asymptotic solutions, based on two-dimensional analyses, may provide adequate approximations for $\Delta s(x_1,x_2)$. In particular, it has been argued that conditions of generalized plane stress will dominate in thin cracked plates

at distances from the crack front larger than half the specimen thickness. This would imply that if the initial curve is kept outside the near-tip three-dimensional zone, the resulting caustic could be interpreted on the basis of a generalized plane stress analysis. (See Rosakis and Ravi-Chandar [34] and Narasimhan and Rosakis [42].)

To illustrate the extent of the near-tip three-dimensional, reference is made to Fig. 10.9 which shows a 3D representation of the ratio $[\sigma_{33}/\nu(\sigma_{11} + \sigma_{22})]$, often called the degree of plane strain. This ratio is a measure of near-tip three dimensionality and is obtained by means of a 3D finite element calculation, which models a stationary crack in a three-point-bend specimen subjected to dynamic loading. In regions where the deformation is locally plane stress, this measure is equal to zero. In the figure, only one half of the specimen thickness is shown. The top surface corresponds to the mid-plane of the specimen. The maximum extent of the 3D zone is approximately 0.4–0.5h. (For details, see Krishnaswamy and Rosakis [36], Krishnaswamy, Rosakis, and Ravichandran [37].) For points outside this region, a plane stress approximation will be applicable. Indeed for such points the optical path

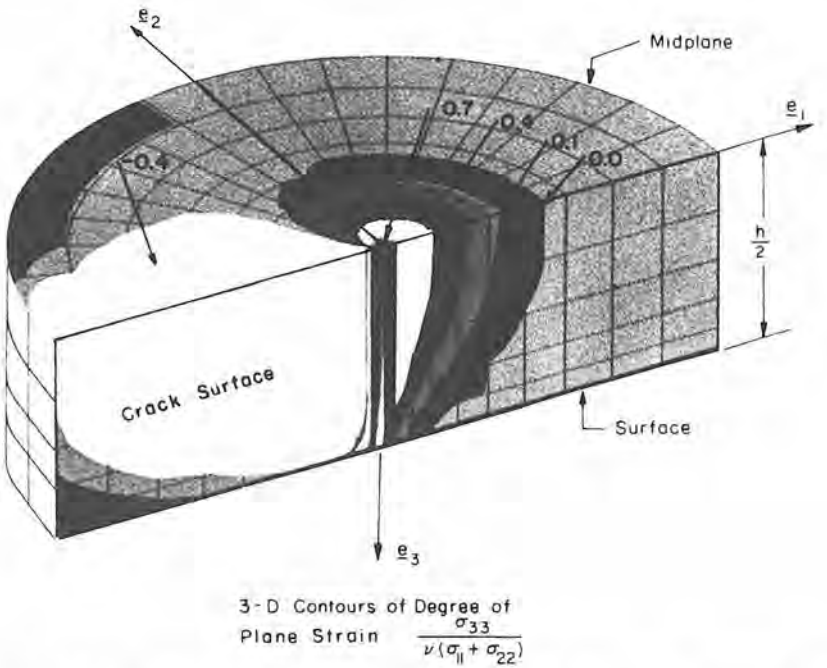

Figure 10.9. Plane strain constraint near a through thickness crack in a plate of uniform thickness h. Only half the plate thickness is shown. The top surface is the midplane of the specimen.

difference Δs [Eqs. (18) and (20)], which involve the ratio $\sigma_{33}/\nu(\sigma_{11} + \sigma_{22})$, will simplify to

$$\Delta s(x_1,x_2) \approx ch[\hat{\sigma}_{11}(x_1,x_2) + \hat{\sigma}_{22}(x_1,x_2)], \tag{21}$$

where

$$c = \begin{cases} \left[D_1 - \dfrac{\nu}{E}(n-1)\right] = c_\sigma, & \text{for transmission} \\ -\dfrac{\nu}{E}, & \text{for reflection.} \end{cases}$$

and $\hat{\sigma}_{11}$ and $\hat{\sigma}_{22}$ are thickness averages of the stress components in the solid. In the above expression c_σ is called the stress-optical coefficient. These stress components will be provided by the generalized plane stress solution of the elastostatic or elastodynamic problem under investigation. Values of c_σ for different transparent solids are provided by Beinert and Kalthoff [17].

A.4 Caustic Analysis Based on Plane Stress Asymptotic Crack-Tip Fields in Linear Elastostatics and Elastodynamics

A.4.1 Analysis Based on K_I^d Dominance, Assumptions, and Shortcomings

In this section we present the methodology that leads to the classical analysis of optical caustic patterns generated during quasistatic or dynamic crack growth in elastic solids. Stationary cracks are treated as a special case. We pay particular attention to the assumptions involved and we attempt to analyze some cases where these assumptions break down.

Consider a Mode-I crack propagating dynamically in a thin plate composed of a homogeneous isotropic, linear elastic material. The crack-tip velocity and the dynamic stress intensity factor are both allowed to be arbitrary functions of time. If a generalized *plane stress* assumption is made, then the thickness average of the first stress invariant $\hat{\sigma}_{11} + \hat{\sigma}_{22}$ at the vicinity of the propagating crack-tip can be asymptotically expressed (Freund and Clifton [43], and Freund [44]) as

$$\hat{\sigma}_{11} + \hat{\sigma}_{22} = F(v)\frac{K_I^d(t)}{\sqrt{2\pi r_I}}\cos(\theta_I/2) + O(1) \qquad \text{as} \quad r_I \to 0, \tag{22}$$

where

$$F(v) = \frac{2(1 + \alpha_s^2(\alpha_I^2 - \alpha_s^2)}{[4\alpha_I\alpha_s - (1 + \alpha_s^2)^2]},$$

$$\alpha_{l,s} = \left(1 - \frac{v(t)^2}{c_{l,s}^2}\right)^{1/2},$$

$v(t)$ is the instantaneous crack speed, $c_{l,s}$ are the longitudinal and shear wave speeds, respectively. $K_I^d(t)$ is the instantaneous value of the dynamic stress intensity factor,

$$r_l = [x_l^2 + (\alpha_l x_2)^2]^{1/2}, \qquad \theta_l = \tan^{-1}[(\alpha_l x_2)/x_1],$$

and the distorted polar coordinate system (r_l, θ_l) translates with the moving crack-tip. Stationary cracks in linear elastic solids are a special case for $v = 0$.

For laboratory specimens of finite dimensions, the above field can be valid only within a region near the crack-tip of extent small compared to any relevant characteristic dimension of the body. On the other hand, the assumption of a two-dimensional field cannot be valid right up to the crack-tip. As shown in the previous section, within some region near the tip (closer than half the specimen thickness) the two-dimensional field must give way to a region of severe three dimensionality where the plane stress assumption breaks down. Although the above restrictions are *competing*, there may be cases where there exists some finite annular region surrounding the crack-tip such that the stress field is square-root singular and $(\hat{\sigma}_{11} + \hat{\sigma}_{22})$ is described by Eq. (22). In such cases we say that we have a situation of K_I^d *dominance* and we assume that the stress intensity factor characterizes the fracture process. The classical analysis of caustics, for both statics and dynamics, assumes that K_I^d dominance always exists and attempts to relate the dimensions of the caustic curve to the instantaneous value of K_I^d.

From a mathematical standpoint the above expression [Eq. (22)] is only the leading term of a transient asymptotic expansion for the stresses, which will be presented in the following section. As will be seen in that section, only the leading $1/\sqrt{r_l}$ term of the transient expansion has the same form as the corresponding term of an expansion obtained if *steady-state* conditions are assumed. Indeed the $O(1/\sqrt{r_l})$ term of the transient problem is obtained if the constant values for K_I^d and v of the steady-state case are replaced by their time varying counterparts. However, this is not true for terms of higher order. For the transient crack growth problem, such terms will in general contain time derivatives of $v(t)$ and $K_I^d(t)$. As a result their importance relative to the leading term will depend on the nature of the time history of crack-tip speed and stress intensity factor as well as on the distances from the crack tip where measurements are performed. In addition, the θ_l variations of the transient higher-order terms are found to be different from their steady-state counterparts of the same order in r_l [see Eq. (28)].

The classical analysis of caustics is based on the assumption of K_I^d dominance. This means that in a real experimental situation, Eq. (22) approximates the stress field at least in a nonvanishing annulus defined by $b<r<a$. The inner bound b is dictated by the extent of the three-dimensional zone

surrounding the crack-tip (see previous section) while a is determined by the transient nature of the loading (see next section). A region where Eq. (22) holds is called a *K_I^d-dominant region*.

If the optical path difference corresponding to Eqs. (21) and (22) is substituted into the caustic mapping Eq. (10) for a virtual image (negative sign), these become

$$X_1 = r_l \cos\theta_l + \hat{K} r_l^{-3/2} \cos\frac{3\theta_l}{2}, \tag{23}$$

$$X_2 = \frac{r_l \sin\theta_l}{\alpha_l} + \alpha_l \hat{K} r_l^{-3/2} \sin\frac{3\theta_l}{2},$$

where

$$\hat{K} = \frac{z_0 hcF(v)K_I^d}{\sqrt{2\pi}}.$$

As discussed above, the condition for the existence of a caustic curve is the vanishing of the Jacobian determinant of the mapping described by Eq. (23). The final form of this condition is obtained by substituting Eq. (22) into relation (21) and using Eq. (16) to provide the locus of points surrounding the crack-tip (initial curve) where the Jacobian vanishes. The equation of the initial curve is thus given by

$$r_l^5 - \frac{9}{4}\hat{K}^2\alpha_l^2 + \frac{3}{2}\hat{K} r_l^{5/2}(\alpha_l^2 - 1)\cos\frac{5\theta_l}{2} = 0. \tag{24}$$

The equation of the caustic curve is now given by the mapping equations (23) under the constraint provided by Eq. (24). (For details see Rosakis [28].) As has been demonstrated by Kalthoff, Beinert, and Winkler, for realistic crack-tip velocities ($v < 0.4c_s$, where c_s is the material shear wave speed), the third term of this equation is small compared to the first two. This implies that the initial curve is nearly a circle of radius $r_0(t)$. Its equation is given by

$$r_l = (\frac{3}{2}\alpha_l\hat{K})^{2/5} = \left(\frac{3hcK_I^d(t)z_0}{2\sqrt{2}F[v(t)]}\right)^{2/5} = r_0(t). \tag{25}$$

Note that for a fixed z_0 value, r_0 is, in general, a function of time dictated by the stress intensity factor and velocity histories. Substituting $r_l = r_0$ in the mapping equations (23) one obtains the parametric equations for the caustic curve:

$$X_1 = r_0\left(\cos\theta_l + 2/3\alpha_l^{-1}\cos\frac{3\theta_l}{2}\right), \tag{26}$$

$$X_2 = \frac{r_0}{\alpha_l}\left(\sin\theta_l + 2/3\alpha_l \sin\frac{3\theta_l}{2}\right).$$

The above relations are the parametric equations of the caustics for dynamic crack growth and are obtained under the assumption of K_I^d dominance [existence of a region surrounding the tip where relation (22) describes the stress field accurately]. For a quasistatically propagating ($v/c_l \to 0$) or a stationary ($v = 0$), crack, $\alpha_l \to 1$ or $\alpha_l = 1$, and relations (26) become the parametric equations for an epicycloid. (See Theocaris [7].)

The caustic equations (26) can now be used to relate the instantaneous value of the stress intensity factor $K_I^d(t)$ with maximum transverse diameter ($D = 2X_2^{MAX}$) of the caustic. For dynamic crack growth under K_I^d dominance this relation becomes

$$K_I^d(t) = \frac{2\sqrt{2\pi}}{3\alpha_l c h z_0 F(v)} \left(\frac{D(t)}{3.17}\right)^{3/2}. \tag{27}$$

The above relation reduces to the original static result by Manogg [1] if $v \to 0$, recalling that in such a case $F(v) \to 1$ and $a_l \to 1$.

It should be emphasized again at this point that the above results have been derived under the assumption of *plane stress* and K_I^d *dominance*. Keeping this fact in mind is important in estimating the limits of the applicability of these relations in experimental investigations of dynamic crack growth conducted in laboratory size specimens where these assumptions may be violated.

For the case of *quasistatically loaded, stationary cracks* in single-notch specimens of steel and PMMA, Rosakis and Ravi-Chandar [34] have investigated the limits of the K_I-dominant plane stress interpretation of caustic patterns generated at different distances near the crack-tip. The specimen configuration was chosen in such a way that K_I^d dominance was realized outside the near-tip three-dimensional zone. Specimens of identical in-plane dimensions but different thicknesses were tested in both transmission and reflection. For each specimen and load level, the distance z_0 (between the specimen and the focal plane of the camera "screen") was varied and the caustic curves were photographed. Following Eq. (25) (for $v = 0$) it can be seen that an increase or decrease of z_0 implies an increase or decrease of the radius of the initial curve r_0 for the same level of stress intensity factor. The near-tip region was thus scanned in the range $0 < r_0 < 2h$. Since points on the initial curve map directly on to the caustic, the resulting caustics will be described by Eqs. (26) and (27) only if the initial curves generating them lie on regions near the crack-tip where the stress field is well described by Eq. (22). It is only then that caustics can furnish the correct values of stress intensity factor through Eq. (27). Boundary value measurements of the loads, conducted simultaneously with the optical experiments, provided the value of the stress intensity factor which was called K_{2D}. The sequence of caustic curves obtained by varying z_0 were also used to obtain an independent measurement of K called K^{EXP}, by *assuming that* Eq. (27), $v = 0$, was valid for the whole range of initial curve radii achievable in the experiments.

Some of the results of their investigation are shown in Fig. 10.10. The figure shows the ratio K^{EXP}/K_{2D} plotted versus the normalized radius of the initial curves used to generate the caustics.

It becomes apparent from these figures that for caustics generated by initial curves whose radii are larger than half the specimen thickness, caustics analyzed on the basis of Eq. (27) provide the correct value of the stress intensity factor. This in turn implies that for *quasistatically loaded, stationary cracks* and large enough specimens, K_I^d dominance may prevail for $r > 0.5h$. On the other hand, for $r < 0.5h$ the interpretation of caustics through relation (27) clearly fails. This is consistent with the numerical results presented in Fig. 10.9. The figure clearly shows that the maximum extend of the near-tip three-dimensional zone is approximately equal to $0.5h$. To further demonstrate the consistency between the experimental predictions (Fig. 10.10) and the numerical calculations (Fig. 10.9) one may observe that as the crack front is approached ($r/h \to 0$ and $\forall\ -h/2 < x_3 < h/2$) the value of the ratio $\sigma_{33}/\nu(\sigma_{11} + \sigma_{22})$ plotted in Fig. 10.9 tends to unity and thus the optical path difference Δs, for caustics by reflection [Eq. (18)], vanishes. This implies that the *apparent* stress intensity factor K^{EXP} measured by caustics, insisting on a plane stress interpretation even within the 3D zone, will drop to zero as the crack-tip is approached. This is exactly what is predicted by Fig. 10.10(b). For further discussion on this subject regarding dynamically loaded stationary cracks, see Krishnaswamy, Rosakis, and Ravichandran [37]. Also, for a numerical investigation of three-dimensional effects during *steady-state* elastodynamic crack growth, see Smith and Freund [45].

The situation may be even more complicated than the one described above if the plane stress region surrounding the near-tip 3D zone is not K dominant (not well described by only the first term of the asymptotic expansion in the stresses). In quasistatic cases this may be due to specimen geometry (e.g., the proximity of a specimen boundary to the crack-tip). In such a case the plane stress region surrounding the 3D zone would only be adequately described by a more complete higher order description of the stresses and Eqs. (23)–(29) derived above would again be inaccurate.

For *transient* dynamic crack growth on the other hand, a higher-order term expansion may be necessary even in cases where specimen in-plane dimensions are much larger than the crack length. This is true since for transient crack growth the coefficients of a higher-order expansion also depend on the magnitude of the time derivative of stress intensity factor and on the crack-tip acceleration history. (See Freund and Rosakis [46], Rosakis, Liu, and Freund [47], and Krishnaswamy, Tippur, and Rosakis [48].) In such cases a more elaborate analysis of caustics may be necessary for the correct measurement of the time history of stress intensity factor. (For more discussion on the structure of transient high-order terms, see Secs. A.5 and B.1. Also the recent analytical investigations by Ma and Freund [49], and by Ma [50] on the transient nature of near-tip fields is of relevance here.)

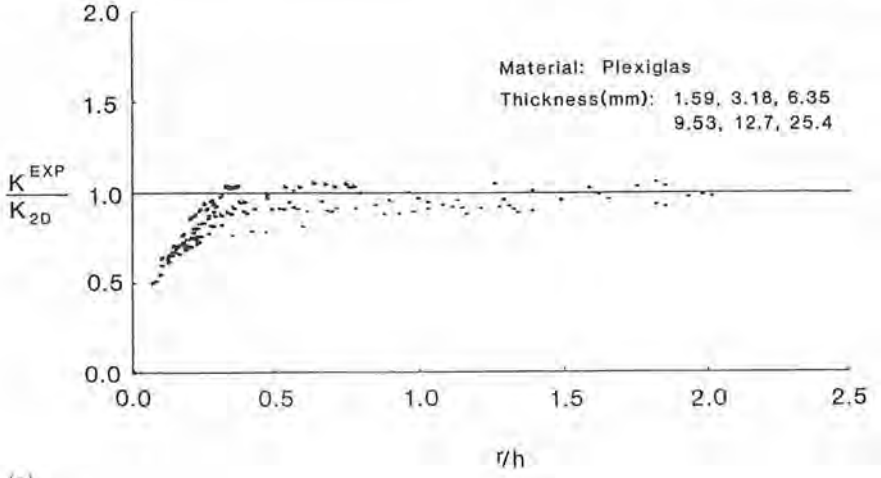

(a)

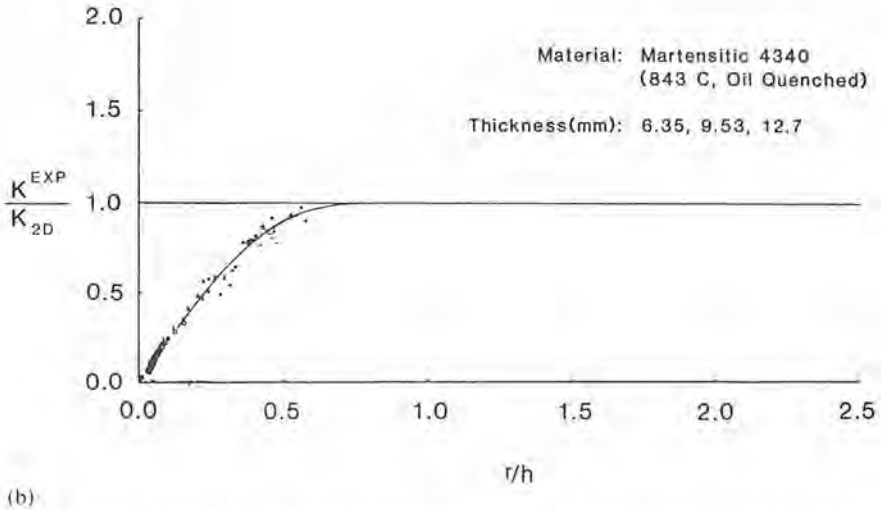

(b)

Figure 10.10. (a) Ratio of apparent stress intensity factor inferred from local caustics measurements (caustics by transmission) to analytical two-dimensional value, versus distance from crack-tip divided by specimen thickness. Material: Plexiglass. (b) Ratio of apparent stress intensity factor inferred from local caustics measurements (caustics by reflection) to analytical two-dimensional value, versus distance from crack-tip divided by specimen thickness. Material: Martensitic 4340 carbone steel.

In a typical dynamic fracture experiment, a high-speed camera is used to obtain a time sequence of caustics. The diameter $D(t)$ of these caustic is measured and hence the stress intensity factor $K_I^d(t)$ is inferred using Eq. (27). Unlike static experiments, the focal distance of the camera (and hence z_0) has to be kept constant during the dynamic event whose net duration is often of the order of milliseconds. From Eq. (25) one finds that $r_0(t) = \tilde{r}_0$ $(K_I^d(t), z_0, \nu(t))$ and as $K_I^d(t)$ varies with time in a dynamic experiment, the radius of the initial curve would perforce change during the course of the experiment. Thus, from the point of view of experiments, it is vital to know that Eq. (21) based on the plane-stress approximation together with the asymptotic equation (22) lead to a valid expression for the optical path difference field for at least the range of radii that the initial curve would cover during the event of interest.

To make matters a little more explicit, suppose that during the event of interest (which could be the crack propagation phase) the initial curve radius is known from previous experience to vary in the region $r_{\min} \leq r_0 \leq r_{\max}$ for some choice of the object plane distance z_0. Also, since the domain of validity of Eq. (22) could, in general, be time dependent as well, let a and b be such as to give the smallest annulus in which Eq. (22) holds, for all times during the entire event of interest. Then, for a valid interpretation of the caustics in terms of the above formulas [Eq. (27)], the inequalities

$$b < r_{\min} \leq r_0 \leq r_{\max} < a,$$

must be satisfied in order to have the initial curve fall in a region of K_I^d dominance *at all times*.

The first attempts to address the issue of the validity of Eq. (22) is reported in Ravi-Chandar and Knauss [26]. A series of tests were performed using the method of caustics in transmission on identical specimens under identical stress-wave loading, varying from test to test only the object plane distance z_0. In this manner a range of initial curve radii was scanned and, since presumably the actual stress-intensity factor history $K_I^d(t)$ for various tests must be identical, the apparent stress intensity factors measured from caustics obtained from different object planes must also agree, at least for those times when the initial curve falls within the region of K_I^d dominance. Their results were also found consistent with the elastodynamic analysis performed by Ma and Freund [49] who modeled the same experimental situation. Their findings indicate that the assumptions behind Eq. (22) might not generally be tenable. Since a substantial part of the dynamic fracture data extent in the literature has been obtained through the use of either caustics or photoelasticity, the ramifications of the result are potentially far-reaching and thus deserve more careful scrutiny.

In particular, in the method of caustics, it would be preferable to be able to obtain the apparent stress-intensity factor values from different initial curves around the crack-tip for the same specimen at any instant in time.

While comparison of results across tests can be made with confidence for the loading regime of the experiments, this becomes more difficult in the crack propagation phase since small variations in crack motion history could lead to large variations in the value of the stress intensity factor from test to test.

A.4.2 Bifocal Caustics Experiments

A schematic of the optical set-up required to bring two different object planes simultaneously into focus in a single camera is shown in Fig. 10.11. This schematic corresponds to a reflection arrangement for caustics. The setup entails the use of two beam splitters and two mirrors by which two optical paths of different path lengths are established between the opaque specimen and the high-speed camera. With reference to the figure, let the high-speed camera be set up to focus at a distance f from the camera lense. Along path (1) this would mean that the virtual object plane is located at a distance z_{01} behind the specimen. Along path (2), however, by virtue of the increased length ($2L$) between the specimen and the camera lens, the object plane would now fall only a distance $z_{02} = z_{01} - 2L$ behind the specimen. Thus the caustic obtained from the two paths would be from two different initial-curve radii. These two caustics could be made to appear on the film track of the high-speed camera either superposed or side by side.

In a similar manner, a bifocal optical arrangement for caustics by transmission can be designed. Such an arrangement is shown in Fig. 10.12. Here the laser light is transmitted through the transparent specimen and the two object planes are real and are located at two different distances, z_{01} and z_{02}, in front of the specimen.

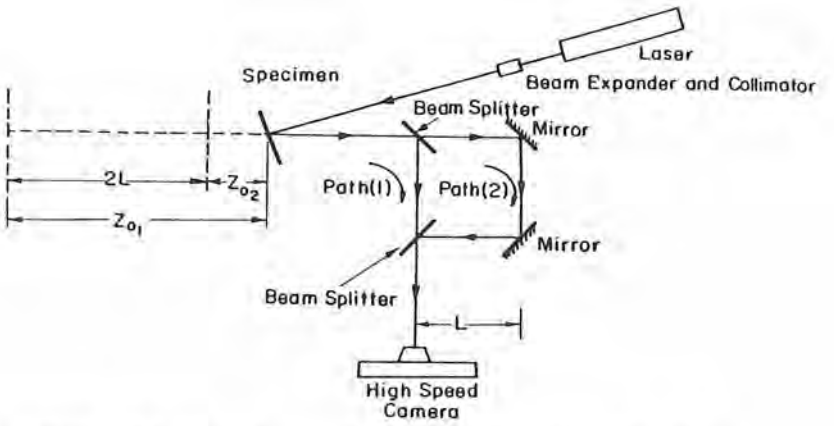

Figure 10.11. Schematic diagram of a reflection bifocal caustics setup.

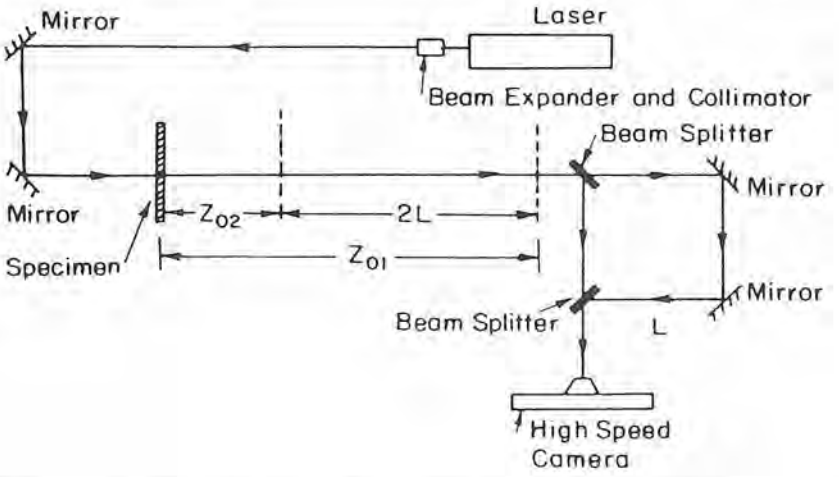

Figure 10.12. Schematic diagram of transmission bifocal caustic setup.

For nomenclatural convenience, the pairs of dynamic caustics obtained by use of this bifocal high-speed camera will henceforth be referred to as "bifocal caustics," with the implicit understanding that such caustics are obtained from two different initial curves on the same specimen at the same time. By changing the distance L from test to test or by changing the focal plane of the camera, one could of course scan various sets of initial curves. Figure 10.13 is a photograph of the actual experimental setup in reflection. The sets of beam splitters and lenses are clearly visible. The drop weight tower used to load the specimen is also shown in the background.

A.4.3 Results of the Bifocal Caustics Experiments

The test which are described below were done in a reflection arrangement and were performed on three-point-bend AISI 4340 steel specimens 30.5 cm long, 15.25 cm wide, and 1.0 cm thick with an initial notch of length 3.8 cm. The specimens were heat treated as follows: (1) normalized at 1,650 °C for 1 h and air cooled, (2) austenitized at 1,550 °C for 1 h and oil quenched, and (3) tempered at 220 °C for 1 h and air cooled. One surface of each specimen was lapped and polished. A Dynatup 8100A drop-weight tower was used as the loading device. A rotating mirror high-speed camera in conjunction with an argon-ion pulse laser was used to record a time-sequence of bifocal caustics as described earlier. The details of specimen preparation and the experimental setup may be found in Krishnaswamy and Rosakis [36]. The pairs of caustics obtained at each instant of time were analyzed as described earlier to get the apparent stress intensity factor histories. Only representative results will be presented here (see Fig. 10.14). Figure 10.15 shows the results

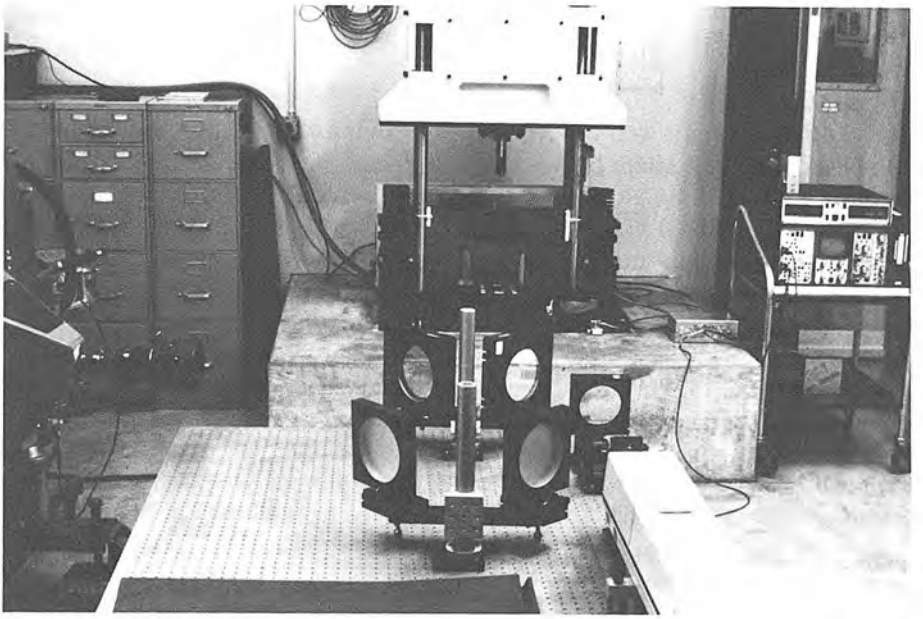

Figure 10.13. Photograph of experimental setup and loading device for "bifocal caustics." (Reflection.)

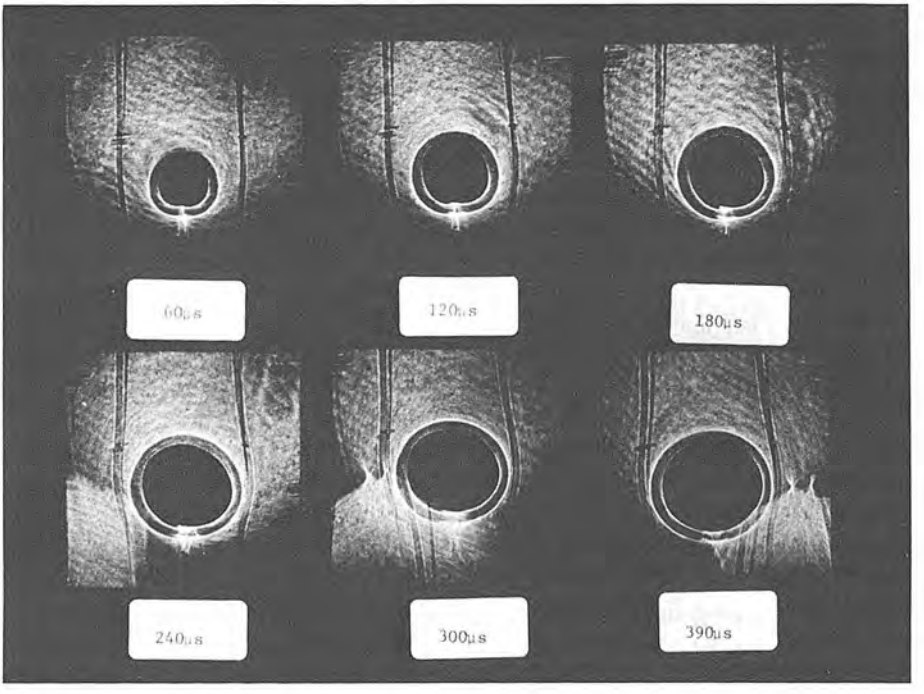

Figure 10.14. Representative sequence of reflection bifocal caustics of a dynamically loaded stationary crack in AISI 4340 steel.

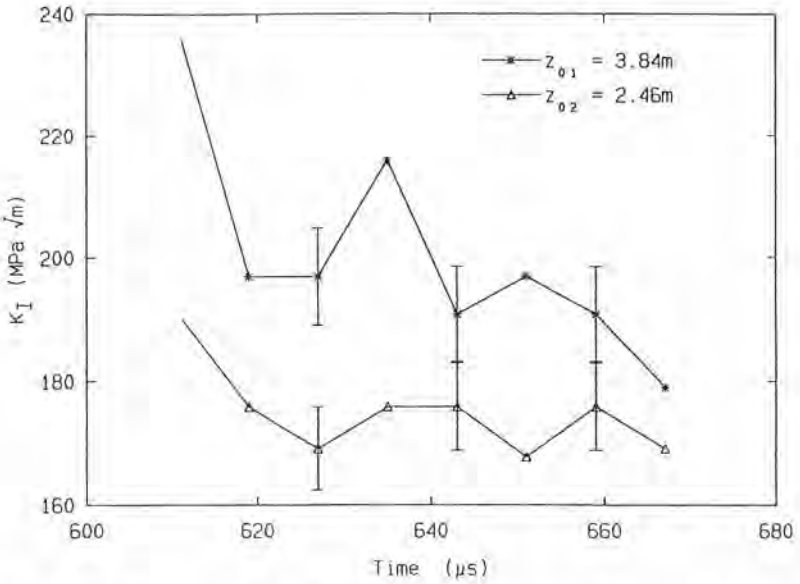

Figure 10.15. Time variation of apparent stress intensity factors as inferred from bifocal caustic curves using the classical elastodynamic analysis of caustics. Initial curves are outside the crack three-simensional zone during crack growth. (Reflection, 4340 steel.)

for a propagating crack in 4340 steel. The apparent stress intensity factors obtained from the diameters of the bifocal caustics pairs are shown as functions of time from impact. Crack initiation was achieved 620 μs after impact.

After that time the crack propagated with a velocity in the range of 1,000–2,000 m/s. The object plane distances used in this experiment were z_{01} = 3.10 m and z_{02} = 1.84 m. The region of possible measurement uncertainty is indicated as vertical error bars. It is interesting to note that the larger measured apparent stress intensity factor corresponds to the larger z_0 value and hence the larger initial curve radius. Also as time goes on, and transients tend to die off the difference is reduced. Differences up to 30% in the measured values of K_I^d are seen in these experiments despite the fact that the initial curve radii r_{01} and r_{02} *were always kept greater than one-half the specimen thickness during crack growth*. Unlike the results of Rosakis and Ravi-Chandar [34] for the static case [Figs. 10.10(a) 10.10(b)], these differences persisted even for $r_0/h \geq 0.5$. This indicates that in the dynamic tests the plane stress region surrounding the near-tip region was not K_I^d dominant and that the analysis of caustics presented above was incapable of furnishing the same value of stress intensity factor from two simultaneously obtained caustic patterns generated *outside* the crack-tip 3D zone.

The above observations together with recent experimental evidence obtained using the CGS technique (see sec. B.4 of this chapter) strongly suggest that a more elaborate analysis of the optical method of caustics is necessary to ensure the usefulness of this technique as an accurate diagnostic tool in dynamic fracture studies. This is particularly true for dynamic fracture experiments in laboratory size specimens where the existence of wave reflections almost always precludes the attainment of pure steady-state conditions. In addition we expect that the transient nature of dynamic crack growth becomes especially important at times close to both crack initiation and crack arrest. At such times the possibility of lack of K_I^d dominance is enhanced and thus the classical analysis of caustics becomes questionable. Similar conclusions can also be drawn on the basis of an ingenious study performed recently by Ningham and Shukla [51]. In their work, caustics, interpreted in the classical sense, and photoelasticity, interpreted by means of a *steady-state* higher-order expansion, were used to obtain stress intensity factor histories for the same specimen configuration and loading. Differences of up to 30% in $K_I^d(t)$ were observed which indicates that the assumptions made in interpreting the optical patterns are very crucial. Although the *steady-state* higher-order expansion used in the photoelastic study is not strictly accurate, it is still an improvement over the assumption of K_I^d dominance used by the classical interpretation of caustics since it provides more flexibility over K_I^d dominance. An improved higher-order expansion, derived for the most general case of transient crack growth at arbitrary crack-tip velocity histories will be presented in the next section.

A.5 Interpretation of Caustics on the Basis of a Higher-Order, Transient, Elastodynamic Analysis

The experimental results (obtained by means of bifocal caustic pairs), discussed in the previous section, clearly show the inadequacy of the classical analysis of caustics in accurately measuring the dynamic stress intensity factor during *highly transient* crack growth events. Even if the initial curve radius lies well outside the regions of near-tip three-dimensionality, where plane stress conditions are achieved, the assumption of K_I^d dominance [validity of relation (22) outside the three dimensional zone] clearly fails, resulting in the inconsistencies described above.

In this section, we provide an explanation of this phenomenon by relaxing the assumption of K_I^d dominance. While dynamic caustic patterns have conventionally been analyzed under the assumption of K_I^d dominance, the use of higher-order terms has been the recent practice in the method of photoelasticity. (See Dally, Fourney, and Irwin [52], Chona, Irwin, and Sanford [53], Sanford and Chona [54], Chona and Sanford [55], and Shukla and

Chona [56].) However, all available higher-order elastodynamic solutions thus far have been for the case of *steadily propagating cracks*, and the applicability of such solutions to highly transient problems is still questionable. Nonetheless, use of a higher-order steady-state expansion is bound to be an improvement over the assumption of strict K_I^d dominance.

We will now relax the assumption of K_I^d dominance and examine the validity of a *transient* higher-order expansion for dynamic crack growth which has become available recently by Freund and Rosakis [46], and Rosakis, Liu, and Freund [47].

A.5.1 Transient Crack-Tip Fields

Consider a planar, Mode-I crack that grows through a plate specimen composed of a homogeneous, isotropic, linearly elastic solid. The midplane of the specimen occupies a region in the x_1, x_2 plane, and the crack-tip translates with a *nonuniform* velocity $v(t)$. A translating orthonormal coordinate frame $\{0; x_1, x_2, x_3\}$ is introduced with its origin at the midpoint of the moving crack front and oriented with the x_1 axis aligned with the direction of crack growth. If a generalized plane stress assumption is made then a three-term expansion for the thickness average of the first stress invarient $\hat{\sigma}_{11} + \hat{\sigma}_{22}$ at the vicinity of the propagating crack tip can be expressed (Freund and Rosakis [46]) as

$$\begin{aligned}\frac{\hat{\sigma}_{11} + \hat{\sigma}_{22}}{2\rho(c_l^2 - c_s^2)} &= \frac{3v^2}{4c_l^2} A_0(t) r_l^{-1/2} \cos\frac{\theta_l}{2} + 2\frac{v^2}{c_l^2} A_1(t) \\ &+ \left\{ \frac{15v^2}{4c_l^2} A_2(t) \cos\frac{\theta_l}{2} \right. \\ &+ D^1[A_0(t)] \left[\left(1 - \frac{v^2}{2c_l^2}\right) \cos\frac{\theta_l}{2} + \frac{v^2}{8c_l^2} \cos\frac{3\theta_l}{2} \right] \\ &+ \frac{1}{2} B(t) \left[\left(1 - \frac{v^2}{2c_l^2}\right) \cos\frac{\theta_l}{2} - \left(1 - \frac{5v^2}{8c_l^2}\right) \cos\frac{3\theta_l}{2} \right. \\ &\left. \left. + \frac{v^2}{16c_l^2} \cos\frac{7\theta_l}{2} \right] \right\} r_l^{1/2} + O(r_l),\end{aligned} \tag{28}$$

where

$$\begin{aligned} r_{l,s}^2(t) &= x_1^2 + \alpha_{l,s}^2(t) x_2^2, \\ \theta_{l,s}(t) &= \tan^{-1}\left(\frac{\alpha_{l,s}(t) x_2}{x_1}\right). \end{aligned} \tag{29}$$

$$\alpha_{l,s}^2(t) = 1 - \frac{v^2(t)}{c_{l,s}^2},$$

$$A_0(t) = \frac{4}{3\mu\sqrt{2\pi}} \frac{1 + \alpha_s^2}{D(v)} K_I^d(t),$$

$$D^1[A_0(t)] = -\frac{3v^{1/2}(t)}{\alpha_l^2 c_l^2} \frac{d}{dt}\left[v^{1/2}(t) A_0(t)\right]$$

$$= \frac{4v^{1/2}(t)}{\mu\sqrt{2\pi}\alpha_l^2 c_l^2} \frac{d}{dt}\left(v^{1/2}(t) \frac{1 + \alpha_s^2}{D(v)} K_I^d(t)\right),$$

$$B(t) = \frac{3v^2(t)}{2\alpha_l^4 c_l^4} A_0(t) \frac{dv(t)}{dt}$$

$$= \frac{2v^2(t)}{\mu\sqrt{2\pi}\alpha_l^4 c_l^4} \frac{1 + \alpha_s^2}{D(v)} K_I^d(t) \frac{dv(t)}{dt},$$

$$D(v) = 4\alpha_l \alpha_s - (1 + \alpha_s^2)^2.$$

The above expansion was obtained by considering the *fully transient* crack growth problem. No steady-state assumption was allowed. Its first team is identical to the result of Eq. (22) and its coefficient $A_0(t)$ depends on $K_I^d(t)$ and $v(t)$, but not on their time derivatives. On the other hand, the functions $D^1[A_0(t)]$ and $B(t)$ that appear in the higher-order terms are directly linked to the time derivatives of $K_I^d(t)$ and $v(t)$. The coefficients $A_1(t)$ and $A_2(t)$ are undetermined by the asymptomatic analysis. Their functional form can be determined for particular initial/boundary-value problems.

If the crack-tip velocity $v(t)$ is constant, i.e., $\dot{v}(t) = 0$, and therefore $B(t) = 0$, we obtain the asymptotic stress field corresponding to transient crack growth under constant velocity and varying stress intensity factor. (See Freund and Rosakis [46], also see Sec. B.5 of this chapter.) A classical example of such a constant velocity, but transient crack problem, is the one analyzed by Broberg (see Freund [44] and Freund and Rosakis [46]). Furthermore, if the time derivative of the dynamic stress intensity factor, $K_I^d(t)$, is also zero, both $D^1[A_0(t)]$ and $B(t)$ will vanish. Then we obtain the familiar results of the asymptotic stress field, up to three terms, obtained by means of a steady-state expansion. (Dally, Fourney, and Irwin [52].)

A.5.2 Caustic Mapping Equations for Transient Elastodynamic Crack Growth

Substitution of Eq. (28) for the first stress invariant into the optical path difference relation (21), and using Eq. (10), the equations for the caustic mapping can be obtained. The complete form of such equations has been

derived by Liu, Rosakis, and Freund [57]. However, in most cases of practical significance crack-tip speeds do not exceed a speed of $0.20c_l$ or approximately $0.5c_R$ where c_R is the material Rayleigh wave speed in plane stress. It is thus felt that assuming that $v/c_l << 1$ will lead to a useful and accurate simplification for the mapping equations which now become

$$X_1 = r_l \cos\theta_l + \hat{K}(t) r_l^{-3/2} \cos\frac{3\theta_l}{2} - \hat{A}(t) r_l^{-1/2} \cos\frac{\theta_l}{2} \tag{30}$$
$$-\frac{1}{2}\hat{B}(t) r_l^{-1/2}\left(\cos\frac{\theta_l}{2} - \cos\frac{5\theta_l}{2}\right),$$
$$X_2 = \frac{r_l \sin\theta_l}{\alpha_l} + \alpha_l\left[\hat{K}(t) r_l^{-3/2} \sin\frac{3\theta_l}{2} - \hat{A}(t) r_l^{-1/2} \sin\frac{\theta_l}{2}\right.$$
$$\left.+\frac{1}{2}\hat{B}(t) r_l^{-1/2}\left(3\sin\frac{\theta_l}{2} + \sin\frac{5\theta_l}{2}\right)\right],$$

where

$$\hat{K}(t) = z_0\, ch\rho(c_l^2 - c_s^2)\frac{3v^2}{4c_l^2} A_0(t) = \frac{z_0 chF(v)}{\sqrt{2\pi}} K_I^d(t),$$
$$\hat{A}(t) = z_0\, ch\rho(c_l^2 - c_s^2)\left(\frac{15v^2}{4c_l^2} A_2(t) + D^1[A_0(t)]\right),$$
$$\hat{B}(t) = z_0\, ch\rho(c_l^2 - c_s^2)\, B(t),$$
$$F(v) = \frac{(\alpha_l^2 - \alpha_s^2)(1 + \alpha_s^2)}{4\alpha_l\alpha_s - (1 + \alpha_s^2)^2}.$$

Following the discussion presented in the previous sections, the equation for the initial cure is now obtained by requiring that the Jarobian of the above transformation vanishes. This requirement leads to the following equation for the initial curve:

$$\left(1 - \frac{3}{2}(1 - \alpha_l^2)\hat{K}(t) r_l^{-5/2} \cos\frac{5\theta_l}{2} - \frac{9}{4}\alpha_l^2 \hat{K}^2(t) r_l^{-5}\right) \tag{31}$$
$$+\left(\frac{1}{2}(1 - \alpha_l^2)\hat{A}(t) r_l^{-3/2} \cos\frac{3\theta_l}{2} + \frac{3}{2}\alpha_l^2 \hat{K}(t)\hat{A}(t) r_l^{-4} \cos\theta_l\right.$$
$$\left.-\frac{1}{4}\alpha_l^2 \hat{A}^2(t) r_l^{-3}\right)$$
$$-\hat{B}(t)\left[\frac{1}{4}\left((3 + 5\alpha_l^2)\cos\frac{3\theta_l}{2} - 3(1 - \alpha_l^2)\cos\frac{7\theta_l}{2}\right) r_l^{-3/2}\right.$$

$$- 3\alpha_l^2 \hat{K}(t) r_l^{-4} \cos\theta_l + \frac{1}{4}\hat{A}(t)(1 + 3\cos 2\theta_l) r_l^{-3}$$

$$+ \frac{1}{8}\hat{B}(t)(1 + 3\cos 2\theta_l - 4\cos 3\theta_l) r_l^{-3} \Big] = 0.$$

The equation of the caustic curve itself is now given by Eq. (30) under the restriction provided by Eq. (31).

In the absence of crack-tip acceleration $\dot{v}(t) = 0$, $\hat{B}(t)$ vanishes. If further $\dot{K}_I^d(t) = 0$, $D^1[a_0(t)]$ also vanishes. In such a case, Eqs. (30) and (31) describe the caustic curves corresponding to steady state crack growth evaluated on the basis of a three-term steady-state expansion for the stresses. If in addition $A_2(t)$ vanishes, these relations exactly reduce to Eqs. (23) and (24) obtained under the assumption of K_I^d dominance (Rosakis [28]).

For stationary cracks ($v = 0$) $D^1[A_0(t)]$, $B(t)$ and $\hat{B}(t)$ all vanish even if $\dot{K}_I \neq 0$. Depending on whether the loading is dynamic or not $A_2(t)$ may be either a constant or a function of time. If $A_2(t)$ happens to vanish, then a situation of K_I dominance is established outside the near-tip three-dimensional zone and the equations of the caustics reduce to those of an epicycloid (Theocaris [7]).

Equations (30) and (31) are still complicated. Nevertheless, given experimentally obtained caustic patterns and an appropriate numerical scheme, they can be used to obtain the values of $\hat{K}(t)$, $\hat{A}(t)$, and $\hat{B}(t)$ as functions of time if, in addition, $v(t)$ and thus $\dot{v}(t)$ are independently known. It should be noted at this point that $\hat{B}(t)$ is related to $\hat{K}(t)$ by

$$\hat{B}(t) = \frac{2\dot{v}(t)}{\alpha_l^4 c_l^2}\hat{K}(t), \tag{32}$$

and thus is not an independent variable.

In an attempt to retain some of the simplicity of the classical analysis of caustics one can introduce a simplifying assumption regarding the nature of the initial curve. Assuming that the initial curve remains a circle of radius r_0, i.e.,

$$r_l = r_0(t) = \left(\frac{3}{2}\alpha_l \hat{K}(t)\right)^{5/2} \tag{33}$$

$$= \left(\frac{3}{2}\frac{\alpha_l z_0 c h F(v)}{\sqrt{2\pi}} K_I^d(t)\right),$$

allows us to relate the two independent unknowns $\hat{K}(t)$ and $\hat{A}(t)$ to two easily measurable dimensions of the caustic curve. As will be discussed later, the validity of the assumption regarding the initial curve [Eq. (33)] has been extensively discussed by Liu, Rosakis, and Freund [57].

The two caustic curve dimensions chosen in this analysis are the maximum transverse diameter D of the caustic and the distance between the point

of intersection of this diameter with the x_1 axis and the front of the caustic. This length will be denoted as X. These lengths are shown schematically in Fig. 10.16.

By substituting $r_l = r_0(t)$ into the mapping Eq. (30) and using Eq. (33), the parametric equations of the caustic are obtained as follows:

$$X_1 = r_0 \left\{ \cos\theta_l + \frac{2}{3}\alpha_l^{-1}\left[\cos\frac{3\theta_l}{2} - \frac{\hat{A}(t)r_0}{\hat{K}(t)}\cos\frac{\theta_l}{2} - \frac{\dot{v}(t)r_0}{\alpha_l^4 c_l^2}\left(\cos\frac{\theta_l}{2} - \cos\frac{5\theta_l}{2} \right)\right]\right\}, \tag{34}$$

$$X_2 = r_0 \left\{ \frac{\sin\theta_l}{\alpha_l} + \frac{2}{3}\left[\sin\frac{3\theta_l}{2} - \frac{\hat{A}(t)r_0}{\hat{K}(t)}\sin\frac{\theta_l}{2} + \frac{\dot{v}(t)r_0}{\alpha_l^4 c_l^2}\left(3\sin\frac{\theta_l}{2} + \sin\frac{5\theta_l}{2} \right)\right]\right\}.$$

For $\hat{A}(t)r_0/\hat{K}(t) \to 0$ and $\dot{v}(t)r_0/\alpha_l^4 c_l^2 \to 0$, Eqs. (34) reduce to the parametric equations for dynamic caustics [Eq. (26)] obtained on the basis of K_l^d dominance.

The above equations can now be used to relate D and X to the instantaneous value of the stress intensity factor $K_l^d(t)$. Letting $\theta_l = \theta_l^p$ be the angular coordinate of the point (r_0, θ_l^p) on the initial curve that maps on to the point of the caustic curve where X_2 is maximum, and observing that $D = 2X_2(\theta_l^p)$,

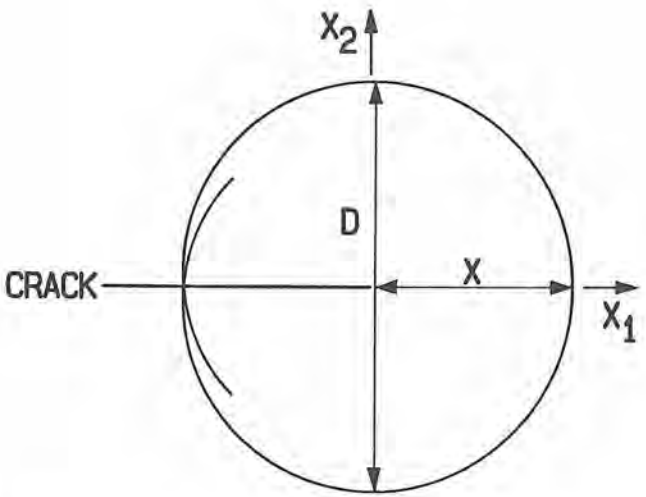

Figure 10.16. Schematic of a caustic curve. The lengths D and X necessary for data analysis are shown.

$(\partial X_2/\partial \theta t)\,(\theta_l^D) = 0$, and $X = X_1\,(0) - X_1\,(\theta_l^D)$ one obtains (Liu, Rosakis, and Freund [57])

$$K_I^d(t) = \frac{2\sqrt{2\pi}}{3\alpha_l c h z_0 F(\nu)} \left(\frac{D}{g_1\,(\theta_l^{(D)})} \right)^{5/2} \left(1 - \frac{2g_1'\,(\theta_l^{(D)})}{g_1\,(\theta_l^{(D)})} \tan \frac{\theta_l^{(D)}}{2} \right)^{-5/2} \tag{35}$$

$$\times \left(\frac{1}{2} + \sqrt{\frac{1}{4} + \frac{2\dot{v}(t)D}{\alpha_l^4 c_l^2} \frac{G_2(\theta_l^{(D)})}{[G_l(\theta_l^{(D)})]^2}} \right)^{-5/2},$$

where

$$g_l(\theta_l^{(D)}) = 2\left(\frac{\sin \theta_l^{(D)}}{\alpha_l} + \frac{2}{3} \sin \frac{3\theta_l^{(D)}}{2} \right),$$

$$g_2(\theta_l^{(D)}) = \frac{4}{3\theta_l}\left(3 \sin \frac{\theta_l^{(D)}}{2} + \sin \frac{5\theta_l^{(D)}}{2} \right),$$

and

$$G_1\,(\theta_l^{(D)}) = g_1\,(\theta_l^{(D)}) - 2g_1'\,(\theta_l^{(D)}) \tan \frac{\theta_l^{(D)}}{2},$$

$$G_2\,(\theta_l^{(D)}) = g_2\,(\theta_l^{(D)}) - 2g_2'\,(\theta_l^{(D)}) \tan \frac{\theta_l^{(D)}}{2}.$$

The angle θ_l^D that appears in the above equations is the root of the following trigonometric equation:

$$\frac{X}{D} = \frac{f_1\,(\theta_l^{(D)})}{G_1\,(\theta_l^{(D)})} \left(\frac{1}{2} + \sqrt{\frac{1}{4} + \frac{2\dot{v}(t)X}{\alpha_l^4 c_l^2} \frac{f_2\,(\theta_l^{(D)})}{[f_1\,(\theta_l^D)]^2}} \right) \tag{36}$$

$$\times \left(\frac{1}{2} + \sqrt{\frac{1}{4} + \frac{2\dot{v}(t)D\ G_2\,(\theta_l^{(D)})}{\alpha_l^4 c_l^2\,[G_1\,(\theta_l^D)]^2}} \right),$$

where

$$f_1\,(\theta_l^{(D)}) = 1 + \frac{2}{3\theta_l} - \left[1 + \frac{2}{\theta_l^2}\left(\sec \frac{\theta_l^{(D)}}{2} - 1 \right) \right] \cos \theta_l^{(D)}$$

$$+ \frac{2}{\theta_l}\left(\frac{2}{3} - \sec \frac{\theta_l^{(D)}}{2} \right) \cos \frac{3\theta_l}{2},$$

$$f_2\,(\theta_l^{(D)}) = \frac{1}{3\theta_l}\left[\left(4 - 3 \sec \frac{\theta_l^{(D)}}{2} \right) \cos \frac{\theta_l^{(D)}}{2} \right.$$

$$\left. + \left(4 - 5 \sec \frac{\theta_l^{(D)}}{2} \right) \cos \frac{5\theta_l^{(D)}}{2} \right].$$

A similar relation for $\hat{A}(t)$ can also be obtained. In addition, $\hat{B}(t)$ can also be determined through Eqs. (32) and (35).

In an experimental situation caustic patterns are photographed and D and X are measured. Equation (36) is then used to obtain θ_I^p, substitute it in Eq. (35) and thus obtain K_I^d.

As demonstrated by Liu, Rosakis, and Freund [57], Eqs. (35) and (36) reduce to Eq. (27) for the case of pure K_I^d dominance. For this case $\dot{v}(t)$ and $\hat{A}(t)$ both vanish and θ_I^p is a weak function of crack-tip velocity and such that $\theta_I^p \sim 72°$.

The major assumption pivotal to the derivation of the relation between K_I^d, D, and X [Eqs. (35) and (36)] is the circularity of the initial curve [Eq. (33)]. The accuracy of this assumption is discussed in detail by Liu, Rosakis, and Freund [57]. In their work, a highly transient crack problem with an a priori known $K_I^d(t)$ history (sudden extension of a stationary crack with initial velocities up to $0.6c_s$) was used to numerically construct caustic patterns and to demonstrate that even for short times after crack initiation [high values of $D_I^1\{A_0\}$ and thus $\hat{A}(t)$], the initial curve remained virtually circular with radius $r_0 \sim [3/2\alpha_I\hat{K}(t)]^{5/2}$. The numerically computed caustic curves were then analyzed to obtain $K_I^d(t)$ as would be done in an experiment and to compare with the theoretically known $K_I^d(t)$ time history. When the caustics were analyzed on the basis of Eq. (27) (classical analysis) errors in excess of 50% of the theoretical values were obtained at times close to crack initiation. On the other hand, when Eqs. (35) and (36) were used in the analysis of the caustic patterns the theoretical value of $K_I^d(t)$ was obtained to within 1%. This clearly indicates that the improved analysis of caustics, based on the higher-order transient expansion, presented above, is capable of providing accurate values of stress intensity factor history.

Relations (28)–(36) show that the time derivatives of the velocity and stress intensity factor histories [see definitions of $\hat{A}(t)$] contribute to the amplitudes of the higher-order terms for the stresses and also influence the mapping equations for the caustics. As a result, one can imagine situations in which K_I^d dominance may exist for a stationary crack of a given length in a specific specimen, geometry, while K_I^d dominance *may not* prevail during transient crack growth [$\dot{K}_I^d(t) \neq 0$, and or $\dot{v}(t) \neq 0$] in an identical specimen geometry and same instantaneous crack length. An experimental example of such a situation will be discussed in the section of this chapter devoted to dynamic fracture applications of CGS (section B). In such cases, the classical analysis of caustics would clearly be inapplicable and may prove to be a serious source of error (also see Krishnaswamy, Tippur, and Rosakis [48]).

A.5.3 Concluding Remarks

The shortcomings of the classical analysis of caustics discussed here may have far-reaching consequences. In particular, caution should be exercised in the interpretation of experimental measurements obtained by caustics in

the past, especially when highly transient crack problems were studied by the technique. The implications of the above on the investigation of fundamental physical phenomena in dynamic fracture and in particular on the investigation of the existence of a unique relation between dynamic fracture toughness and crack-tip speed have been discussed by Freund and Rosakis [46]. Such issues will also be discussed later in this chapter in relation to full field, dynamic, crack-tip measurements performed by means of the coherent gradient sensor method (CGS). Like caustics, CGS is sensitive to gradients of $(\hat{\sigma}_{11} + \hat{\sigma}_{22})$ but in addition it is a full field method. As such, it has the capability of revealing the transient structure of the near-tip field and to directly demonstrate the existence or lack of K_I^d dominance.

A.6 Application of Caustics to the Investigation of Elastoplastic Crack Problems

Most structural materials that contain cracks undergo substantial plastic deformation under rising load prior to onset of crack growth. In many cases, including standard specimen configurations, a large plastic zone develops around the crack-tip and there is no region of the body over which a stress intensity factor controlled elastic field prevails. The linear elastic fracture toughness approach to fracture resistance characterization is then not applicable and other criteria, such as the critical J must be adopted. Methods for measuring values of J for ductile fracture specimens are available but the methods are indirect, in general, in the sense that values of J are inferred from values of other measured quantities, typically load and deflection data. In this section, attention is focused on points deep within the crack-tip plastic zone, and a means of inferring values of J from the local deformation field is discussed.

As discussed, in Sec. A.4, the *classical* analysis of caustics for cracks in linear elastic solids proceeds on the basis of the assumption of K_I dominance. It is important to observe that within the framework of the assumption of K_I dominance, the deformed shape of a thin plate specimen surface near a crack-tip is known up to a scalar amplitude, which is proportional to K_I. Thus, success of the method of caustics is based on the fact that, with a suitable optical arrangement, the light pattern obtained by reflecting parallel incident light from the specimen surface near the crack tip provides a direct measure of the stress intensity factor.

Once the idea of the method is described in this way, it becomes clear that applicability of the technique does not hinge on the material in the crack-tip region responding in an elastic manner. Instead, the key feature is that the deformed shape of the specimen surface (that is, the reflecting surface) in the crack-tip region is known up to a scalar amplitude. Although the mechanics of elastic-plastic fracture is not as fully developed as elastic frac-

ture mechanics, the available asymptotic analyses of near-tip fields in power-law hardening materials suggest that this situation may prevail for these cases as well. Within the framework of plane stress analysis, with small strains and proportional stress histories for *stationary cracks*, the value of Rice's J integral has been proposed as a plastic intensity factor. This viewpoint was adopted by Rosakis and Freund [30] and Rosakis, Ma, and Freund [31]. It was thus assumed that J provides a suitable scalar amplitude for the deformed shape of the surface of an elastic-plastic fracture specimen (J dominance) and a means of directly measuring this amplitude was proposed. Although there are methods available for measuring J values for ductile materials, they apply only for rate-independent materials subjected to quasi-static loading. While the direct optical method being discussed here has drawbacks of its own, its use is not subject to the same limitations on rate of loading or material response.

A.6.1 Stationary Cracks in Elastic-Plastic Solids (the HRR Field)

Consider a large plate of elastic-plastic material that exhibits power-law hardening behavior. Suppose the plate is initially of uniform thickness h and that is contains a long through-crack. The plate is subjected to edge loading which results in a plane stress opening mode of deformation. If the midplane of the plate undergoes no transverse displacement, then the normal displacement of the plate surface $u_3(x_1, x_2)$ is

$$u_3(x_1, x_2) = f(x_1, x_2) = h \int_0^{1/2} \varepsilon_{33}(x_1, x_2, x_3) d(x_3/h), \tag{37}$$

where the orientation of Cartesian axes shown in Fig. 10.6(a) is assumed and ε_{33} is the total strain in the thickness direction and $x_3 = -f(x_1, x_2)$ is the equation of the specimen surface after deformation. If a state of generalized plane stress is assumed the above relation reduces to

$$u_3(x_1, x_2) = f(x_1, x_2) = \frac{h}{2} \varepsilon_{33}(x_1, x_2), \tag{38}$$

where $\varepsilon_{33}(x_1, x_2)$ is the thickness average of the total strain in the thickness direction.

Hutchinson [58] and Rice and Rosengren [59] showed that for two-dimensional deformation states the strain components in the crack-tip region scale with the value of J for a power-law hardening material. They considered a monotonically loaded stationary crack in an incompressible material de-

scribed by a J_2-deformation theory of plasticity and a relationship between post-yield strain ε_{ij} and stress σ_{ij} of the form

$$\frac{\varepsilon_{ij}}{\varepsilon_0} = \frac{3}{2}\left(\frac{\sigma_e}{\sigma_0}\right)^{n-1}\frac{S_{ij}}{\sigma_0}, \tag{39}$$

where

$$S_{ij} = \sigma_{ij} - \frac{1}{3}\sigma_{ij}\sigma_{kk}, \qquad \sigma_e^2 = \frac{3}{2}S_{ij}S_{ij}, \tag{40}$$

and σ_0 is the tensile yield stress, ε_0 is the equivalent tensile yield strain, and n is the hardening exponent. By introducing the preceding assumptions, they observed that, within a small strain formulation, the asymptotic strain distribution in the crack-tip region is

$$\varepsilon_{ij} \to \varepsilon_0\left(\frac{J}{\sigma_0\varepsilon_0 I_n r}\right)^{n/(n+1)} E_{ij}(n,\theta), \tag{41}$$

as $r \to 0$ in a polar coordinate system with origin at the crack-tip. The angular factors E_{ij} in Eq. (41) depend on the mode of loading and on the hardening exponent. The dimensionless quantity I_n, decreases from $I_n = 5$ for $n = 1$–2.57 for infinitely large values of n for cases of generalized plane stress. The intensity factor J in Eq. (41) is the value of Rice's J integral. The singular Eq. (41) is customarily referred to as the HRR singularity. The asymptotic result Eq. (41) was derived under the further assumption that the dependence of the local field on the polar coordinates r and θ is indeed separable.

For plane deformations, the J integral is defined for any path of integration C by

$$J = \int_C (W\mathrm{n}_1 - n_i\sigma_{ij}u_{j,1})dC, \tag{42}$$

where W is the local stress work density, n_1 is the x_1 component of the unit vector normal to C, and u_i is the particle displacement vector. The integral has the well-known property of path independence, that is, $J = 0$ for *any* simple closed path in the body in the absence of body forces. This implies that J has the same value for all paths that begin on one traction-free face of a crack in a plane with normal in the x_2 direction and that end on the opposite traction-free face of the crack. Because the path of integration can be chosen to be arbitrarily close to the crack-tip, J has been interpreted as a measure of the strength of the crack-tip singular field, a role that is obvious from the form of Eq. (41). Based on the observation that J is a characterizing parameter for the crack-tip field, it has been suggested that a condition for onset of crack growth is the attainment of a critical value of J. This seems reasonable, provided that the one-parameter characterization remains valid and

that the one-parameter field prevails over a region large in size compared to the fracture process zone (J dominance). The interest in measuring values of J for ductile materials stems from the potential usefulness of this suggested criterion.

In view of the assumed incompressibility of material response, the strain in the thickness direction which appears in Eq. (38) is related to the in-plane strains by

$$\varepsilon_{33} = -(\varepsilon_{11} + \varepsilon_{22}) = -(\varepsilon_{rr} + \varepsilon_{\theta\theta}), \tag{43}$$

For specified material parameters and a given value of J, the in-plane strains are known from Eq. (41), the out-of-plane strain is computed from Eq. (43), and the shape of the reflecting surface is then given by Eq. (38). Thus, for points near the crack-tip, the shape of the reflecting surface is known up to a scalar amplitude, namely the plastic strain intensity J. In the next section, the relationship between the magnitude of J and the size of the shadow spot obtained by reflecting parallel incident light from this surface is established.

It should be noted that Eq. (43) will provide an overestimate of lateral contraction for given in-plane strains because for most materials the elastic part of the local deformation is not incompressible although the plastic part may be so. For points close enough to the crack-tip for the plastic strain to dominate the elastic strain, however, the total strain is expected to satisfy Eq. (43) to an acceptable degree.

A.6.2 Analysis of Caustics on the Basis of the Assumption of the Validity of a Plane Stress HRR Asymptotic Crack-Tip Field (J Dominance)

According to the assumption of J dominance, Eqs. (38), (41), and (43) can be used to furnish the shape of the reflecting surface $f(x_1, x_2)$ as follows:

$$f(x_1, x_2) = \frac{1}{2}\varepsilon_0 h \left(\frac{J}{\sigma_0 \varepsilon_0 I_n r} \right)^{n/(n+1)} (E_{rr} + E_{\theta\theta}). \tag{44}$$

Numerical values of the angular variations E_{ij} are available for many values of hardening exponent n from the work of Shih [60]. Again, Eq. (44) represents the normal displacement of points on the initially plane specimen surface due to deformation. For an initial curve that is well within the crack-tip plastic zone where the HRR field can be expected to dominate, the caustic mapping Eqs. (10) take the form

$$\mathbf{X} = \mathbf{x} + \varepsilon_0 z_0 h \left(\frac{J}{\varepsilon_0 \sigma_0 I_n} \right)^{n/(n+1)} \nabla \left(\frac{E_{rr} + E_{\theta\theta}}{r^{n/(n+1)}} \right). \tag{45}$$

In polar form these equations become:

$$X_1 = r\cos\theta + G\,r^{-(2n+1)/(n+1)}\left(\frac{n}{n+1}\psi\cos\theta + \psi'\sin\theta\right), \tag{46}$$

$$X_2 = r\sin\theta + G\,r^{-(2n+1)/(n+1)}\left(\frac{n}{n+1}\psi\sin\theta + \psi'\cos\theta\right),$$

where

$$G = \varepsilon_0 z_0 h\left(\frac{J}{\varepsilon_0\sigma_0 I_n}\right)^{n/(n+1)}, \quad \psi = E_{rr} + E_{\theta\theta}, \tag{47}$$

and the prime denotes the derivative with respect to θ.

If the determinant of the Jacobian matrix of the transformation equation (46) is set equal to 0, then the result is a quadratic equation for $r^{(3n+2)/(n+1)}$ in which the coefficients depend on ψ, ψ', and ψ'', as well as on the hardening exponent n. The root of the quadratic equation is

$$r(\theta,n)^{(3n+2)/(n+1)} = G\,R(\theta,n), \tag{48}$$

where

$$\begin{aligned} 2R(\theta,n) = {} & \left[\left(\frac{n}{n+1}\right)^2\psi + \psi''\right] + \left\{\left[\left(\frac{n}{n+1}\right)^2\psi + \psi''\right]^2\right. \\ & + 4\,\frac{2n+1}{n+1}\left[\left(\frac{n}{n+1}\right)^2\psi^2 - \frac{n}{n+1}\psi\psi''\right. \\ & \left.\left. + \frac{2n+1}{n+1}(\psi')^2\right]\right\}^{1/2}. \end{aligned} \tag{49}$$

Equation (48) gives the *initial curve* on the specimen surface for a given intensity of local deformation field. Then, substitution of Eq. (48) into Eq. (46) yields the equation of the corresponding caustic curve in the X_1, X_2 plane, parametric in the angle θ,

$$\begin{aligned} X_1 = {} & G^{(n+1)/(3n+2)}\,R^{(n+1)/(3n+2)} \\ & \left[\cos\theta + R^{-1}\left(\frac{n}{n+1}\psi\cos\theta + \psi'\sin\theta\right)\right], \end{aligned} \tag{50}$$

$$\begin{aligned} X_2 = {} & G^{(n+1)/(3n+2)}\,R^{(n+1)/(3n+2)} \\ & \left[\sin\theta + R^{-1}\left(\frac{n}{n+1}\psi\sin\theta + \psi'\cos\theta\right)\right] \end{aligned}$$

for values of θ in the range $-\pi < \theta < \pi$.

The shape of the caustic curve depends only on the distribution of plastic strains in the crack-tip region. The absolute size of the caustic curve, on the other hand, depends on the strength of the plastic strain singularity, the bulk material properties, the geometrical parameters, and the optical parameters. In fact, Eq. (50) is a relationship among all of these parameters. Thus, if the values of the material, geometrical and optical parameters are known, then Eq. (50) provides a relationship between the size of the caustic curve D and the strength of the plastic singularity J. Adopting the maximum transverse diameter $D/2 = \max(X_2)$ as the characteristic dimension, the intensity of the strain singularity can be expressed as (see Rosakis, Ma, and Freund [31]):

$$J = S_n \frac{\sigma_0^2}{E} \left(\frac{E}{\sigma_0 z_0 h} \right)^{(n+1)/n} D^{(3n+2)/n}. \tag{51}$$

Equation (51) is the main result of this section. It is obtained under the assumption of plane stress J dominance and is the equivalent of relation (27) which was obtained on the basis of the assumption of K_I dominance in elastic fracture mechanics.

All of the parameters that appear in Eq. (51) are determined from prior knowledge of the material behavior or from the experimental setup. The coefficient S_n is a function of n only and its values have been tabulated by Rosakis, Ma, and Freund [31]. It should be noted that for $n > 5$ the value of S_n is almost indistinguishable from the asymptotic value 0.072 for large n. For a nonhardening material ($n \to \infty$), Eq. (51) reduces (see Freund and Rosakis [30]) to

$$J = \frac{\sigma_0 D^3}{13.5 z_0 h}. \tag{52}$$

Likewise, for an elastic material ($n = 1$), it is well-known [see Eq. (27)] that the stress intensity factor K_I is proportional to the caustic diameter D raised to the power 5/2. That Eq. (51) is also consistent with this result is evident once the relationship $J = K_I^2/E$, which applies for elastic cracks under plane stress conditions, is recalled. It should be emphasized here that complete equivalence of Eqs. (51) and (27) is obtained only for the case of elastically incompressible solids ($\nu \sim 0.5$) since the present analysis used incompressibility as one of its assumptions [see Eq. (43)].

Unlike for the elastic case, the initial curve is no longer circular and its shape depends on the hardening level of the material. The point (r^D, θ^D) of the initial curve that maps into the maximum value of X_2 of the caustic curve is at an angle θ^D measured counterclockwise from the x_1 axis. It is shown by Marchand et al. [61] that θ^D varies from 72° to 56° as n varies from 1 to ∞ and that r^D can be related to D by

$$r^D = \begin{cases} 0.385\ D, & n = 9 \\ 0.40\ D, & n \to \infty \end{cases}. \tag{53}$$

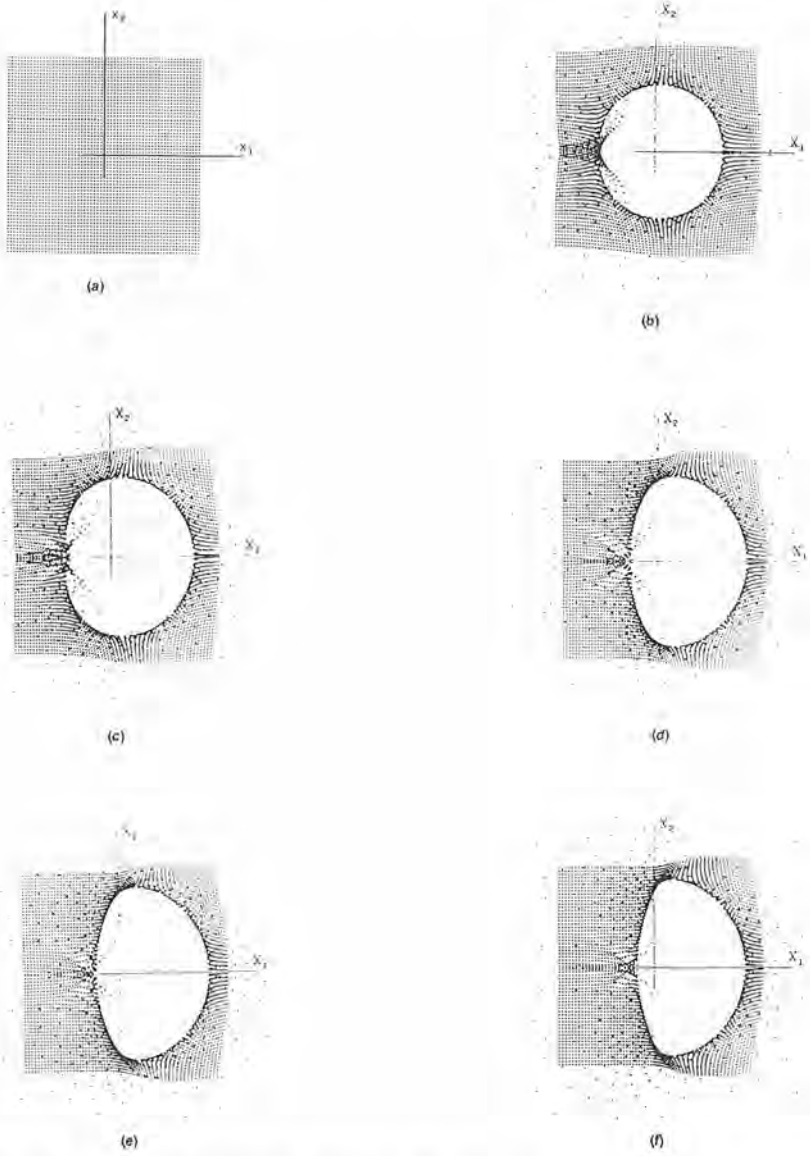

Figure 10.17. (a) Regular array of incident light rays assumed in generating the synthetic shadow spot patterns in (b)–(f), based on the HRR asymptotic field. The numerical simulation of the reflection process is shown for the following exponents: (b) $n = 1$, (c) $n = 3$, (d) $n = 9$, (e) $n = 13$, and (f) $n = 25$.

In order to more fully understand the phenomenon of shadow spot formation for a power-law hardening material, a companion study was carried out in which the full reflected optical field was simulated numerically. In this study, a square array of light rays was assumed to be normally incident on the surface of the specimen. The pattern in which these light rays pierce the plane reflecting surface of the undeformed specimen is shown in Fig. 10.17(a). These light rays were then "reflected" from a surface deformed according to Eq. (44) and the pattern in which the lines of the reflected rays pierce a screen position behind the reflecting surface was constructed. The patterns obtained for $n = 1, 3, 9, 13$, and 25 are shown in Figs. 10.17(a)–10.17(f). The anticipated features, such as the shadow spot (zero density of rays) and the caustic curve (high density of rays), are evident in these constructions of the reflected optical fields. Further insight into the physical process of shadow spot formation can be gained by comparing a straight row or column of rays in Fig. 10.17(a) to the positions into which these points map in Figs. 10.17(b)–10.17(f). These rows and columns map into curves that are tangent to the caustic curve at their common point, as is evident from the synthetic optical patterns.

Finally, a shadow spot photograph obtained by reflection from the near-tip region of a ductile steel specimen is reproduced here as Fig. 10.18 in order to illustrate the quality that might be expected in applying the ideas being proposed in laboratory testing. This photograph was produced by using light reflected from deep within the crack-tip plastic zone of a tool steel with a low rate of strain hardening in the double cantilever beam configuration. It is clear from the photograph that the surface evidence of plastic deformation extends far beyond the shadow spot.

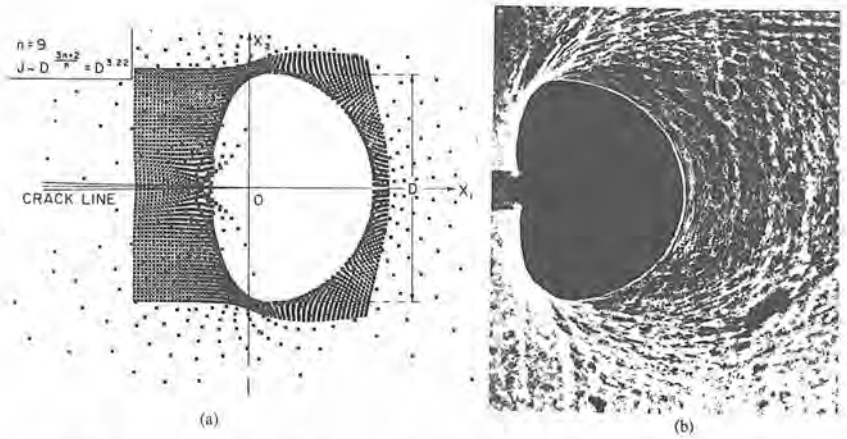

Figure 10.18. Caustics formed due to reflection of light from within a crack-tip plastic zone. (a) Numerically simulated on the basis of plane stress HRR. (b) Experimental.

For mixed mode cracks in elastic-plastic solids, caustics can also be used to measure the J integral as well as the mixity factor M^p. The analysis of the caustic patterns for this case has been presented by Zhang and Ravi-Chandar [25].

A.6.3 Caustics Obtained on the Basis of an Elastic-Plastic Plane Stress, Small Scale Yielding Finite-Element Calculation (Investigation of the *J*-Dominance Assumption)

It should be emphasized once more that Eqs. (43)–(52) have been obtained under the assumption of the validity of the HRR asymptotic field (J dominance). In this section we outline some attempts to eliminate this restriction by constructing caustics based on a full-field plane stress numerical calculation (see Narasimhan and Rosakis [62] and Zehnder, Rosakis, and Narasimhan [63]).

The numerical calculations modeled a semi-infinite crack under Mode-I plane stress small scale yielding conditions. The displacements of the singular, elastic crack-tip field, $\mathbf{u} = K_I (r/2\pi)^{1/2} \hat{\mathbf{u}} (\theta)$, were specified on a circular radius of approximately 3,400 times the smallest element. The maximum extent of the plastic zone was contained within 1/30 of this radius, ensuring small scale yielding conditions. An incremental J_2 plasticity theory was used. The material obeyed the Huber–von Mises yield criterion and followed a piecewise power-hardening law in uniaxial tension of the form

$$\frac{\varepsilon}{\varepsilon_0} = \begin{cases} \dfrac{\sigma}{\sigma_0}, & \sigma \leq \sigma_0, \\ \left(\dfrac{\sigma}{\sigma_0}\right)^n, & \sigma > \sigma_0, \end{cases}$$

with hardening exponents $n = 5, 9, \infty$. The investigation concentrates on the results for $n = 9$ since this matches the 4340 steel used in experiments to be described later. All plasticity was confined to the "active region," consisting of 1,704 four-noded isoparametric quadrilaterals. After the element nearest the crack-tip has yielded, the load, applied through the stress intensity factor K_I, or equivalently through J ($J = K_I^2/E$ for small scale yielding), was increased monotonically until the extend of the plastic zone ahead of the crack-tip was 50 $\times$ the smallest element size. For the propagation phase of this study a nodal release procedure was used to grow the crack by 20 elements. A number of crack growth histories were studied corresponding to different values of Paris's tearing modulus $T = (E/\sigma_0^2)(dJ/da)$ of 0, 1, 5, 15, 20. In the next section some of the results of the numerical analysis pertaining to the synthetic construction of caustic curves are summarized.

A.6.4 Stationary Cracks

The maximum radial extend r_p of the numerically obtained plastic zone was in good agreement with experimental measurements performed on thin compact tension specimens of 4340 steel, restricted to small scale yielding conditions (see Fig. 10.19). The value of r_p was found to be $0.25(K_I/\sigma_0)^2$. Direct comparison of the full-field-stress and deformation fields with their asymptotic, HRR counterparts revealed good agreement for $x_1 < 0.3r_p$, thus establishing the range of dominance of the asymptotic solution. On the other hand, the numerically obtained field quantities were shown to approach the elastic K_I field only well outside the plastic zone, i.e., for $x_1 > 1.5r_p$. If the initial curve satisfies the first of these restrictions, it can be expected that caustics can be interpreted on the basis of Eq. (51). On the other hand, if the second restriction is satisfied, the *elastic* analysis of caustics is sufficient and Eq. (27) can be used for the evaluation of K_I.

To provide a means of analyzing caustics that is neither dependent on the assumption of K_I of J-dominance caustic patterns were generated using the results of the finite element analysis. The out-of-plane surface displacements were smoothed using a least-squares scheme and caustics were generated by mapping light rays point by point using Eq. (10) ($\Delta s = u_3$). For a fixed value of applied load (far-field K_I level) a series of caustics was generated corresponding to different values of z_0. As discussed in detail earlier, variation in z_0 results in initial curves of different sizes and allows for the complete scanning of the near-tip region. The caustics are shown in Fig. 10.20 for values of r_0/r_p ranging from 0.19 to 1.3. It is seen that for $r_0/r_p = 0.19$, the numerically simulated caustic agrees in shape with the caustic predicted using the HRR field. On the other extreme, when $r_0/r_p = 1.3$, the numerically simulated caustic. Figure 10.20(f) exhibits the epicycloidal shape of the caustic

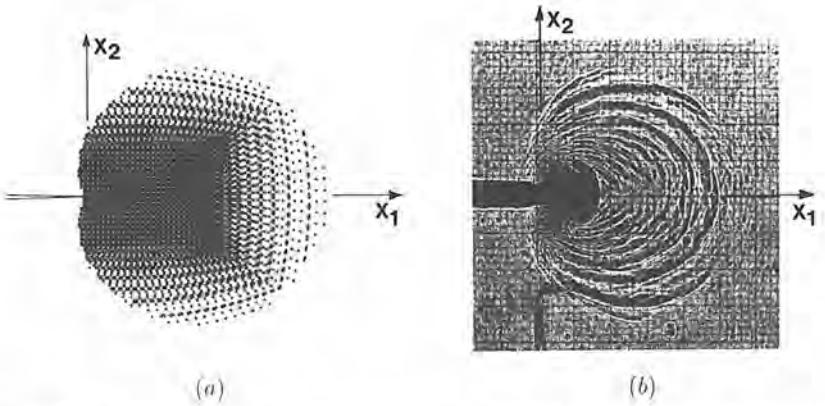

Figure 10.19. Plastic zones for a monotonically loaded stationary crack (a) numerical, (b) experimental.

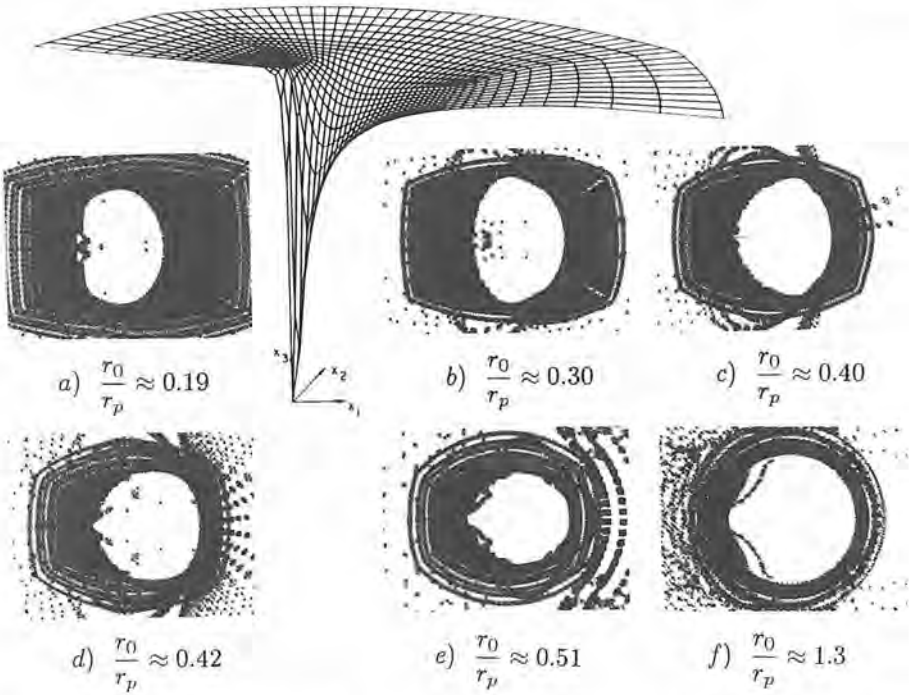

Figure 10.20. Caustics generated by using the out-of-plane displacements calculated from the numerical model. An example of the numerically generated out-of-plane displacement field is also shown.

obtained using the elastic K_I field. In the region between $r_0/r_p = 0.19$ and 1.3 there is a transition from the "HRR-like" caustic to the "elastic" caustic.

Figure 10.21 is a sequence of photographs of caustics obtained from the tensile loading of a thin compact tension specimen of 4340 carbon steel. The experimental details, specimen dimensions, etc. are described by Zehnder, Rosakis, and Narasimhan [63]. On comparing Figs. 10.20 and 10.21, it is seen that in both cases there is a transition from an HRR caustic to an elastic caustic as r_0/r_p goes from 0.19 to 1.3. It is found that both the numerical and experimental caustics retain the shape predicted by the $r^{-1/2}$ field even for r_0/r_p as small as 1.0. Thus, the effect of the plastic zone on the caustic measurement cannot be judged by mere observation of the caustic shape. The reason for the invariance in shape is explained in detail by Zehnder, Rosakis, and Narasimhan [63]. The effect of plasticity on the interpretation of caustics obtained when the initial curve lies outside the plastic zone is also discussed in the same reference.

The numerically generaged caustics were also used to establish the relationship between the caustic diameter D and the value of applied J for the two-dimensional, small scale yielding problem. This relationship is shown in Fig. 10.22 in a nondimensional form. A very small abscissa value in this

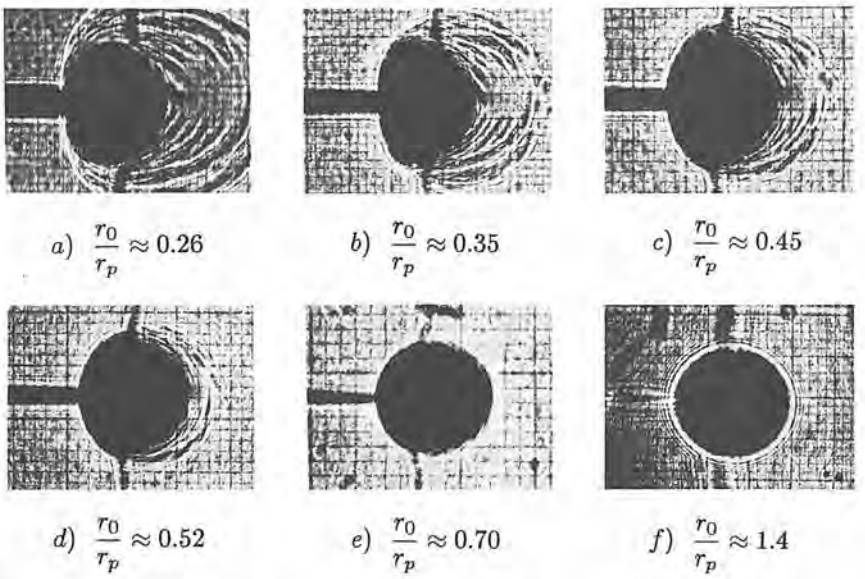

Figure 10.21. Sequence of caustics obtained for reflection of light from regions near a plastically deforming crack-tip.

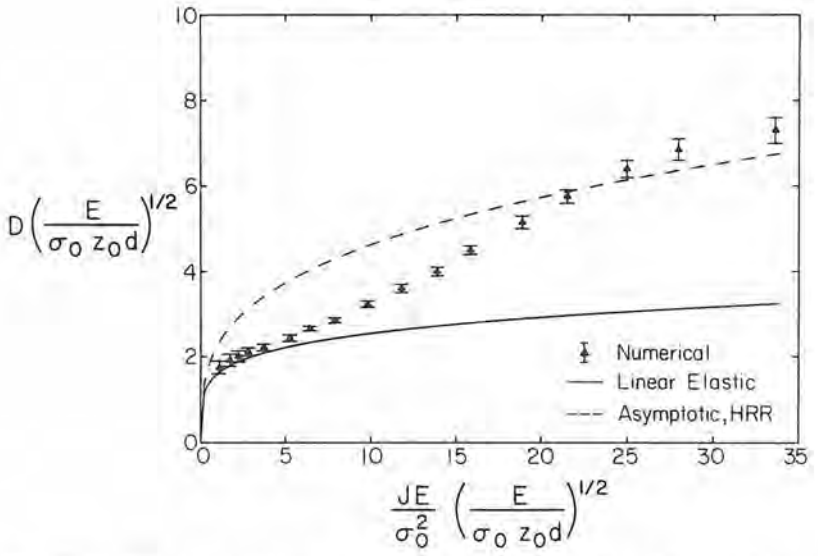

Figure 10.22. Relationship between caustic diameter and the J integral from 2D analyses.

figure (large z_0 or small J) implies that the initial curve is far away from the tip. A large abscissa value implies that the curve is far away from the tip. A large abscissa value implies that the curve is very near the tip, probably within the range of dominance of the HRR field. The solid line in the figure represents the variation of the caustic size in the K_I-dominated region, by Eq. (27), with $\nu = 0.3$. The dashed line gives the relationship for caustics generaged from the HRR-dominated region (J dominance). As can be observed from this figure, the full-field numerical results approach the elastic relation (27) for small abscissa values and the relation (51) obtained from the HRR solution for large values of the abscissa. In the intermediate region there is a transition from one relation to the other. The error bars in the figure indicate the uncertainty in the caustic diameter due to the finite-element discretization.

A.6.5 Growing Cracks

The numerical calculations were also used to simulate slow crack growth under plane stress conditions. For the specific case of an elastic-plastic power-hardening solid with a hardening exponent $n = 9$, the calculated out-of-plane displacements are used to construct caustics for the initial phases of crack growth. An example of the resulting caustic shapes is shown in Fig. 10.23. Figure 10.23(a) displays a caustic corresponding to an initial curve well within the crack-tip plastic zone of a stationary crack ($r_0/r_p \sim 0.1$). As expected, the caustic shape is similar to the one calculated on the basis of the HRR analysis.

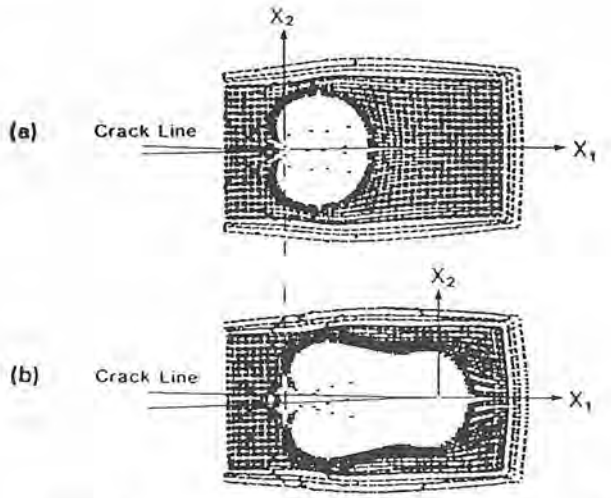

Figure 10.23. Numerical caustics from plane stress elastic-plastic analysis. Caustic (a) before crack growth and (b) after crack growth.

Figure 10.23(b) displays the caustic corresponding to an increment of crack length equal to 2/5 of the initial plastic zone size. During crack growth, the value of applied J was kept constant, or $T \equiv (E/\sigma_o^2)(dJ/da) = 0$. It is interesting to observe that the diameter of the caustic curve surrounding the new location of the crack-tip is smaller than that of the stationary crack of Fig. 10.23(a). This is true since the strain singularity at the tip of a propagating crack is weaker than that for a stationary crack. As the crack propagates, there is residual plastic deformation surrounding the initial location of the crack-tip and a wake of plastic strains along the newly created fracture surfaces. These plastic strains and the resulting residual out-of-plane displacements are responsible for the residual caustic seen behind the propagating crack-tip in Fig. 10.23(b).

A.6.6 Concluding Remarks

Very little experimental work has been done to investigate the use of caustics in elastic-plastic fracture mechanics. Preliminary experiments of this sort were reported by Rosakis and Freund [30], Marchand et al. [61], Judy and Sanford [64], and Zehnder, Rosakis, and Narasimhan [63]. These experiments investigated the dominance of HRR fields, the effect of plasticity on caustics originating from the elastic region outside the plastic zone, and the extent of the region of three dimensionality at the vicinity of the crack-tip. In particular, the effect of three dimensionality, even under small scale yielding conditions, still remains obscure and provides fertile ground for further research. (For preliminary results see Narasimhan and Rosakis [42] and Zehnder and Rosakis [65].) Even for the idealized case of a semi-infinite crack in an infinite plate of thickness h, and small scale yielding conditions, the interpretation of caustics generated within the near-tip three-dimensional zone remains an open challenge. The complication arises from the fact that, unlike the purely elastic case, at least two length scales (i.e., the plastic zone size, r_p and the specimen thickness h) are involved in the analysis of this problem.

For dynamically loaded stationary cracks, caustics have been used in conjunction with high-speed photography to measure the time history of J up to crack initiation. This preliminary investigation has been discussed in the review article by Rosakis, Zehnder, and Narasimhan [41]. The application of caustics by reflection to the study of the dynamic initiation toughness of ductile metals remains one of the most potentially rewarding research challenges in the field. The accurate dynamic measurement of J at the instant of crack initiation has remained illusive and it is believed that only local optical measurements will be capable of performing this task accurately while simultaneously also furnishing an accurate measurement of crack initiation time (for discussion, see Zehnder, Rosakis, and Krishnaswamy [66]).

A.7 Description of Experimental Arrangements

Some of the mechanical aspects of setting up an experiment using caustics are discussed here. Two possible optical setups for the recording of reflected caustics are illustrated in Fig. 10.24. The two setups are identical in principle, but each has distinct advantages for certain types of experimentation. The arrangement of Fig. 10.24(a) is useful for experiments in which it is desired to photograph caustics corresponding to many z_0 values. The arrangement of Fig. 10.24(b) is useful for experiments in which a fixed z_0 value is used and when short exposure times are desired, such as in dynamic fracture experiments.

In both setups a parallel beam of light is reflected from the flat, mirrored surface of the test specimen. The angle between the light beam and the normal to the specimen should be minimized to prevent distortions of the resulting caustics. The light source need not be monochromatic, but it must come from a point source or its equivalent so that the beam can be collimated. The incident beam can be diverging, parallel or converging; however, a parallel beam is the most useful for many applications.

In Fig. 10.24(a) the image of the caustic is focused onto a translucent screen by lens l_2. The caustic is then recorded by photographing the screen.

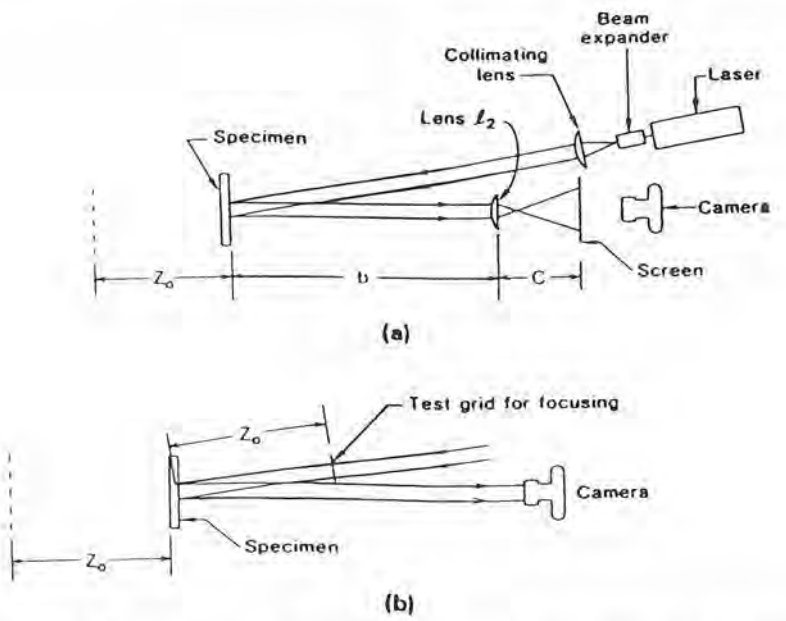

Figure 10.24. Optical setups for experiments using reflected caustics. (b) Setup for experiments in which z_0 is varied. (b) Setup for fixed z_0.

The screen can be made of ground glass or even of paper taped to a clear glass or plastic plate. The advantage of this setup is that z_0 may be accurately determined by measuring b, c, and the focal length f of lens l_2. Using these values in the thin lens equation, $(1/i) + (1/o) = 1/f$, one obtains

$$z_0 = \frac{cf}{c - f} - b.$$

The magnification from the plane at $x_3 = -z_0$ to the real screen is

$$m = \frac{i}{o} = \frac{c}{z_0 + b} = \frac{c - f}{f}.$$

The measured caustic diameter must be divided by m in the subsequent calculations. To obtain small initial curves, z_0 must be small or c large, resulting in high magnification. To obtain large z_0's and large initial curves, c must be small, resulting in low magnifications. To maintain reasonable magnification for large z_0's a long focal length l_2 should be used. The magnification from the screen to the film in the camera is determined by placing a scale on the real screen and photographing the scale superposed on the caustic pattern.

The set up in Fig. 10.24(b) is commonly applied to dynamic fracture experiments in which a fixed z_0 value is used. In this arrangement a test grid, printed on a glass plate, is placed in the incoming beam at a distance z_0 from the specimen. The camera is then focused on this grid. In the setup of Fig. 10.24(a) light is wasted due to the diffuse screen, and thus relatively long exposure times are needed. In the setup of Fig. 10.24(b) little light is wasted, and with sufficient light very short exposure times are possible. For the dynamic fracture experiments performed at the California Institute of Technology, a 15 ns exposure time is achieved with a pulsed argon ion laser at a pulsing rate up to 2,000 kHz. The high-speed camera is of the rotating mirror type. In photographing caustics one deals only with collimated light and specular reflections. Thus the camera of Fig. 10.24(b) (or the equivalent high-speed camera) must have an aperature large enough to admit the entire light beam and must not obstruct any of the light within the camera. Precise alignment of the high-speed camera and the light beam is required.

A.8 Conclusions (Caustics)

In this section we have presented the physical principles underlying the optical method of caustics. We also discuss several possible sources of inaccuracy that may arise in the classical interpretation of caustic patterns. The following basic conclusions are reached.

1. The existence of a near-tip three-dimensional zone excludes the possibility of interpreting caustic patterns that are obtained from distances smaller than one half of the specimen thickness from the crack-tip.

2. For distances from the crack-tip greater than half the specimen thickness, where plane stress conditions exist, the classical interpretation of caustic patterns is possible only if the surrounding field is strictly K_I^d dominant (well approximated by the $r^{1/2}$ singular term of the plane stress asymptotic expansion).
3. In most transient crack growth events K_I^d dominance is not generally observed, especially at times close to crack initiation or arrest. This is also true in laboratory size specimens where stress waves reflections may produce nonuniform stress-intensity factor histories. In such cases a truly transient higher-order expansion is necessary for correctly describing stress fields outside the crack-tip three-dimensional zone.
4. Under transient crack growth conditions, use of the classical analysis of caustics in the interpretation of the optical patterns may result in errors that could exceed 30% in the value of the dynamic stress intensity factor.
5. A modified analysis of caustics is presented. This analysis is based on a higher-order transient elastodynamic expansion at the vicinity of a growing crack. Preliminary investigations show that this analysis is capable of furnishing the correct value of $K_I^d(t)$ even at instances when highly transient effects dominate.
6. For stationary cracks in elastic-plastic solids we present an analysis of caustics based on the assumption of the existence of a well-established HRR field within the crack-tip plastic zone (assumption of J dominance).
7. We discuss the limitations of the J-dominant approach and present numerical results that allow for the interpretation of caustics for the case of *small-scale yielding* situations. The effects of three-dimensionality on the interpretation of caustic patterns is also discussed briefly.

B.1 Introduction [The Coherent Gradient Sensing (CGS)]

In this section we review recent experimental developments related to the investigation of crack-tip deformations in transparent and opaque solids using a new coherent optical technique—coherent gradient sensing (CGS). CGS is a full field, lateral shearing interferometric technique with an on-line spatial filter. This full field optical method will be demonstrated both in transmission and in reflection modes to study deformations in transparent as well as opaque solids. Its ability to produce fringes in real time is used advantageously to map dynamic crack-tip deformations in PMMA and AISI 4340 steel specimens. The technique measures either in-plane stress gradients (transmission) or out-of-plane displacement gradients (reflection).

Presently, several optical methods are being used for measuring surface slopes. Incoherent optical techniques such as reflection moiré [67] and moiré [68] deflectometry are commonly used. Among the coherent techniques, defocussed laser speckle photography [69], grating shearing interferometry

[70], and speckle shearing interferometry [71,72] are some of the examples. Many of these methods have been demonstrated with either reflective or diffused object surfaces. Also, they typically consist of double exposure procedure which is a severe limitation for dynamic applications.

In experimental fracture studies, photoelasticity [73,74], caustics, geometric moiré [75], and moiré interferometry [76] are some of the methods used to measure crack-tip deformations or deformation related quantities and hence the stress intensity factor. In these techniques, interpretation of the measurements is based on the premise that a K-dominant or a J-dominant 2D asymptotic field description exists in the vicinity of the crack-tip. However, in reality, the situation has not been this simple. Recent studies, discussed in part A of this chapter, have brought to light the shortcomings of such interpretations because of the three-dimensional nature of the crack-tip deformation and the inadequacy of the purely singular fields to model the region outside the three-dimensional zone (lack of K or J dominance).

From these experimental and numerical investigations, it has become inceasingly evident that a 2D K-dominant crack-tip field description for general specimen configurations should be used cautiously keeping in mind the near-tip three dimensionality and possible lack of K dominance. Furthermore, in dynamic loading situations, these complexities are compounded by the transient nature of the fracture phenomenon which may inhibit the establishment of a K_I^d-dominant region (see Sec. A.4 and A.5). In view of the above, besides demonstrating the applicability of CGS to static and dynamic fracture studies, we will also examine some aspects related to lack of K_I^d dominance. The work described in this part will closely parallel the discussions presented in Part A, on caustics.

In most methods applied to fracture mechanics, one often encounters the difficult question of whether the chosen experimental technique provides adequate control over the sensitivity of measurement. This becomes relevant because of the wide range of magnitudes of deformation that may occur near a crack-tip. Typically, interferometric methods are preferred for the measurement of elastic deformations while for larger deformations the resulting fringe density often overwhelms the recording capabilities. As a result, geometric moiré methods are used when large deformations exist. However, in fracture studies one often needs a method which can satisfactorily perform in both regimes.

In this section we introduce CGS as a potential tool for measuring in-plane gradients of out-of-plane surface displacements around a crack tip. The method produces high contrast fringes and provides a substantial degree of *control on the sensitivity* of measurement during quasi-static experiments. In addition, it involves a simple optical setup and, when compared to other interferometric techniques, it is relatively insensitive to vibrations. Finally, the insensitivity of this method to rigid body motions is highly attractive for solid mechanics applications.

CGS employs the basic principles of the so-called "moiré deflectometry" used widely in a variety of problems by Kafri and his associates [77,78]. However, CGS takes advantage of coherent optics by using wave-front division (by means of high-density Ronchi rulings) and their subsequent interference. By incorporating an online spatial filtering procedure, one could not only realize high contrast fringes in real time, but also use high-density diffraction gratings for the purpose.

Since CGS fringes are related to either in-plane stress gradients (transmission) or out-of-plane displacement gradients (reflection), the technique can be thought of as the *full field* equivalent of the optical method of caustics. (For both the transmission and reflection cases.) The sensitivity of the method to the same deformation or stress quantities responsible for the formation of caustics provides a unique opportunity of comparison. In particular, for transient dynamic fracture studies where the accurate interpretation of caustics has been questioned (see Sec. A.4), dynamic CGS has allowed for the direct investigation of the causes that lead to problems with caustics. In addition, the capability of CGS to investigate dynamic fracture problems in opaque materials (no severe light limitations resulting from exposure times of the order of ns) make this full field technique a strong contestor to caustics. Caustics by reflection have so far been the dominant optical method applied to the study of dynamic crack growth problems in opaque structural materials.

In Sec. B.2, we present a diffraction analysis of the method and experimental evidence to demonstrate its applicability for elastostatic and elastodynamic crack-tip deformation studies. Examples include the use of CGS for the measurement of dynamic mixed-mode crack-tip fields and the study of dynamic crack growth along bimaterial interfaces. For original references on CGS, see Tippur, Krishnaswamy, and Rosakis [79,80].)

B.2 Physical Principle of CGS

Consider a plate specimen of uniform thickness, in the undeformed state. Let its middle cross section occupy the x_1, x_2 plane of an orthonormal Cartesian coordinate system. The specimen is such that it causes nonuniform spatial gradients in the optical path when light is transmitted through it, or reflected from its surface. For solid mechanics applications these gradients are deformation related. For transmission of light through a transparent specimen the gradients in optical path are related to stress induced gradients in refractive index and due to local thickness changes of the specimen. For reflection they are related to gradients in nonuniform surface elevations (out-of-plane displacements) resulting due to mechanical loading. In solid mechanics, both gradients in refractive index and nonuniform thickness

changes are related to gradients in the stress state which are induced when loads are applied to the boundary of the initially undeformed specimen.

The purpose of the CGS technique is to provide a simple *full field* optical measurement of gradients in optical path change. Given appropriate stress-optical and constitutive relations this will allow for the measurement of in-plane stress gradients (transmission) and out-of-plane displacement gradients. The similarities of the analysis of CGS with the analysis of caustics in both the reflection and transmission cases are striking. As a result, many of the physical principles presented here in Secs. A.2–A.4 remain relevant for the following development.

B.2.1 The Experimental Arrangement

The schematic of the experimental setup used for transmission CGS is shown in Fig. 10.25(a). A transparent, optically isotropic plate specimen is illuminated by a collimated bundle of coherent laser light. The transmitted object wave is then incident on a pair of high density Ronchi gratings, G_1 and G_2, separated by a distance Δ. The field distribution on the G_2 plane is spatially filtered by the filtering lens L_1 and its frequency content is displayed on its back focal plane. By locating a filtering aperture around either the ± 1 diffraction orders, information regarding the stress gradients is obtained on the image plane of the lens L_2.

Figure 10.25(b) shows the modification of the above setup for measuring surface deflections of opaque solids when studied in reflection mode. In this case, the specularly reflecting object surface is illuminated by a collimated beam of laser light using a beam splitter. The reflected beam, as in the previous case, is processed through the optical arrangement which is identical to the one shown in Fig. 10.25(a).

In the following section, a first-order diffraction analysis is presented to demonstrate that the information displayed on the image plane indeed corresponds to gradients of in-plane stress and gradients of out-of-plane displacement.

Figure 10.26 explains the working principle of the method of CGS in two dimensions. For the sake of simplicity, and without losing generality, the line gratings are assumed to have a sinusoidal transmittance. Let the gratings G_1 and G_2 have their rulings parallel to, say, the x_1 axis. A plane wave transmitted through or reflected from an undeformed specimen and propagating along the optical axis, is diffracted into three plane wave fronts E_0, E_1, and E_{-1} by the first grating G_1. The magnitude of the angle between the propagation directions of E_0 and $E_{\pm 1}$ is given by the diffraction equation $\theta = \sin^{-1}(\lambda/p)$, where λ is the wavelength and p is the grating pitch. Upon incidence on the second grating G_2, the wave fronts are further diffracted into $E_{0,0}$, $E_{0,1}$, $E_{1,-1}$, $E_{1,0}$, $E_{1,1}$, etc. These wave fronts which are propagating in dis-

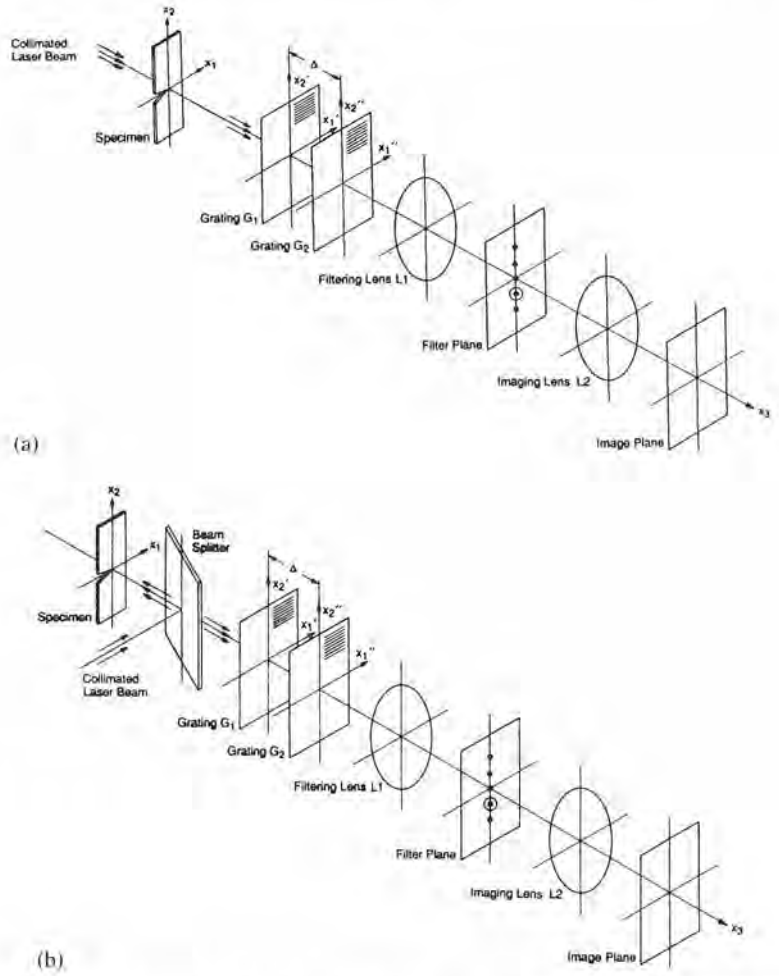

Figure 10.25. Schematic of the experiment setup for (a) transmission CGS, (b) reflection CGS.

tinctly different directions, are then brought to focus at spatially separated diffraction spots on the back focal plane of the filtering lens. The spacing between these diffraction spots is directly proportional to $\sin\theta$ or inversely proportional to the grating pitch p.

Now, consider a plane wave normally incident on a deformed specimen surface. The resulting transmitted or reflected wave front will be distorted either due to changes of refractive index or due to surface deformations. This object wave front that is incident on G_1 now carries information regarding the specimen deformation, and consists of light rays traveling with per-

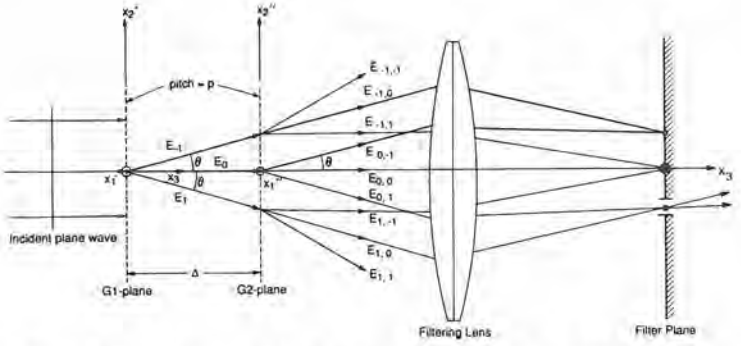

Figure 10.26. Schematic describing the working principle of CGS.

turbations to their initial direction parallel to the optical axis. If a large portion of such a bundle of light has rays nearly parallel to the optical axis, each of the diffraction spots on the focal plane of L_1 will be locally surrounded by a halo of dispersed light field due to the deflected rays. The extent of this depends on the nature of the deformations. By using a two-dimensional aperature at the filtering plane, information existing around one of the spots can be further imaged.

B.2.2 The Governing Equations of CGS

Consider a specimen whose midplane, in transmission, or surface, in reflection, occupies the (x_1, x_2) plane in the undeformed state. Let $\mathbf{e}_i$ denote unit vector along the x_i axis, $(i = 1, 2, 3)$ (see Fig. 10.27). When the specimen is undeformed, the unit object wave propagation vector (vector normal to the refracted or reflected wave front) is $\mathbf{d}_0 = \mathbf{e}_3$. After deformation, the propagation vector is perturbed and can be expressed by

$$\mathbf{d}_0 = \alpha\mathbf{e}_1 + \beta\mathbf{e}_2 + \gamma\mathbf{e}_3, \tag{54}$$

where $\alpha(x_1, x_2)$, $\beta(x_1, x_2)$, and $\gamma(x_1, x_2)$ denote the direction cosines of the perturbed wave front. This upon incidence on G_1, whose principal direction is parallel to, say, the x_2 axis, is split into three wave fronts propagating along $\mathbf{d}_0$, $\mathbf{d}_{\pm 1}$ and whose amplitudes $E_0(\mathbf{x}')$, $E_{\pm 1}(\mathbf{x}')$ can be represented by

$$E_0(\mathbf{x}') = a_0 \exp(ik\mathbf{d}_0 \cdot \mathbf{x}'), \tag{55}$$

$$E_{\pm 1}(\mathbf{x}') = a_{\pm 1} \exp(ik\mathbf{d}_{\pm 1} \cdot \mathbf{x}'),$$

where a_0 and $a_{\pm 1}$ are constants and $k = 2\pi/\lambda$ is the wave number. Due to diffraction by the sinusoidal grating G_1, the propagation directions of the diffracted wave fronts can be related by

$$\mathbf{d}_{\pm 1} = \Omega_{\pm 1}\mathbf{d}_0, \tag{56}$$

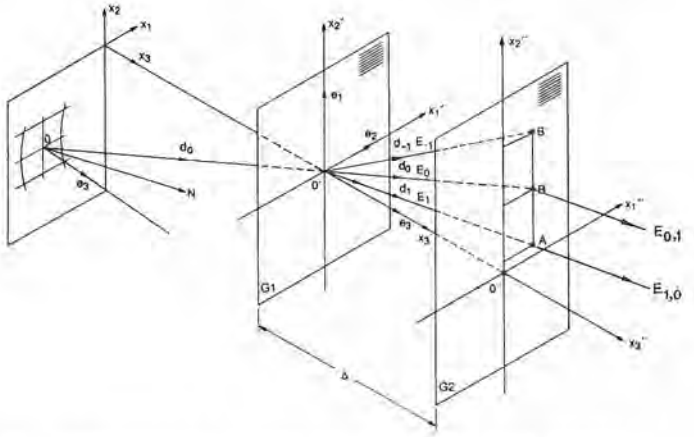

Figure 10.27. Diffraction of a generic ray through the CGS gratings.

where $\Omega_{\pm 1}$ are rotation tensors whose matrices of components are given by

$$[\Omega_{\pm 1}]_{ij} = \begin{pmatrix} 1 & 0 & 0 \\ 0 & \cos\theta & \pm\sin\theta \\ 0 & \mp\sin\theta & \cos\theta \end{pmatrix}$$

and $\theta = \sin^{-1}(\lambda/p)$. From Eqs. (56) and (54) we find

$$\mathbf{d}_{\pm 1} = [\alpha\mathbf{e}_1 + (\beta\cos\theta \pm \gamma\sin\theta)\mathbf{e}_2 + (\gamma\cos\theta \mp \beta\sin\theta)\mathbf{e}_3]. \tag{57}$$

On the plane G_2 ($x_3 = \Delta$) (see Fig. 10.27) the amplitude distribution of the three diffracted wave fronts are

$$E_0|_{x_3=\Delta} = E_0(\overrightarrow{O'B}) = a_0 \exp(ik\mathbf{d}_0 \cdot \overrightarrow{O'B}) \tag{58}$$

$$= a_0 \exp\left[ik\left(\frac{\Delta}{\mp\gamma}\right)\right],$$

$$E_1|_{x_3=\Delta} = E_1(\overrightarrow{O'A}) = a_1 \exp(ik\mathbf{d}_1 \cdot \overrightarrow{O'A}) \tag{59}$$

$$= a_1 \exp\left(ik\frac{\Delta}{(\gamma\cos\theta - \beta\sin\theta)}\right),$$

$$E_{-1}|_{x_3=\Delta} = E_{-1}(\overrightarrow{O'B'}) = a_{-1} \exp(ik\mathbf{d}_{-1} \cdot \overrightarrow{O'B'}) \tag{60}$$

$$= a_{-1} \exp\left(ik\frac{\Delta}{(\gamma\cos\theta + \beta\sin\theta)}\right).$$

The wave fronts E_0, $E_{\pm 1}$ will undergo further diffraction upon incidence on G_2 into secondary wave fronts $E_{(0,0)}$, $E_{(0,1)}$, $E_{(1,-1)}$, $E_{(1,0)}$, $E_{(1,1)}$, etc. Of these

secondary diffractions $E_{(0,1)}$ and $E_{(1,0)}$ have their propagation direction along $\mathbf{d}_1$, $E_{(0,-1)}$ and $E_{(-1,0)}$ along $\mathbf{d}_{-1}$ and $E_{(0,0)}$, $E_{(-1,1)}$, and $E_{(1,-1)}$, along $\mathbf{d}_0$ (Fig. 10.26). If information is spatially filtered by blocking all but ± 1 diffraction order, only the wave fronts $E_{(0,\pm 1)}$ and $E_{(\pm 1,0)}$ contribute to the formation of the image. Noting that the two wave fronts do not acquire any additional relative phase differences after G_2, the amplitude distribution on the image plane is

$$E_{\text{im}} = (E_0 + E_{\pm 1})|_{x_3=\Delta} \tag{61}$$

$$= a_0 \exp\left[ik\left(\frac{\Delta}{\gamma}\right)\right] + a_{\pm 1} \exp\left(ik \frac{\Delta}{(\gamma \cos\theta \mp \beta \sin\theta)}\right).$$

Hence, the intensity distribution on the image place is,

$$I_{\text{im}} = E_{\text{im}} E_{\text{im}}^{*} = a_0^2 + a_{\pm 1}^2 \tag{62}$$

$$+ 2a_0 a_{\pm 1} \cos\left[k\Delta\left(\frac{\gamma(\cos\theta - 1) \mp \beta \sin\theta}{\gamma(\gamma \cos\theta \mp \beta \sin\theta)}\right)\right],$$

where E_{im}^{*} is the complex conjugate of E_{im}. Under small θ approximation, the above equation simplifies to

$$I_{\text{im}} = a_0^2 + a_{\pm 1}^2 + 2a_0 a_{\pm 1} \cos\left(\frac{k\Delta\beta\theta}{\gamma^2}\right). \tag{63}$$

Thus, I_{im} denotes an intensity variation on the image plane whose maxima occur when

$$\frac{k\Delta\beta\theta}{\gamma^2} = 2n\pi \quad \text{or} \quad \frac{\beta}{\gamma^2} = \frac{np}{\Delta}, \qquad n = 0, \pm 1, \pm 2, \ldots, \tag{64}$$

where n denotes fringe orders. (Recall that $\theta \sim \lambda/p$, $k = 2\pi/\lambda$.) Similarly, when the principal direction of the grating is parallel to the x_1 axis, it can be shown that

$$\frac{k\Delta\alpha\theta}{\gamma^2} = 2m\pi \quad \text{or} \quad \frac{\alpha}{\gamma^2} = \frac{mp}{\Delta}, \qquad m = 0, \pm 1, \pm 2, \ldots. \tag{65}$$

Equations (64) and (65) are the governing equations for the method of CGS and they relate fringe orders to the direction cosines of the object wave front. It is clear from the above two equations that the sensitivity of the method could be *increased* by either increasing the grating separation distance Δ or decreasing the grating pitch p. As discussed extensively by Bruck and Rosakis, an increase of the ratio Δ/p eventually results in a violation of the small angle approximation implicit in the above analysis. Their work discusses the limitations and advantages of the above formulation and it presents an alternative analysis based on "physical" theories of optics. It is demonstrated that CGS strictly represent contours of *finite differences* in optical path.

These finite differences result by the "shearing" effect that the two gratings have on a diffracted wavefront which is split into two parts, displaced by an amount proportional to Δ/p relative to each other, and recombined. The relative displacement is in the direction perpendicular to the lines of the grating. The finite differences actually reduce to *derivatives* in optical path as Δ/p is decreased and the approximations of the above analysis become valid.

B.3 Relation Between Direction Cosines or Refracted or Reflected Wave Fronts and Deformation State

We now relate the direction cosines of the object wave front to deformation quantities of interest for both transmission and reflection cases. The discussion bares strong similarities to that in Sec. A.3 on caustics.

B.3.1 CGS by Transmission

Consider a planar wave front incident normal to an optically and mechanically isotropic, transparent plate of initial uniform nominal thickness h and reflective index n. If the plate is deformed, the transmitted wave front will be expressed as $S(x_1, x_2, x_3) = x_3 + \Delta s(x_1, x_2) = \text{const.}$, where Δs is the optical path change acquired during refraction.

As discussed in detail in Sec. A.3, in relation to caustics, for a homogeneous isotropic, linear elastic material, Δs will be given the elasto-optical equation

$$\Delta s = 2h\left(D_1 - \frac{\nu}{E}(n-1)\right)\int_0^{1/2}\left\{(\sigma_{11}+\sigma_{22})\times\left[1 + D_2\left(\frac{\sigma_{33}}{\nu(\sigma_{11}+\sigma_{22})}\right)\right]\right\} d\frac{x_3}{h}, \tag{66}$$

where

$$D_2 = \frac{\nu D_1 + \nu(n-1)/E}{D_1 - \nu(n-1)/E},$$

E and ν are Young's modulus and Poisson's ratio of the material, respectively, n is the refractive index of the undeformed material, and D_1 is the coefficient of the stress optical law. The above equation is written in such a way that the term in parentheses represents the degree of plane strain. [For a plot of $\sigma_{33}/\nu(\sigma_{11}+\sigma_{22})$ for a crack see Fig. 10.9.] When generalized plane stress is a good approximation, this term can be neglected and Eq. (66) reduces to

$$\Delta s \approx c_\sigma(\hat{\sigma}_{11} + \hat{\sigma}_{22}), \tag{67}$$

where $c_\sigma = D_1 - \dfrac{\nu}{E}(n-1)$ and $\hat{\sigma}_{11}$ and $\hat{\sigma}_{22}$ are thickness averages of stress components of the material. Using these, the propagation vector for a perturbed wave front can be expressed as

$$\mathbf{d}_0 = \frac{\nabla(S)}{|\nabla(S)|} = \frac{\dfrac{\partial(\Delta s)}{\partial x_1}\mathbf{e}_1 + \dfrac{\partial(\Delta s)}{\partial x_2}\mathbf{e}_2 + \mathbf{e}_3}{\sqrt{1 + \left(\dfrac{\partial(\Delta s)}{\partial x_2}\right)^2 + \left(\dfrac{\partial(\Delta s)}{\partial x_2}\right)^2}} \tag{68}$$

$$\approx \frac{\partial(\Delta s)}{\partial x_1}\mathbf{e}_1 + \frac{\partial(\Delta s)}{\partial x_2}\mathbf{e}_2 + \mathbf{e}_3 = \alpha\,\mathbf{e}_1 + \beta\,\mathbf{e}_2 + \gamma\,\mathbf{e}_3$$

for $|\nabla(\Delta s)|^2 << 1$ and where $S(x_1, x_2, x_3) = x_3 + \Delta s(x_1, x_2) = \text{const}$. Using Eq. (67) in Eq. (68), we can obtain the direction cosines of the propagation vector. Thus, using Eqs. (64) and (65) for plane stress conditions, the fringes can be related to the gradients of $(\hat{\sigma}_{11} + \hat{\sigma}_{22})$ as follows:

$$c_\sigma h \frac{\partial(\hat{\sigma}_{11} + \hat{\sigma}_{22})}{\partial x_1} \approx \frac{mp}{\Delta}, \qquad m = 0, \pm 1, \pm 2, \ldots, \tag{69}$$

$$c_\sigma h \frac{\partial(\hat{\sigma}_{11} + \hat{\sigma}_{22})}{\partial x_2} \approx \frac{np}{\Delta}, \qquad n = 0, \pm 1, \pm 2, \ldots, \tag{70}$$

B.3.2 CGS by Reflection

Consider a specimen whose specularely reflective and flat surface occupies the (x_1, x_2) plane in the undeformed state (Fig. 10.27). Upon deformation, the reflector can be expressed as

$$F(x_1, x_2, x_3) = x_3 + f_3(x_1, x_2) = x_3 + u_3(x_1, x_2) = 0, \tag{71}$$

where u_3 is the out-of-plane displacement component on the specimen surface. The unit surface normal $\mathbf{N}$ at a generic point (x_1, x_2) is given by

$$\mathbf{N} = \frac{\nabla F}{|\nabla F|} = \frac{u_{3,1}\,\mathbf{e}_1 + u_{3,2}\,\mathbf{e}_2 + \mathbf{e}_3}{\sqrt{1 + u_{3,1}^2 + u_{3,2}^2}}, \tag{72}$$

where $u_{3,\alpha}$ denotes in-plane gradient components. Consider now, a plane wave which is incident on the specimen along the $-x_3$ direction. Let $\mathbf{d}_0$ be the unit vector along the reflected ray whose direction cosines are α, β, and γ. From the law of reflection, the coplanar unit vectors $\mathbf{d}_0$, $\mathbf{N}$, and $\mathbf{e}_3$ are related by $\mathbf{d}_0 \cdot \mathbf{N} = \mathbf{e}_3 \cdot \mathbf{N}$ (see Fig. 10.27). This leads to

$$\mathbf{d}_0 = (2\mathbf{e}_3 \cdot \mathbf{N})\mathbf{N} - \mathbf{e}_3. \tag{73}$$

By substituting Eq. (72) in (73),

$$\mathbf{d}_0 = (\alpha \mathbf{e}_1 + \beta \mathbf{e}_2 + \gamma \mathbf{e}_3) \tag{74}$$

$$= \frac{2(u_{,1}\mathbf{e}_1 + u_{,2}\mathbf{e}_2 + \mathbf{e}_3)}{(1 + u_{,1}^2 + u_{,2}^2)} - \mathbf{e}_3.$$

Thus, the direction cosines of $\mathbf{d}_0$ can be related to the in-place surface gradients of u_3 by

$$\alpha = \frac{2u_{3,1}}{1 + u_{3,1}^2 + u_{3,2}^2}, \qquad \beta = \frac{2u_{3,2}}{1 + u_{3,1}^2 + u_{3,2}^2}, \tag{75}$$

$$\gamma = \frac{(1 - u_{3,1}^2 - u_{3,2}^2)}{(1 + u_{3,1}^2 + u_{3,2}^2)}.$$

Using the above equations (64) and (65), and assuming $|\nabla u_3|^2 << 1$, we get

$$\frac{\partial u_3}{\partial x_1} \approx \left(\frac{mp}{2\Delta}\right), \qquad m = 0, \pm 1, \pm 2, \ldots, \tag{76}$$

$$\frac{\partial u_3}{\partial x_2} \approx \left(\frac{np}{2\Delta}\right), \qquad n = 0, \pm 1, \pm 2, \ldots, \tag{77}$$

where the facts that $\theta \sim (\lambda/p)$ and $k = 2\pi/\lambda$ are made use of. For an isotropic, linear elastic solid the out-of-plane displacement field u_3 can be expressed as follows (see Sec. A.3):

$$u_3 = h \int_0^{1/2} \varepsilon_{33}(x_1, x_2, x_3) d(x_3/h) \tag{78}$$

$$= -\frac{\nu h}{E} \int_0^{1/2} \left[(\sigma_{11} + \sigma_{22}) \left(1 - \frac{\sigma_{33}}{\nu(\sigma_{11} + \sigma_{22})}\right)\right] d(x_3/h).$$

In the above, the second term in the large parentheses represents the degree of plane strain and when plane stress is a good approximation, it can be neglected. Thus, the above equation reduces to

$$u_3 = -\frac{\nu h}{2E}(\hat{\sigma}_{11} + \hat{\sigma}_{22}). \tag{79}$$

Hence Eqs. (76) and (77) for plane stress deformations can be expressed as

$$\frac{\partial u_3}{\partial x_1} = -\frac{\nu h}{2E} \frac{\partial(\hat{\sigma}_{11} + \hat{\sigma}_{22})}{\partial x_1} = \left(\frac{mp}{2\Delta}\right), \qquad m = 0, \pm 1, \pm 2, \ldots, \tag{80}$$

$$\frac{\partial u_3}{\partial x_2} = -\frac{\nu h}{2E} \frac{\partial(\hat{\sigma}_{11} + \hat{\sigma}_{22})}{\partial x_2} = \left(\frac{np}{2\Delta}\right), \qquad n = 0, \pm 1, \pm 2, \ldots, \tag{81}$$

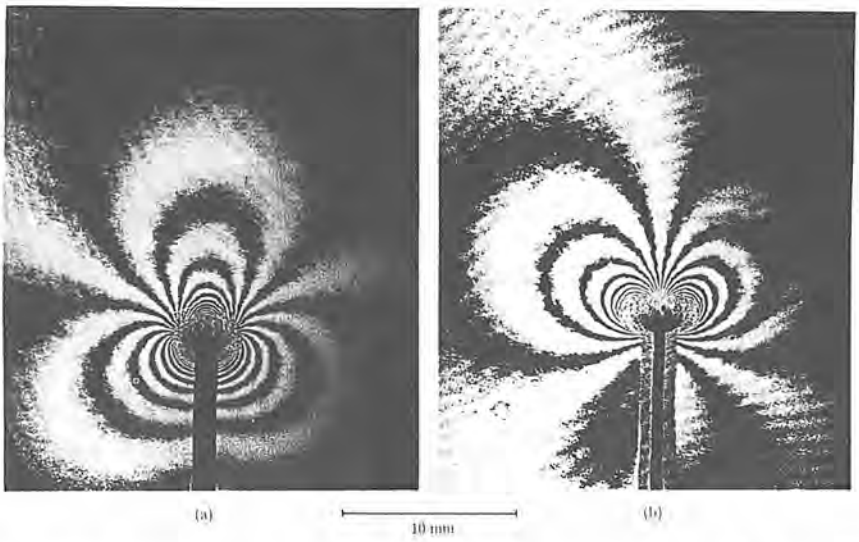

Figure 10.28. Fringe patterns representing contours of constant (a) $\frac{\partial u_3}{\partial x_1}$. (b) $\frac{\partial u_3}{\partial x_2}$. Material: Aluminum.

Figures 10.28(a) and 10.28(b) shows two CGS interferograms obtained by reflection of light from the near-tip region of an aluminum specimen containing a Mode-I crack. The specimen is loaded quasistatically. The contours in Fig. 10.28(a) are contours of equal $\partial u_3/\partial x_1$ [see Eq. (76)]. The coutours of Fig. 10.28(b) are contours of equal $\partial u_3/\partial x_2$ [see Eq. (77)]. In this particular case there is visual evidence of plastic deformation near the crack-tip (surface roughening near the crack-tip). As a result, the linearity assumption that led from Eqs. (76) and (77) to (80) and (81) is not necessarily valid everywhere and these displacement gradient contours cannot be related to the stress field unless an appropriate, elastic-plastic, constitutive law is utilized.

B.3.3 Three-Dimensional Effects

As is evident from the previous section, the expressions for the optical path change, Δs, [Eqs. (66) and (78)] involve the ratio $\sigma_{33}/\nu(\sigma_{11} + \sigma_{22})$. As discussed extensively in Sec. A.3, in relation to caustics, this ratio, called the plane strain constant, is a measure of three dimensionality. Figure 10.9 shows the plane strain constant in the vicinity of a dynamically loaded stationary crack in a linearly elastic homogeneous isotropic solid. As evident from this figure, the ratio $\sigma_{33}/\nu(\sigma_{11} + \sigma_{22})$ is small compared to unity only at distances from the crack-tip larger than half the specimen thickness, where

plane stress conditions seem to dominate. It is only in such regions that Eqs. (66) and (78) reduce to Eqs. (69) and (70) and Eqs. (80) and (81), respectively. This restriction should always be born in mind and is entirely analogous to the restriction on "initial curve" size which is required for a *plane stress* interpretation of caustic curves. (See Sec. A.3.)

In practical applications of the technique, only fringes outside the three-dimensional zone should be analyzed. Since this is a *variable sensitivity* method (for a fixed p, sensitivity is increased if the spacing between gratings, Δ, is increased), this can be achieved by choosing a ratio Δ/p such that enough experimental data are obtained outside the near-tip three-dimensional zone ($r \geq 0.5h$).

B.4 CGS Analysis Based on Plane Stress Asymptotic Crack-Tip Fields in Linear Elastostatics and Elastodynamics

B.4.1 Analysis of CGS Patterns on the Basis of K_I^d Dominance

Consider a Mode-I crack propagating dynamically in a thin plate composed of a homogeneous isotropic, linear elastic solid. The crack-tip velocity and the dynamic stress intensity factor are both allowed to be arbitrary functions of time. If a *generalized plane stress* assumption is made, then the thickness averages of the stresses at the vicinity of the propagating crack are asymptotically proportional to $r^{-1/2}$, where r is the distance from the propagating crack-tip. In particular, the thickness average of the first stress invarient $\hat{\sigma}_{11} + \hat{\sigma}_{22}$ which is of relevance in both CGS and caustics is asymptotically given by Eq. (22) in Sec. A.4. Stationary cracks in linear elastic solids are a special case corresponding to $v = 0$.

The situation in which the near-tip stresses are square-root singular and thus Eq. (22) provides an adequate representation of the first stress invarient at some annular region surrounding the crack-tip is called one of K_I^d *dominance*. The limitations of the assumption of K_I^d dominance are extensively discussed in Sec. A.4 of this chapter.

For the sake of analyzing CGS fringe patterns and in view of Eqs. (69), (70), (80), and (81) let us now define the quantities $Y_1^d(r_I, \theta_I, t)$ and $Y_2^d(r_I, \theta_I, t)$, related to the x_1 and x_2 partial derivatives of $\hat{\sigma}_{11} + \hat{\sigma}_{22}$ as follows:

$$Y_\alpha^d(r_I, \theta_I, t) = \frac{\partial(\hat{\sigma}_{11} + \hat{\sigma}_{22})}{\partial x_\alpha} \times \frac{2\sqrt{2\pi r_I^{3/2}}}{F(v)[\delta_{1\alpha} \cos(3\theta_I/2) + \delta_{2\alpha} \sin(3\theta_I/2)]}, \tag{82}$$

where $F(v), r_I, \theta_I$ are defined in Eq. (22) and $\delta_{\alpha\beta}$ is the Kronecker delta and α, β have the range $\{1,2\}$. $Y_\alpha^d(r_I, \theta_I)$ are constructed by normalizing the actual

x_1 and x_2 gradients of $\hat{\sigma}_{11} + \hat{\sigma}_{22}$, as measured by CGS, by the same gradients corresponding to the asymptotic field of Eq. (22) divided by the stress intensity factor. In time instants such that K_I^d dominance prevails [i.e., times such that there exist regions near the crack-tip where Eq. (22) describes the stress field], $Y_\alpha^d(r_l, \theta_l)$ are both equal to $K_I^d(t)$, for any choice of r_l and θ_l within the region of K_I^d dominance. At time instants during crack growth such that K_I^d dominance fails (K_I^d-dominant region vanishes), $Y_\alpha^d(r_l, \theta_l, t)$ are not in general constant but rather are expected to be functions of position.

For situations of K_I^d dominance, Eq. (82) can be used to estimate the stress intensity factor from CGS fringes by observing that use of Eqs. (69), (70), (80), and (81) results in the following relations for $K_I^d(t)$:

$$K_I^d(t) = Y_\alpha^d(r_l, \theta_l, t),$$

where

$$Y_\alpha^d(r_l, \theta_l, t) = \frac{k_\alpha p}{\Delta} \frac{2\sqrt{2\pi} r_l^{3/2}}{chF(\nu)[\delta_{1\alpha} \cos(3\theta_l/2) + \delta_{2\alpha} \sin(3\theta_l/2)]}, \tag{83}$$

$$k_\alpha = \begin{cases} m \text{ for } \alpha = 1, \; m = 0, \pm 1, \pm 2, \ldots \\ n \text{ for } \alpha = 2, \; n = 0, \pm 1, \pm 2, \ldots \end{cases}$$

and

$$c = \begin{cases} D_1 - \nu/E(n-1) = c_{tr} & \text{for transmission} \\ -\nu/E & \text{for reflection} \end{cases}.$$

The right-hand side of Eq. (83) can be experimentally measured from a CGS interferogram. Δ and p, c, and h are constants related to the experimental setup material and specimen. Also, if $\nu(t)$ is known, r_l, θ_l can be computed from the position (r, θ) of *any point within the K_I^d-dominant region* while m or n are fringe orders.

Figures 10.29(a) and 10.29(b), shows two CGS interferograms obtained by transmission of light from the near-tip region in a PMMA three-point-bend specimen containing a crack (for details, see Tippur, Krishnaswamy, and Rosakis [80]). The specimen is loaded symmetrically and the load is applied quasistatically. The contours in Fig. 10.29(a) are proportional to $\partial(\hat{\sigma}_{11} + \hat{\sigma}_{22})/\partial x_1$ where x_1 is along the crack line. The contours in Fig. 10.29(b) are proportional to $\partial(\hat{\sigma}_{11} + \hat{\sigma}_{22})/\partial x_2$. In both figures, the superposed line denotes the theoretical CGS fringes expected if K_I^d dominance, for $\nu = 0$, holds. Indeed, for this case the agreement is good suggesting validity of this assumption. In the next section, we will discuss a systematic way of examining K_I^d dominance under both quasistatic and dynamic conditions. For the case of lack of K_I^d dominance, we will suggest ways of measuring $K_I^d(t)$ through an analysis based on a transient high-order expansion.

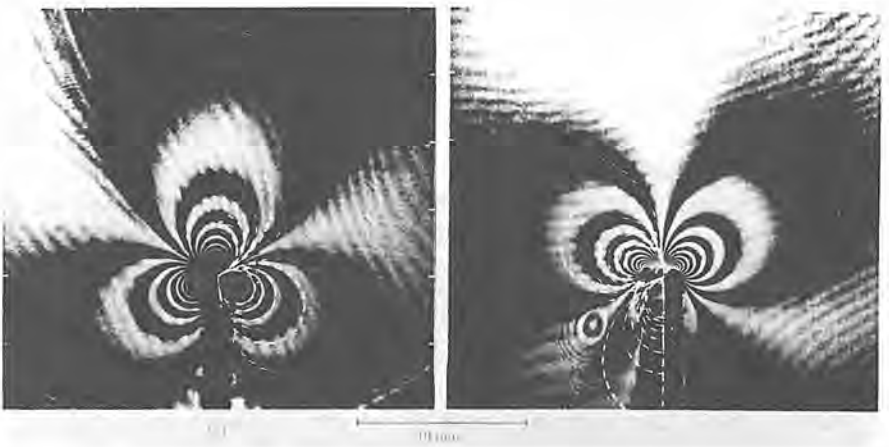

Figure 10.29. Near-tip fringe patterns representing contours of constant (a) $\partial(\hat{\sigma}_{11} + \hat{\sigma}_{22})/\partial x_1$, (b) $\partial(\hat{\sigma}_{11} + \hat{\sigma}_{22})/\partial x_2$.

B.4.2 Experimental Investigation of K_I^d-Dominance

The question of K_I^d dominance has been investigated in detail by Tippur, Krishnaswamy, and Rosakis [80], Krishnaswamy, Tippur, and Rosakis [48], and by Freund and Rosakis [46] for both the quasistatic and dynamic cases by using the method of CGS. Here we present a summary of their results and we choose to emphasize points related to our discussion of Secs. A.4 and A.5 pertaining to the interpretability of optical caustics generated during transient crack growth. Our goal is not only to observe situations of lack of K_I^d dominance but to also examine the nature of the near-tip field when this assumption fails. Our specific aim is to verify the hypothesis made in Sec. A.5, regarding the validity of a higher-order transient elastodynamic expansion for the near-tip deformation field. We begin our experimental investigation of this phenomenon by considering a set of experiments performed on precracked PMMA and 4340 steel specimens in both transmission and reflection modes.

The specimen geometry was of the three-point-bend type. The nominal specimen dimensions were length $2l = 30.4$ cm, width $w = 12.7$ cm and thickness $h = 1$ cm. A band saw, approximately 0.75 mm thick, was used to cut an initial notch of length $a = 25$ mm in these specimens. In the transmission mode, no further specimen preparation was needed. In the reflection mode, an aluminum coating was applied to the PMMA specimen surface through a vacuum deposition technique in order to make it reflective. The 4340 carbon steel specimens were lapped so that their surfaces became optically flat. Then they were polished by diamond paste to a mirror finish. An aluminum coating was also applied to increase the reflectivity.

The specimens were loaded in a three-point-bending configuration. The loading device used to dynamically load the specimens was the Dynatup 8100A drop-weight tower. The experimental configuration is such that the crack is under Mode-I loading conditions.

A rotating-mirror type high-speed camera set-up was used to obtain a sequence of dynamic CGS interferograms. A Spectra Physics (model 166) argon-ion pulse laser (output power 2 W at $\lambda = 514$ nm in continuous wave mode) was used as the light source. The laser beam was expanded and collimated to obtain a beam 50 mm in diameter which was centered on the initial notch tip of the specimen. The transmitted or reflected object wave front was then processed through a pair of line gratings of density 40 lines/mm with a separation distance $\Delta = 30$ mm. The gratings were oriented with their principal direction parallel to the crack line in order to obtain the x_1-gradient information of the crack-tip fields. The resulting diffraction wave fronts were then collected, filtered, and imaged onto a rotating-mirror high-speed camera through a series of lenses. The pulsing circuit of the laser was set to give 50 ns exposure every 7–10 μs for a total of 1 ms from the time of an input trigger which wsa synchronized to the moment of impact of the drop-weight with the specimen.

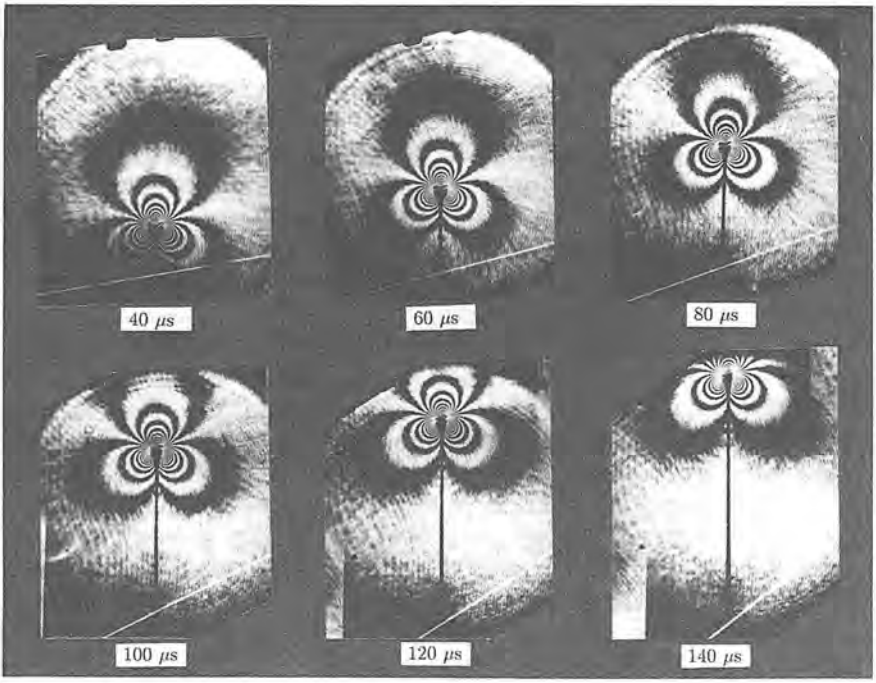

Figure 10.30. Sequence of transmission CGS x_1 gradient fringe patterns for a dynamically propagating crack in PMMA specimen.

Figure 10.30 shows a representative sequence of CGS (transmission mode) interferograms for the case of a dynamically propagating crack in a PMMA specimen. Figure 10.31 shows the CGS pattern corresponding to a time of 20 μs after initiation.

It was found that the crack propagated with an essentially *constant velocity* of about 0.3 the shear wave speed of the material. These fringe patterns correspond to the case when the diffraction gratings were oriented with

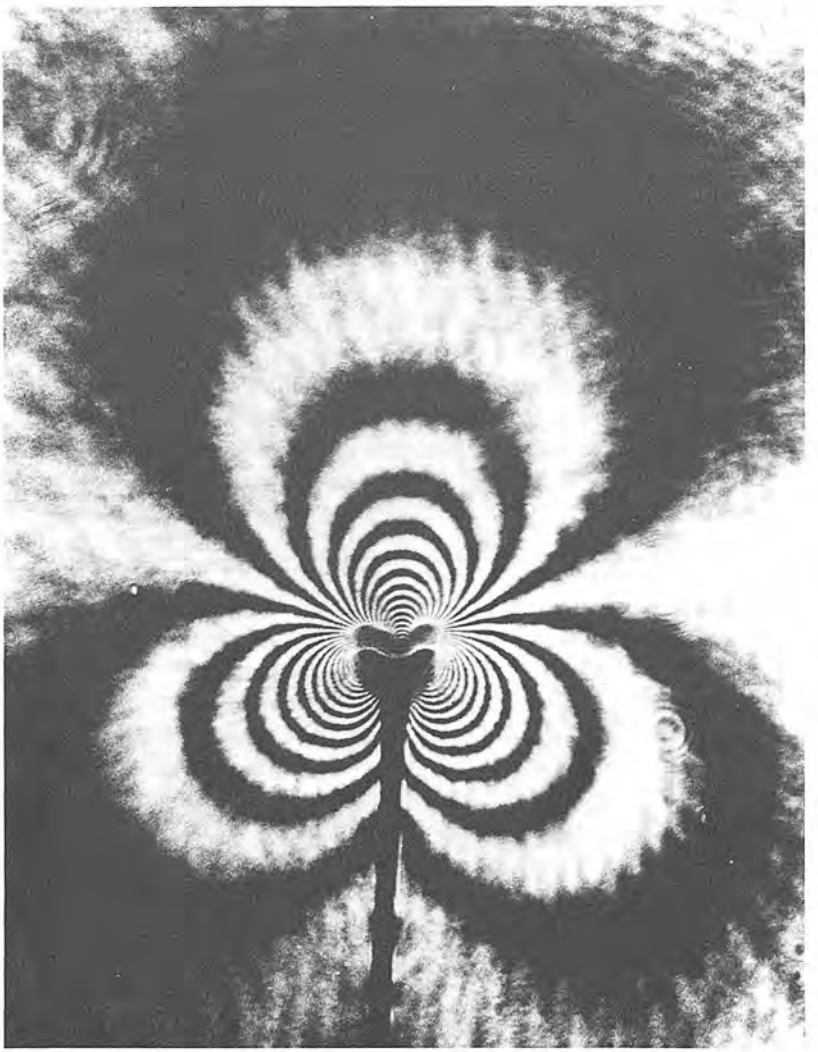

Figure 10.31. Transmission CGS x_1-gradient pattern (enlarged) corresponding to 20 μs after crack initiation in PMMA specimen.

their principal directions parallel to the x_1 axis. Thus, the fringes surrounding the crack-tip at each instant of time represent the x_1 gradient of $(\hat{\sigma}_{11} + \hat{\sigma}_{22})$.

The fringe patterns were digitized for analysis to get fringe order *(m)* and location (r_i,θ_i) with respect to the crack-tip at each instant in time. The quantity $Y_1^d(r_i,\theta_i,t)$, defined in Eq. (82), can now be plotted from the experimental data obtained from each CGS interferogram. If the field is K_I^d dominant $Y_I^d(r_i,\theta_i,t)$ should be a constant $\forall(r,\theta)$ and equal to K_I^d.

Figure 10.32 shows a typical plot of Y_I^d against normalized radial distance *(r/h)* for one particular specimen for a time instant a few microseconds after crack initiation. For different radial lines $\theta_i = 0°$, 15°, 30°, 45°, 105°, 120°, and 135° around the propagating crack-tip.

The crack-tip velocity at that time is approximately 300 *m/s*. As is apparent from the figure, there appears to be *no* region around the crack-tip over which the function Y_1^d is constant. Indeed the spread in Y_1^d values from different locations is as much as 400%. Obviously, extraction of the dynamic stress intensity factor value cannot be based here on a simplistic assumption of near-tip K_I^d dominance, see Eq. (83) for $K_I^d(t)$. One other interesting point must be made. The instantaneous crack length a to plate width w ratio at the time shown in Fig. 10.32 was $a/w = 0.2$. The immediate question that arises is: would there be a region of *static* K_I dominance around a stationary crack of the same length in a *statically* loaded specimen of the *same* geometry? The answer is provided in Fig. 10.33, which shows a plot of the static counterparts of the quantities plotted in Fig. 10.32 for the case of a specimen with $a/w = 0.2$ in an identical specimen to the one tested dynamically.

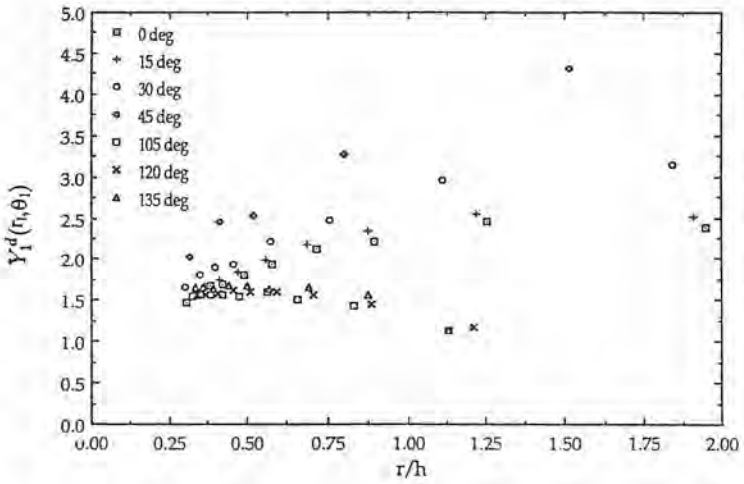

Figure 10.32. Radial variation of $Y_1^d(r_i, \theta_i)$ along various θ_i for a dynamically propagating crack in PMMA specimen corresponding to 20 μs from crack initiation when crack length to plate width ration is $a/w = 0.2$.

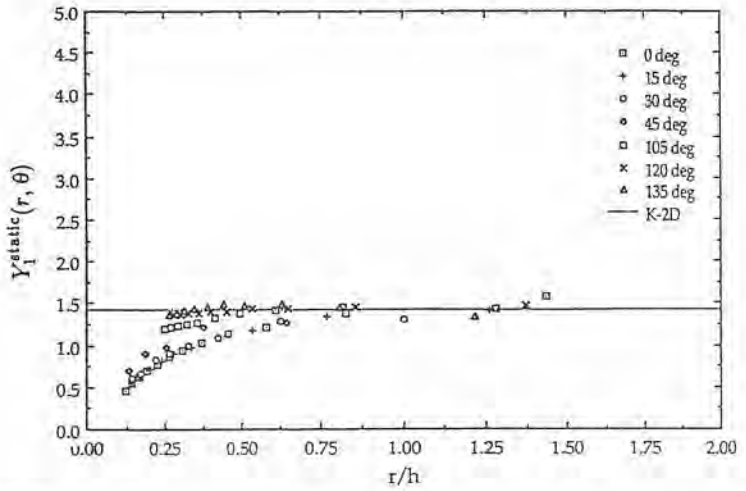

Figure 10.33. Radial variation of $Y_1^{static}(r, \theta)$ along various θ for a statically loaded crack in PMMA specimen with crack-length–to–plate-width ratio $a/w = 0.2$.

In the region $(r/h) < 0.5$, Y_1^{static} does not seem to be constant and thus the field in this region does not appear to be K_I dominant. This is consistent with other experimental investigations using caustics wherein such deviation has been attributed to near-tip three dimensionality (see Sec. A.3, Figs. 10.9 and 10.10). Outside this three-dimensional region, however, there appears to be a sizeable region of constant Y_1^{static} in the range $0.5 \leq (r/h) \leq 1.25$. Further, the constant value of Y_1^{static} in this range is in good agreement with the static stress intensity factor K_I^{2D} as obtained from boundary load measurements. This is a clear indication that even though a stationary crack might exhibit a sizeable region of K_I dominance under static loading conditions, there might be no corresponding region of K_I^d dominance when a crack of the same instantaneous length is propagating dynamically in an identical specimen subjected to dynamic loading.

It should be noted at this point that the reflection experiments performed in PMMA and 4340 steel, reported by Krishnaswamy, Tippur, and Rosakis [48] corroborate the above conclusions. The results are entirely analogous.

The observed lack of dynamic K_I^d dominance outside the near-tip three-dimensional region using CGS is consistent with the observations of lack of K_I^d dominance reported in Sec. A.5 observed by means of bifocal caustics [36,37] (see Fig. 10.15).

In the next section we provide an explanation of $Y_I^d(r_i, \theta_i)$ values presented in Fig. 10.32. Our goal is to demonstrate that the observed spread in Y_I^d values is governed by the specific structure of the transient stress field near the crack-tip and is not due to random experimental error. Consistent with

our discussion of Sec. A.6 on caustics, we investigate the interpretation of dynamic CGS fringes on the basis of a transient higher-order expansion.

B.5 Interpretation of CGS on the Basis of a Higher-Order Transient Elastodynamic Analysis

While dynamic caustic patterns have traditionally been analyzed under the often unverified assumption of K_I^d dominance (see discussion in Secs. A.4 and A.5) the use of higher-order terms has been the recent practice in the method of dynamic photoelasticity (for details see contribution to this volume by Chona). However, all available higher-order elastodynamic solutions thus far have been for the case of steadily propagating cracks and the applicability of such solutions to *highly transient* problems may be questioned. Indeed, the main criticism of this approach has been that such a procedure may result in inappropriate time averaging of field quantities. Nonetheless, use of a higher-order steady-state expansion in the analysis of optical data is bound to be an improvement over the assumption of strict K_I^ddominance.

In the following, we will relax the assumptions of near-tip K_I^d dominance and steady-state crack propagation. We will show that if these assumptions fail, that the experimentally obtained transmission and reflection mode CGS interferograms can be successfully interpreted on the basis of a transient, higher-order stress field for a propagating crack that has become available recently (Freund and Rosakis [46], Rosakis, Liu, and Freund [47].) This procedure allows for the accurate measurement of $K_I^d(t)$ even in the presence of highly transient crack growth events.

B.5.1 Transient Higher-Order Fields

Freund and Rosakis have extended the earlier interior asymptotic solution of Freund and Clifton to provide a higher-order description of the transient stress state at the vicinity of a dynamically propagating crack. The most general form of this expansion corresponding to nonuniform crack velocities and stress intensity factor histories was briefly discussed here in Sec. A.5. For the purpose of the constant velocity CGS experiments discussed in this section, we present a specialization of their results for the case of constant crack-tip speeds.

Although crack-tip velocity is kept constant, the following expression is still a transient result since the coefficients of the six terms presented are arbitrary functions of time. Moreover, the coefficients of the higher-order terms of this expansion involve first and second time derivatives of coefficients of lower order terms. The steady-state higher-order expansion utilized by Dally, Fourney, and Irwin [52] is contained in this result as a special case.

According to Freund and Rosakis [46], the thickness averages of the first stress invarient under plane stress conditions is given up to six terms, by

$$\begin{aligned}
\frac{\hat{\sigma}_{11} + \hat{\sigma}_{22}}{2\rho(c_l^2 - c_s^2)} &= \frac{3v^2}{4c_l^2} A_0 \cos\left(\frac{\theta_l}{2}\right) r_l^{-1/2} + \frac{2v^2}{c_l^2} A_1 \\
&+ \left\{\left[\frac{15v^2}{4c_l^2} A_2 + \left(1 - \frac{v^2}{2c_l^2}\right) D^1(A_0)\right] \cos\left(\frac{\theta_l}{2}\right)\right. \\
&\left. + \frac{v^2}{8c_l^2} D^1(A_0) \cos\frac{3\theta_l}{2}\right\} r_l^{1/2} \\
&+ \left\{\left[\frac{6v^2}{c_l^2} A_3 + \left(1 - \frac{v^2}{4c_l^2}\right) D^1(A_1)\right] \cos(\theta_l)\right\} r_l \\
&+ \left\{\left[\frac{35v^2}{4c_l^2} A_4 + \left(1 - \frac{v^2}{2c_l^2}\right) D^1(A_2) + \frac{1}{9}\left(1 - \frac{v^2}{4c_l^2}\right) D^2(A_0)\right.\right. \\
&\left.\left. + \left(1 - \frac{v^2}{2c_l^2}\right) \ddot{A}_0\right] \cos\left(\frac{3\theta_l}{2}\right)\right\} \\
&+ \left[\frac{3v^2}{8c_l^2} D^1(A_2) + \frac{1}{6}\left(1 - \frac{v^2}{4c_l^2}\right) D^2(A_0) + \frac{3v^2}{8c_l^2} \ddot{A}_0\right] \cos\left(\frac{\theta_l}{2}\right) \\
&+ \left(\frac{v^2}{96c_l^2} D^2(A_0)\right) \cos\left(\frac{5\theta_l}{2}\right) r_l^{3/2} \\
&+ \left\{\left[\frac{12v^2}{c_l^2} A_5 + \left(1 - \frac{v^2}{2c_l^2}\right) D^1(A_3) + \frac{D^2(A_1)}{16}\right.\right. \\
&\left.\left. + \left(1 - \frac{v^2}{2c_l^2}\right) \ddot{A}_1\right] \cos(2\theta_l)\right\} \\
&+ \left[\frac{v^2}{2c_l^2} D^1(A_3) + \frac{1}{8}\left(1 - \frac{v^2}{4c_l^2}\right) D^2(A_1) + \frac{v^2}{2c_l^2} \ddot{A}_1\right] r_l^2 + o(r_l^2),
\end{aligned} \tag{84}$$

where

$$D^1(A_k) = -\frac{(k+3)v}{c_l^2 \alpha_l^2} \frac{d}{dt}(A_k), \qquad k = 0,1,2,\ldots,$$

$$D^2(A_k) = D^1[D^1(A_k)],$$

$$\ddot{A}_k = \frac{1}{c_l^2 \alpha_l^2}\left(\frac{d^2}{dt^2} A_k\right),$$

and ρ is the mass density of the material. Although the above expression is for the special case of constant crack velocity, the coefficients A_k in the above transient field are allowed to be time varying as opposed to the steady-state approximation where the corresponding coefficients must be constant. Note also that the *spatial variation* of the terms associated with coefficients A_k are only identical to the ones that would be obtained from a higher-order steady-state analysis with $A_0(t)$ being proportional to the dynamic stress intensity factor and so on. Furthermore, it is seen that the higher-order transient expression contains *additional* terms whose coefficients depend on *time derivatives* of lower-order coefficients. As a result, the net spatial variation shown in the above expression (even for $v \to 0$) is *different* than the steady-state higher-order expansion used by Dally, Fourney, and Irwin. An illustration of the interdependence of the coefficients of higher- and lower-order terms is provided if one observes that D^1 (A_0) is proportional to the first time derivative of the stress intensity factor history, since

$$A_0(t) = \frac{4}{3}\frac{K_I^d(t)}{\pi\sqrt{2\pi}}\frac{(1+\alpha_s^2)}{[4\alpha_s\alpha_l-(1+\alpha_s^2)^2]}.$$

Transmission Mode. Substituting the transient field given in Eq. (84) in to the x_1-gradient transmission mode fringe Eq. (69), and using Eq. (82), we get an expression for $Y_1^d(r_l,\theta_l,t)$ of the form

$$Y_1^d(r_l,\theta_l,t) = \left(\frac{mp}{\Delta}\right)\frac{1}{F(v)}\frac{2\sqrt{2\pi}}{c_v h}\frac{r_l^{3/2}}{\cos(3\theta_l/2)} \tag{85}$$

$$= K_I^d + \left(\beta_2\frac{\cos(\theta_l/2)}{\cos(3\theta_l/2)} + \beta_3\frac{\cos(5\theta_l/2)}{\cos(3\theta_l/2)}\right)r_l$$

$$+ \left(\beta_4\frac{1}{\cos(3\theta_l/2)}\right)r_l^{3/2}$$

$$+ \left(\beta_4\frac{\cos(\theta_l/2)}{\cos(3\theta_l/2)} + \beta_6 + \beta_7\frac{\cos(7\theta_l/2)}{\cos(3\theta_l/2)}\right)r_l^2$$

$$+ \left(\beta_8\frac{\cos(\theta_l)}{\cos(3\theta_l/2)}\right)r_l^{5/2} + o(r^3),$$

where K_I^d, the dynamic stress intensity factor, as well as $\beta_2 \ldots \beta_8$ are time-dependent coefficients to be determined. Under K_I^d dominance, Y_1^d would have been a constant for every (r_l,θ_l), and would be equal to the instantaneous stress intensity factor K_I^d. If significant higher-order transient terms exist, then the variation of Y_1^d would be given by the right-hand side of Eq. (85), which for simplicity will be denoted by $G_1^d(r_l,\theta_l;\ K_I^d, \beta_2, \ldots, \beta_8)$.

A least-squares procedure analogous to the one described by Tippur, Krishnaswamy, and Rosakis was used to fit the above function G_1^d to the

experimental data Y_I^d obtained from the CGS interferograms. Since Eq. (85) is obtained from a two-dimensional analysis, data from the near-tip three-dimensional region were excluded. The three-dimensional region excluded was based on a cut off value for the degree of plane strain (which, strictly, should be zero in regions of plane stress) as shown in Fig. 10.9.

Figure 10.34 shows the results for one particular time instant during crack propagation in the specimen. The agreement between the fitted function G_I^d [based on the transient expansion (84) to $O(r^2)$] and the experimental data in Fig. 10.34 is indeed seen to be remarkably good.

Figure 10.35 conveys a more visual picture of the agreement between the transient analysis and the data. Here, a reconstructed fringe pattern from the fitted function G_I^d is shown superposed (as broken lines) on one side of the corresponding CGS interferogram. Also shown on the other side as solid lines is the reconstructed fringe pattern obtained from a least-squares analysis based on the assumption of K_I^d dominance [equivalent to using only one term in Eq. (84)].

The crosses on the left-hand side represent the experimental data obtained from the CGS interferogram. It is seen that the transient analysis agrees very well with the experimental data in the range ($0.5 < r/h < 2.0$, $-\pi < \theta < \pi$), whereas the K_I^d-dominance assumption is clearly inadequate. This was the case for most interferograms obtained at times close to crack initiation. This strongly suggests that *the observed lack of K_I^d dominance in the two-dimensional region outside the near-tip three-dimensional zone is due to the important contribution of higher-order terms to the total stress and deformation fields around the crack-tip. The importance of these terms*

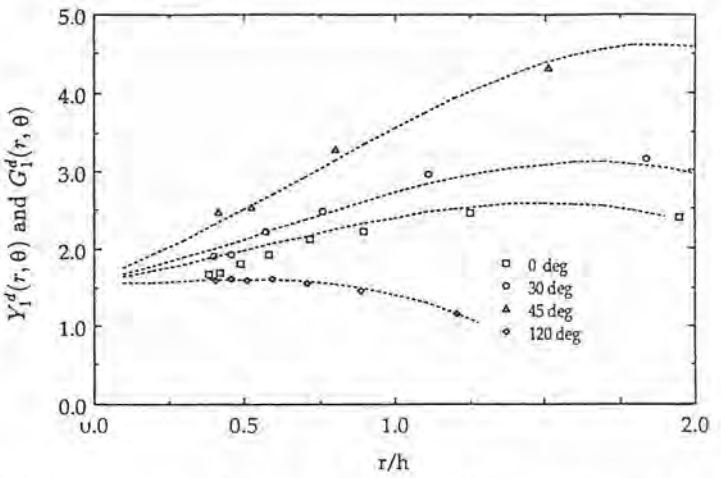

Figure 10.34. Comparison of the radial variation of the experimental data $Y_I^d(r, \theta)$ and the analytical fit $G_I^d(r, \theta)$ for various θ for transmission mode CGS patterns for specimen.

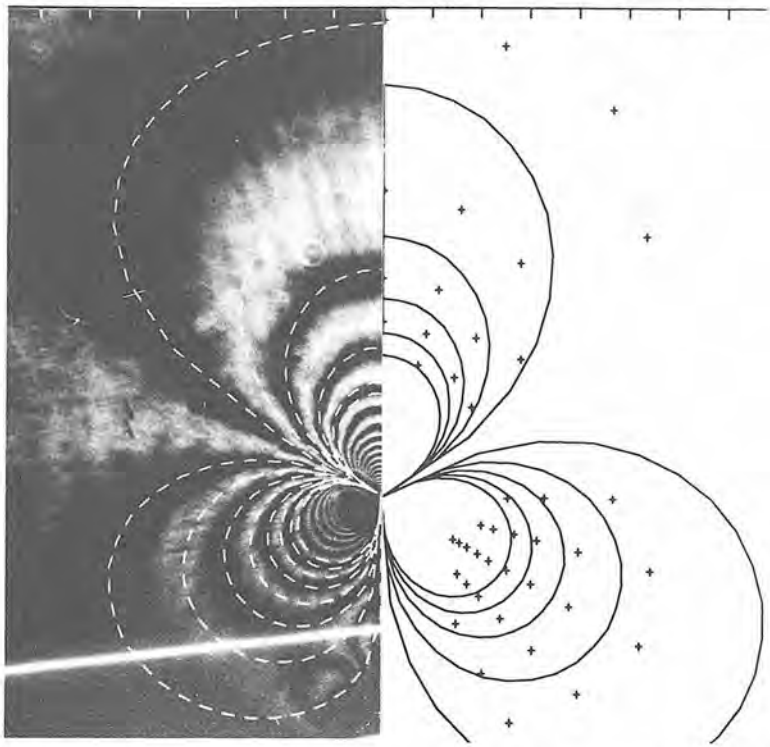

Figure 10.35. Synthetic fringe patterns reconstructed from one- and six-term transient analyses compared with the corresponding transmission mode x_1 gradient CGS interferogram.

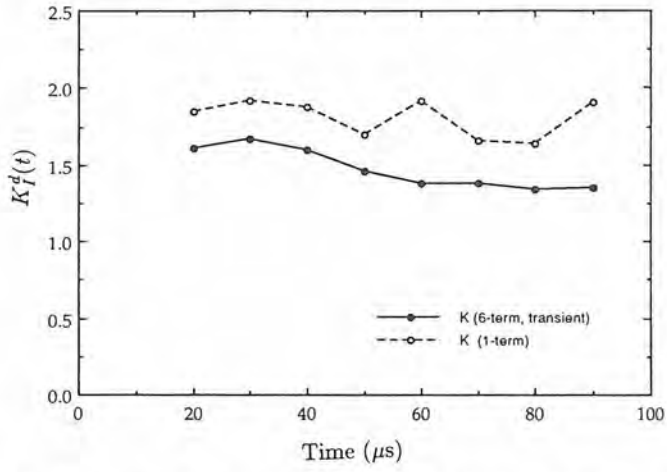

Figure 10.36. Time variation of the dynamic stress intensity factor as obtained from one- and six-term transient analyses of a CGS time sequence.

relative to the first term of the expansion is found to be intimately related to the transient nature of the crack growth event.

The errors associated with interpretation of experimental data on the basis of K_I^d dominance can now be evaluated. Figure 10.36 shows the time variation of the dynamic stress intensity factor during crack propagation in specimen as obtained form the time sequence of x_1-gradient CGS fringe patterns. The solid line represents the value for the dynamic stress-intensity factor when the fringes were interpreted on the basis of the higher-order transient analysis. The dotted line corresponds to the value for the dynamic stress intensity factor obtained when the fringes were analyzed under the assumption of K_I^d dominance (most singular contribution only). It is clear that interpretation of experimental data on the basis of K_I^d dominance leads to substantial errors in the measured values for the dynamic stress intensity factor.

Reflection Mode. A higher-order analysis of reflection mode CGS interferograms can be performed along essentially the same lines as described above. Substituting the higher-order expression for the stresses [Eq. (84)] in the reflection mode fringe relation (76), leads after rearrangement to

$$Y_1^d(r_l,\theta_l,t) = \left(\frac{mp}{2\Delta}\right)\frac{1}{F(\nu)}\frac{E\sqrt{2\pi}}{\nu h}\frac{r_l^{3/2}}{\cos(3\theta/2)} \tag{86}$$

$$= G_1^d(r_l,\ \theta_l;\ K_I^d,\ \beta_2\ \ldots\ \beta_8).$$

Here G_1^d is the same expression as the right-hand side of Eq. (85) and the left-hand side of the above expression is the quantity Y_I^d previously defined in Eq. (82). Once again, the experimental data Y_I^d can be fitted to the function G_I^d through the least-squares procedure discussed earlier.

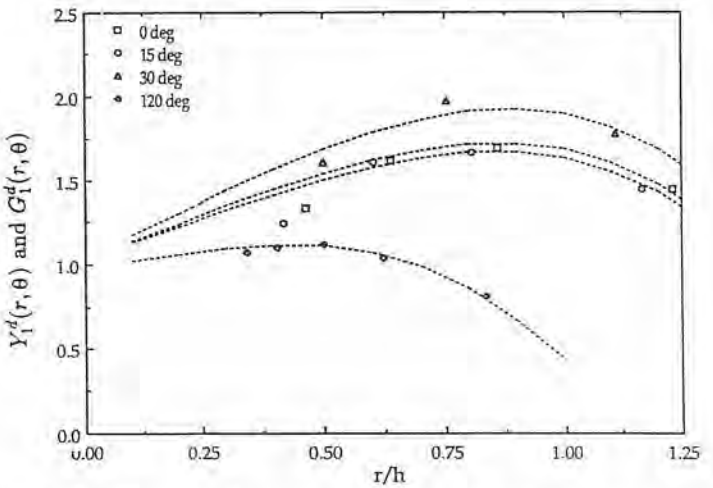

Figure 10.37. Comparison of the radial variation of the experimental data $Y_1^d(r,\theta)$ and the analytical fit G_1^d,r,θ for various θ for reflection CGS patterns.

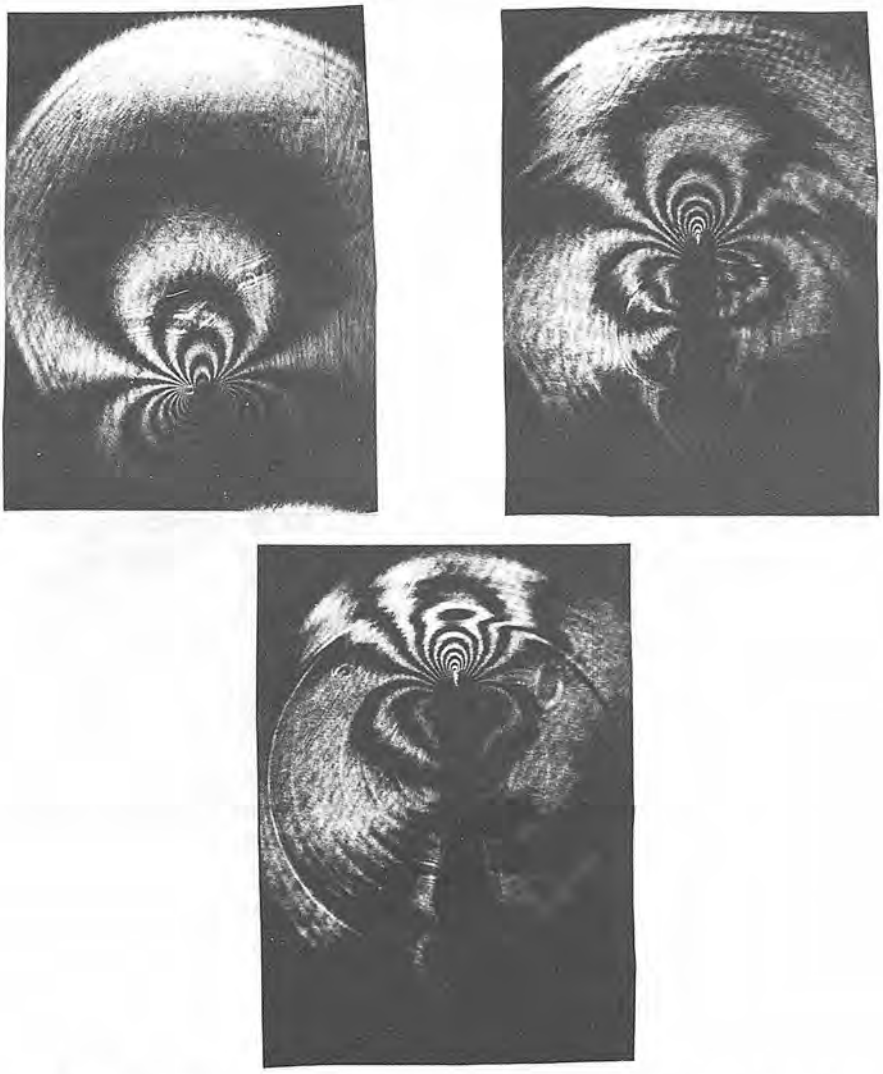

Figure 10.38. Reflection mode x_1-gradient CGS fringe patterns for an initiating and rapidly propagating crack in an AISI 4340 steel specimen showing strong influence of stress waves.

Figure 10.37 shows the *reflection mode* CGS results for one particular time instant during crack propagation in a PMMA specimen whose surfaces have been aluminized through vacuum deposition. As in the transmission mode case, the agreement between the fitted function G_1^d and the data Y_1^d is good outside the near-tip three-dimensional region. Again, it is seen that K_I^d-dominance assumption is clearly inadequate. We thus note that a *consis-*

tent interpretation of both transmission and reflection mode CGS fringe patterns is possible through inclusion of transient higher-order effects.

Figure 10.38 shows a representative sequence of CGS interferograms obtained by reflection of light from the surface of an AISI 4340 carbon steel specimen containing a dynamically growing crack. Strong transient effects are present. Visual evidence of the transient nature of this process are presented in the form of unloading waves (circular lines surrounding the tip) that disturb the optical pattern at times after the crack starts propagating. (Average crack growth velocity, $v \sim 1500$ *m/s*.)

To further illustrate the *transient* nature of the crack-tip fields, the time histories of the stress intensity factor $K_I^q(\mathbf{t})$ and of the coefficients $\beta_k(t)$ inferred from the data during a representative dynamic fracture experiment are shown in Fig. 10.39. Each of the quantities is normalized by its mean value for the entire test. Even though the crack speed was constant during the entire observation, the figure clearly shows the transient nature of the crack growth process. For at least the first 50 μs after initiation of crack growth from a stationary blunted notch, there is significant fluctuation in the values of $\beta_k(t)$, $k = 2, \ldots, 7$. The figure clearly shows the inadequacy of a *steady-state* higher-order expansion at times less than approximately 50 μs after initiation.

As evident form the above results, the assumption of K_I^q dominance fails in the plane stress region surrounding the near-tip three-dimensional zone. It is therefore expected that caustic patterns obtained from such regions and analyzed by using the classical analysis of caustics (see Sec. A.4) would not yield the correct value of stress intensity factor. This is true because in such cases the crack-tip fields are not well approximated by the single term Eq.

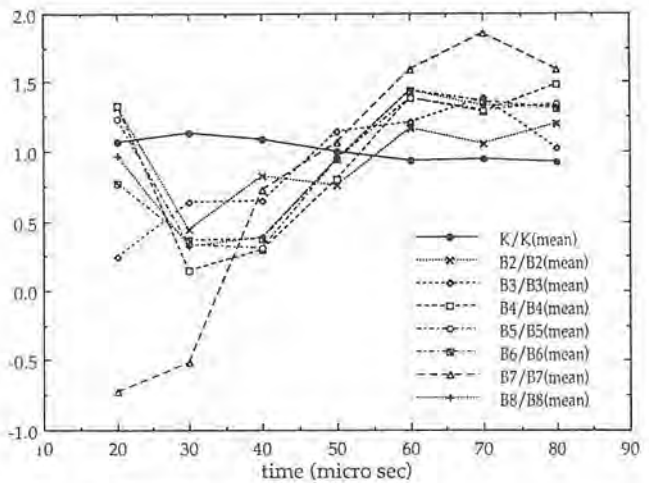

Figure 10.39. Time histories of $K_I^q(t)$ and $\beta_\kappa(t)$, each normalized by its mean value, for the duration of a particular crack propagation event. (Crack growth in PMMA.)

(22). It should be recalled that this conjuncture was made without proof in Secs. A.4 and A.5 of the first part of this chapter.

B.5.2 Synthetic Caustics for Transient Crack Growth

In order to demonstrate the above conjuncture conclusively and to directly illustrate the inadequacy of the classical analysis of caustics for investigating truly transient crack growth phenomena, the following procedure is adopted.

From the multiparameter analysis of the $[\partial(\hat{\sigma}_{11} + \hat{\sigma}_{22})/\partial x_1]$ patterns obtained using CGS in transmission (described in the previous section), one can obtain K_I^d, β_1, β_2, β_3, ... Once these constants are determined, $\partial(\hat{\sigma}_{11} + \hat{\sigma}_{22})/\partial x_2$ can be calculated using the expression for $(\hat{\sigma}_{11} + \hat{\sigma}_{22})$. Now, let us recall that the caustic mapping in transmission is given by

$$X_\alpha = X_\alpha + z_0 \left(c_\sigma h \frac{\partial}{\partial x_\alpha} (\hat{\sigma}_{11} + \hat{\sigma}_{22}) \right), \qquad \alpha = 1, 2,$$

where (X_1, X_2) denote the in-plane coordinates of the caustic plane, "screen," located at a distance z_0 from the specimen plane (x_1, x_2) along the optical axis. Using the above mapping, caustics have been generated from the CGS fringe patterns. One such caustic for a time instant 20 μs after crack initiation is shown in Fig. 10.40. The image plane distance (z_0 = 6 m) is such that the initial curve radius is well outside the crack-tip 3D region ($r_0 \geq 0.4h$). If one were to synthetically plot the caustic based only on the value of K_I^d (determined from the same multiparameter transient fit to the CGS pattern), the caustic should look like the one shown by the broken line.

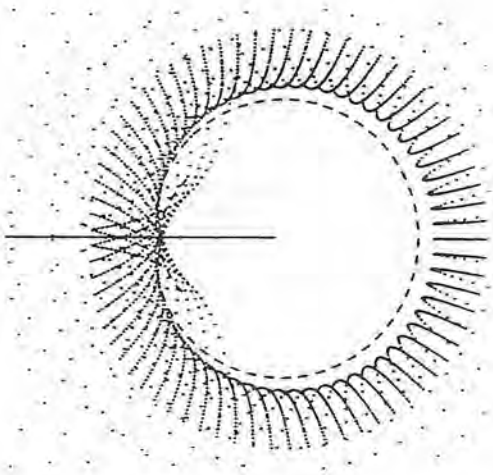

Figure 10.40. Synthetic caustic obtained by analyzing transmission CGS pattern for a time instant 20 μs after crack initiation. Dotted line corresponds to caustic obtained on the basis of K_I^s dominance at the same time instant.

This clearly demonstrates the effect of transient higher-order terms on the diameter of the caustic. The effect in the computed value of K_I^d is expected to be even more pronounced. Indeed, if the synthetic caustic is now interpreted in the classical way, as if it were generated by a K_I^d field [see Eq. (27)], the resulting value is found to be 25–30% higher than the value of K_I^d obtained from the full field measurements which were input in the numerical calculation. To demonstrate this clearly, the value of $K_I^d(t)$ measured from the full field CGS patterns, using the transient higher-order fit, for different times after crack initiation are plotted in Fig. 10.41. Also in the same plot, values of K_I^d caustic obtained by interpreting the synthetic caustic (generated form the experimental field measurements) in the classical manner are displayed. The figure clearly shows a persistent difference of the order discussed above which is due to the violation of the assumption of strict K_I^d dominance during transient crack growth.

Indeed this is consistent with the results of the bifocal caustics experiments presented in Sec. A.4, where pairs of caustics simultaneously generated from different distances from the crack-tip, during crack growth, and analyzed in the conventional way also resulted in differences in K_I^d of the same order of magnitude.

A visual illustration of the effects of transients on the shape of the caustic is shown in Fig. 10.42. Here a crack is propagating dynamically in a wedge loaded, "narrow," double cantilever beam specimens which acts as a waveguide. As the crack initiates unloading waves, visible as bright lines, are generated (first two frames). The waves are reflected from the specimen sides and interact with the propagating crack-tip distorting the caustic shape (third to seventh frames). After this time multiple wave reflections help cre-

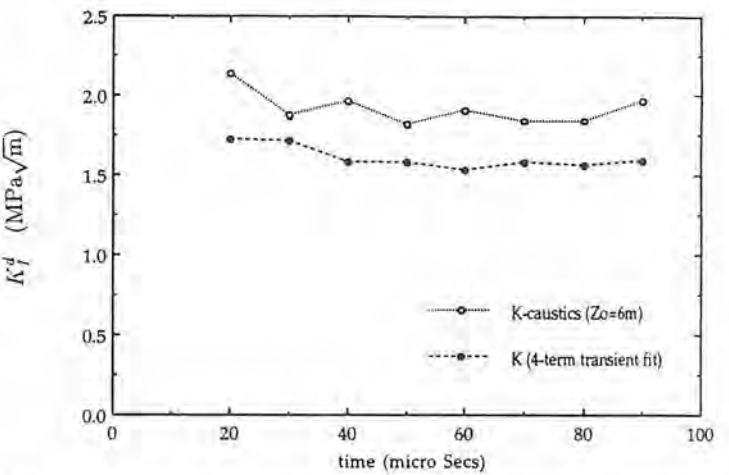

Figure 10.41. Plot of K_I^d caustics and CGS at different times during crack growth in PMMA. (Range of r_w/h for K_I^d caustic: 0.90–1.04.)

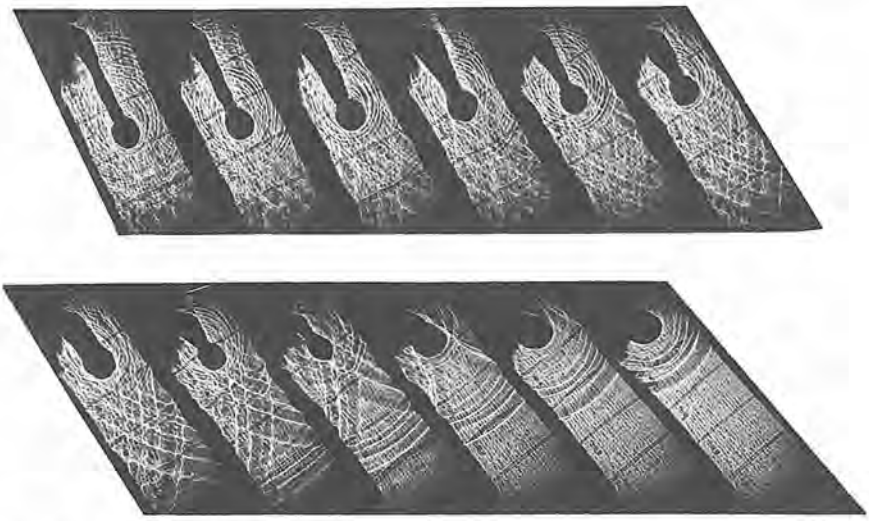

Figure 10.42. Effect of wave reflections on caustic shape. A visual demonstration of the destructive of K_I^d dominance by transients. Material: AISI-4340 steel, specimen: double cantilever beam.

ate a less transient environment in the specimen and the caustic curve attains a shape more closely resembling that predicted by K_I^d-dominant analysis. Although the above example is clearly *extreme* compared to crack growth in a large three-point-bend specimen where wave reflections are not so important, it helps visualize the effect of transients in destroying K_I^d dominance.

The experimental results obtained both by means of caustics and CGS lead us to the following general conclusion regarding experimental dynamic crack growth studies.

"Contrary to conventional wisdom, K_I^d dominance in the vicinity of dynamically propagating crack-tips appears to be the exception rather than the rule. It is thus critically important that interpretation of the experimental data under assumed K_I^d dominance, steady-state or two-dimensional conditions be *carefully justified* prior to attributing physical credence to the observed phenomena."

This observation may have important consequences in resolving a number of controversies that have arisen in experimental dynamic fracture studies of the recent past. In particular this realization may be relevant in the resolution of the debate concerning the existence of a unique relation between dynamic fracture toughness and crack-tip velocity, (uniqueness of the K_I^d versus v relation). The relevant literature on this controversy includes contributions by Kobayashi and Dally [81], Kalthoff [16,17], Rosakis, Duffy, and Freund [32], Zehnder and Rosakis [35], Ravi-Chandar and Knauss [26], Nigam and Shukla [51], Takahashi and Arakawa [82], Chona, Irwin, and

Sanford [83], and Dally, Agarwal, and Sanford [46] among others. For a discussion regarding these issues see Freund and Rosakis [46].

B.6 Applications of CGS in the Investigation of Asymmetric Dynamic Fracture Problems

B.6.1 Asymmetric Impact Loading of Stationary Cracks

In this section we briefly discuss the application of CGS to the investigation of asymmetric crack problems. For these cases the analysis of CGS patterns proceeds much in the same way as in the Mode-I (symmetric) case. The simplest assumption required for the analysis of CGS fringes is that of mixed-mode **K** dominance ($\mathbf{K} = K_{\mathrm{I}} + iK_{\mathrm{II}}$). As in the purely Mode-I case, here also, the presence of near-tip three dimensionality is expected to limit

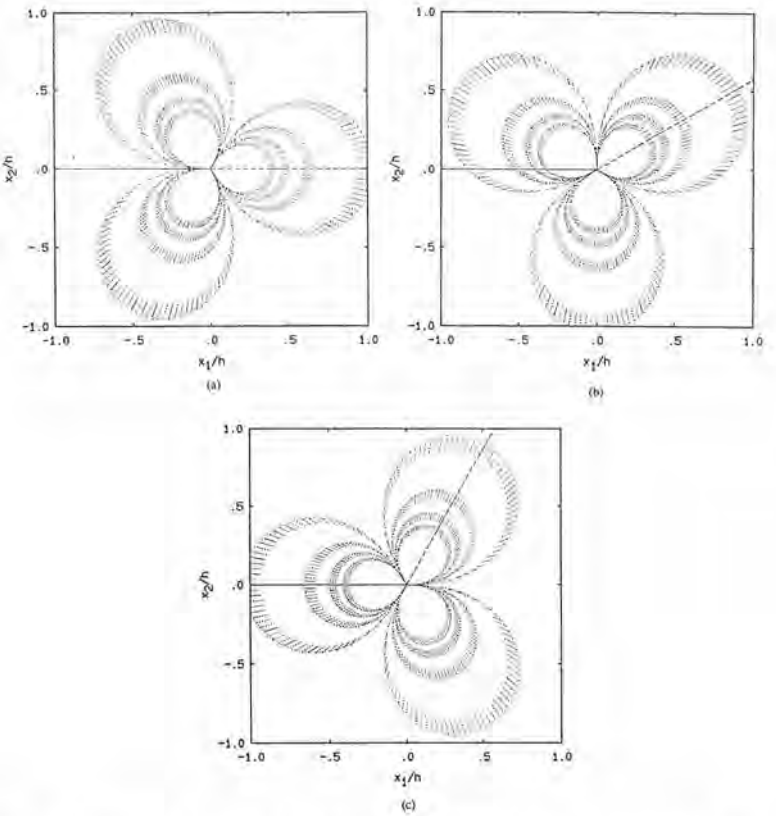

Figure 10.43. (a)–(c) Numerical predictions of CGS fringes [constant $\partial(\tilde{\sigma}_{11} + \tilde{\sigma}_{22})/\partial x_1$ values] constructed on the basis of (a) a pure K_{I} field, (b) $K_{\mathrm{I}} = K_{\mathrm{II}}$, and (c) a pure K_{II} field.

the validity of this assumption. In addition, the shape of the near-tip three-dimensional zone is expected to depend on the mixity (ratio of K_I/K_{II}).

An example of synthetically constructed $(\partial/\partial x_1)(\hat{\sigma}_{11} + \hat{\sigma}_{22})$ CGS patterns corresponding to three **K**-dominant fields of three different mixities is shown in Figs. 10.43(a)–43(c). The x_1 axis lies along the crack line.

Figure 10.43(a) corresponds to $K_I > 0$, $K_{II} = 0^+$, Fig. 10.43(b) corresponds to $K_I > 0$, and Fig. 10.43(c) corresponds to $K_I = 0^+$, $K_{II} > 0$. It is interesting to see that, much like caustics, CGS patterns corresponding to **K**-dominant fields retain their shape for different ratios of K_I/K_{II} but are simply rotated by an angle Ψ measured from the x_1 axis equal to

$$\Psi = \frac{\pi}{3} - \frac{2}{3}\tan^{-1}(K_I/K_{II}).$$

Thus, Figs. 10.43(a), 10.43(b), and 10.43(c) correspond to $\Psi = 0°$, 30°, and 60°, respectively.

A mixed-mode caustic pattern is shown in Fig. 10.44 for comparison to mixed-mode CGS patterns. The caustic pattern is obtained by reflection of laser light from the surface of a PMMA specimen containing a premachined crack in the shape of a circular arc (see Rosakis [27]). As discussed by Theocaris and Gdoutos [6] and by Rosakis [27], a finite K_{II} rotates the axis of symmetry of the "epicycloidal" caustic curve by an angle of $w = \tan^{-1}(K_{II}/K_I)$ to the local tangent at the crack-tip. Very much like CGS, the angle of

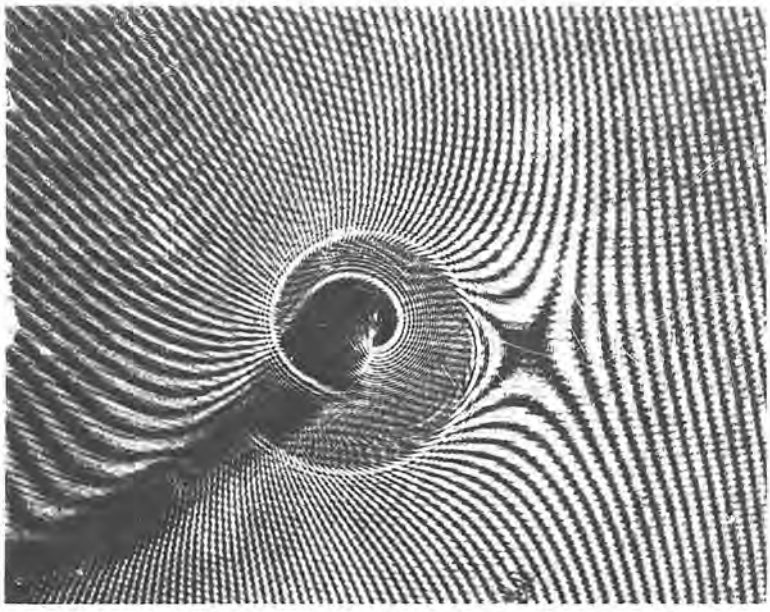

Figure 10.44. Mixed-mode caustic pattern at the tip of a circular arc crack loaded in the vertical direction.

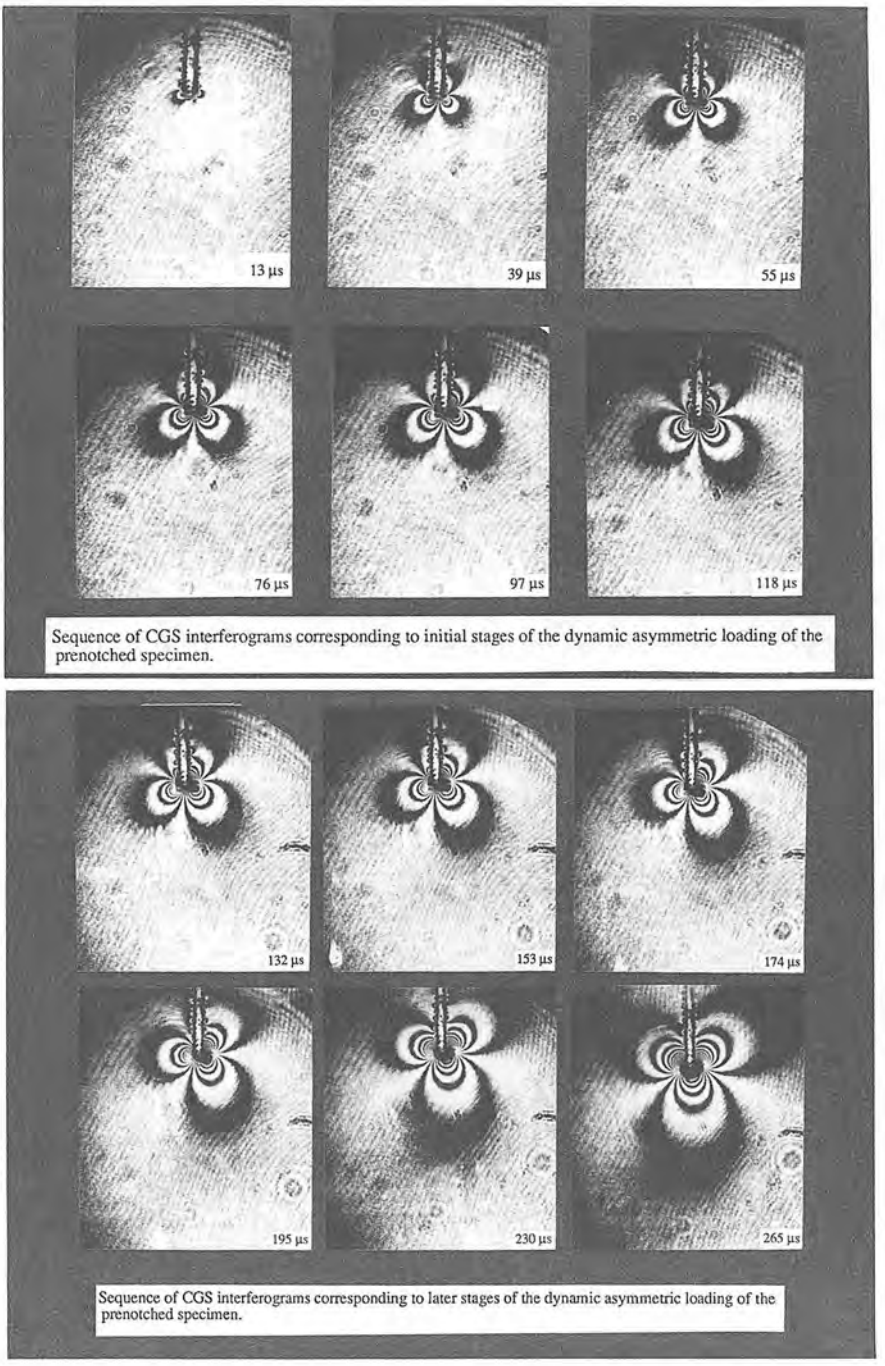

Figure 10.45. (a),(b) Sequence of CGS interferograms corresponding to asymmetric impact loading of a prenotched specimen. (a) Short time response. (b) Long time response.

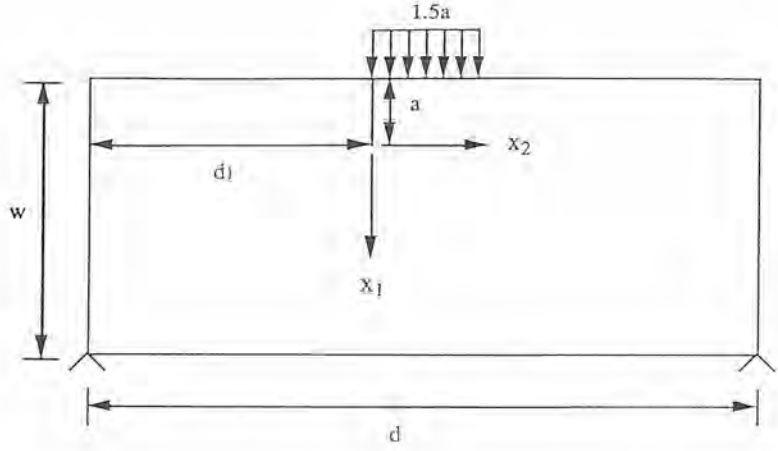

Dimensions of specimen :
a=25mm
w=127mm
d=254mm
d_1=136mm
thickness=7.5mm

Mechanical properties of specimen:
E=1240 MPa
v=0.35
c=0.108 nPa
$c_d^{pl\text{-}\sigma}$=1765 m/s

Figure 10.46. The asymmetric impact loading configuration and material constants.

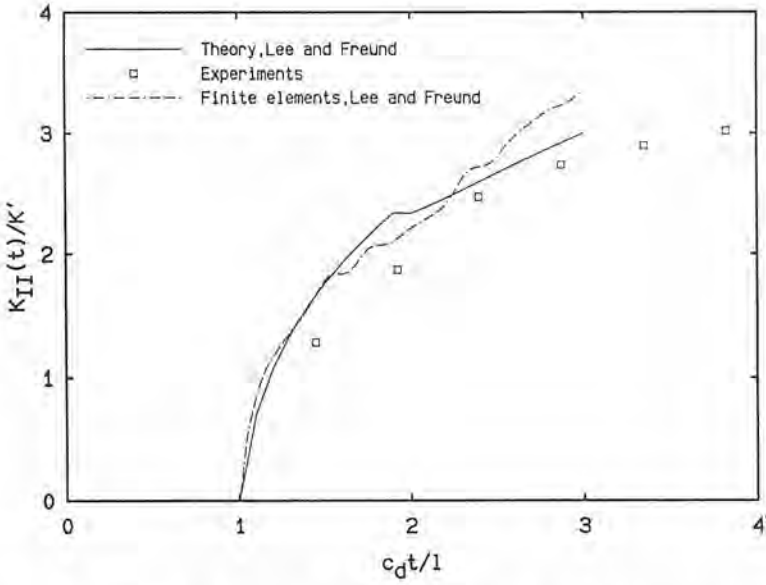

Figure 10.47. Normalized stress intensity factor as a function of normalized time, for "short" times (c_1t/l) < 3. Comparison or theoretical analysis of Lee and Freund [86], numerical analysis of Lee and Freund [87] and experimental results for Mode II.

the rotation of the axis of symmetry provides an easy measure of the ratio K_{II}/K_I.

Figures 10.45(a) and 10.45(b) show a series of CGS interferograms obtained by means of high-speed photography. The patterns are contours of equal $(\partial/\partial x_1)(\hat{\sigma}_{11} + \hat{\sigma}_{22})$, where x_1 is along the initial crack line. The specimen geometry and loading is shown in Fig. 10.46. The material is PMMA. The specimen is subjected to assymetric impact loading at one side of the initial crack. The loading is provided by means of a 24 foot drop weight tower. Figure 10.45(a) corresponds to short times after impact while Fig. 10.45(b) shows the long time response. For details see Mason, Lambros, and Rosakis [85].

As is obvious from a comparison of Figs. 10.45(a) and 10.43(c), at short times the near-tip deformations are primarily mode II. At longer times and as stress wave reflections start arriving from the supports the near-tip fields change to an almost Mode-I stress field [see Figs. 10.45(b) and 10.43(a)]. The accuracy with which these CGS patterns can be analyzed were the subject of the investigation cited above. It is shown that the time history of K_I and K_{II} obtained experimentally agrees very will with the predictions made by Lee and Freund [86,87], who modeled the same problem analytically and numerically. This was found to be true even at very short times after impact when K_I was only a small fraction of K_{II}. Fig. 10.47 shows the time history of stress intensity factors K_{II} as obtained experimentally (CGS) analytically and numerically.

B.6.2 Dynamic Crack Growth in Bimaterial Interfaces

The last dynamic application of CGS to be discussed here is that of a crack initiating and propagating quasistatically or dynamically in a bimaterial interface.

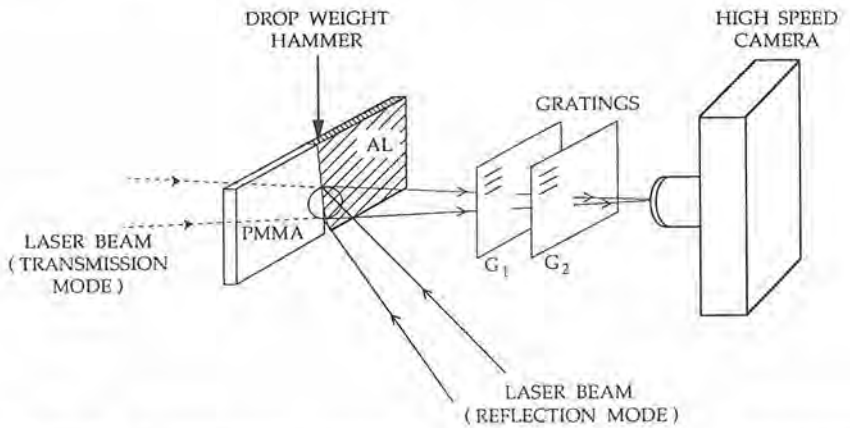

Figure 10.48. Experimental arrangements for dynamic crack growth in bimaterial interfaces.

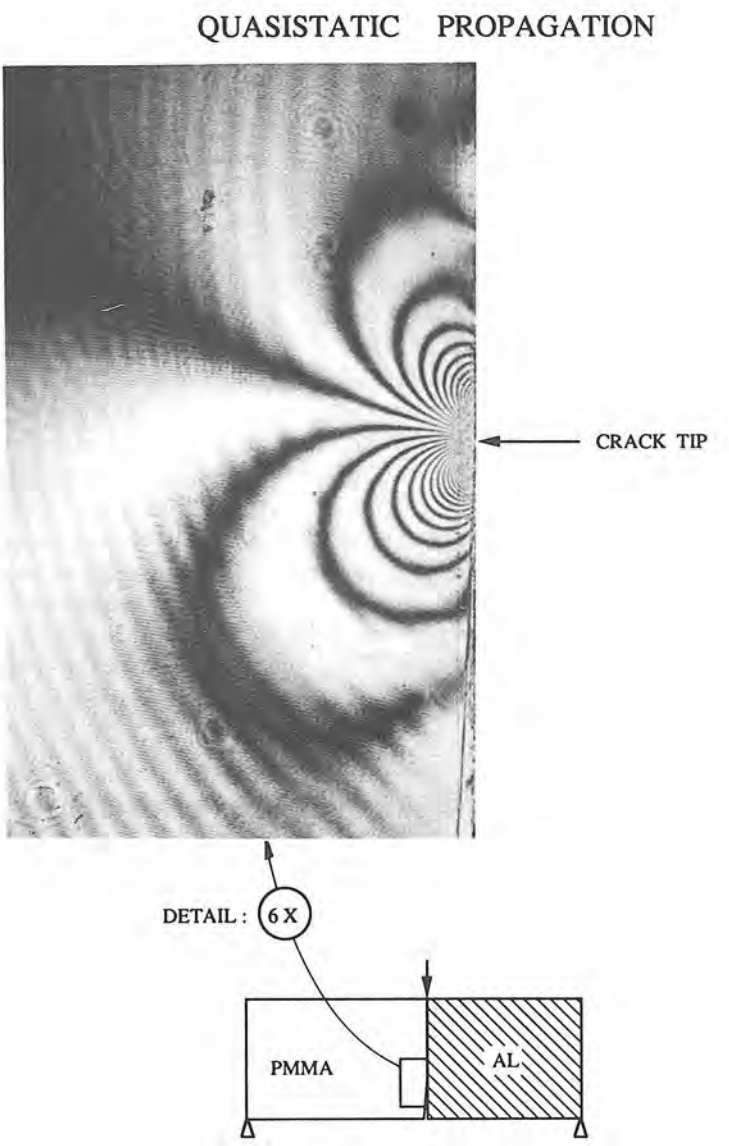

Figure 10.49. A CGS interferogram obtained by transmission of light from the near-tip region of a crack propagating quasistatically from a PMMA-Al interface.

The specimen configuration is of the three-point-bend type and is shown in Fig. 10.48. The bimaterial combination is that of Al and PMMA. Initial cracks exist on the bottom of the specimen along the bond line. In the dynamic experiments the specimen was impact loaded by means of a drop weight tower.

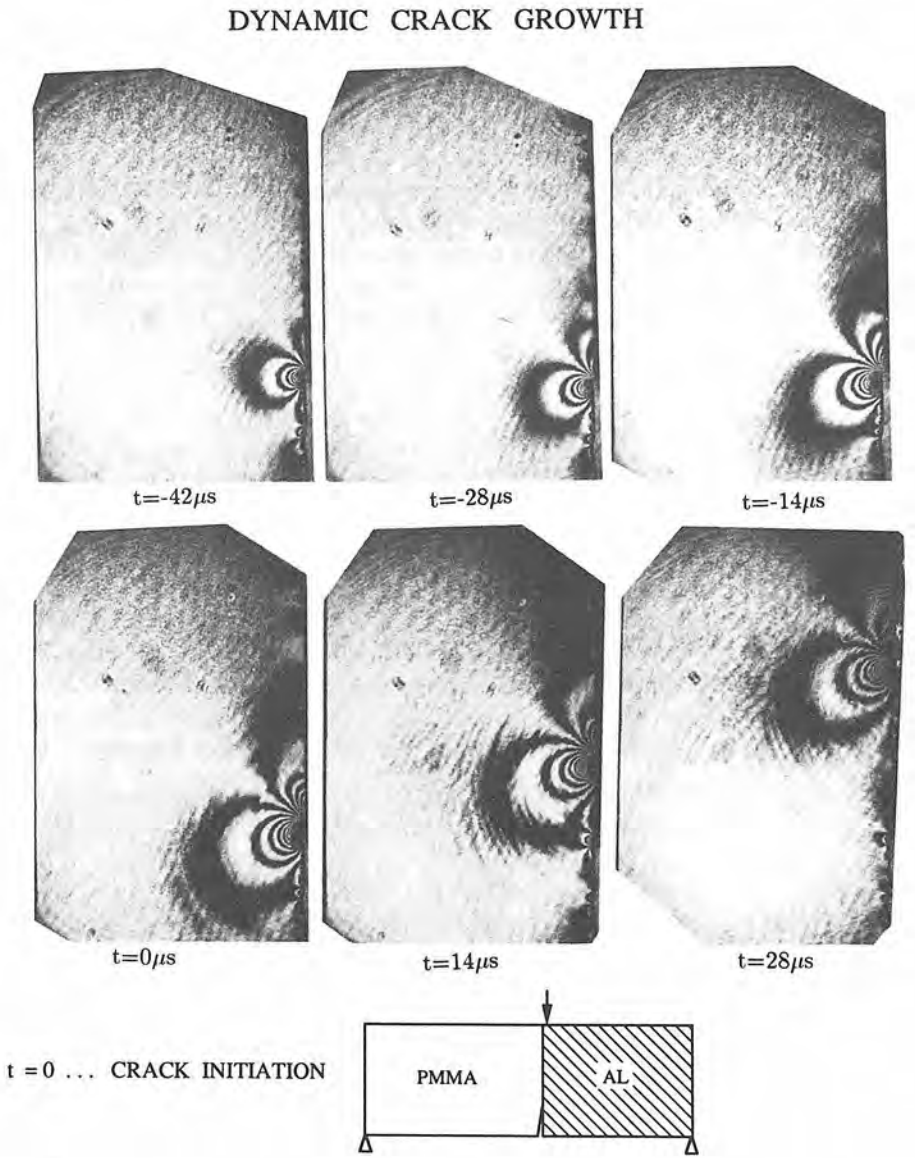

Figure 10.50. Dynamic crack growth in a PMMA-Al interface. (Average crack growth speed ~90% of Rayleigh wave speed of PMMA.)

Figure 10.49 shows a CGS interferogram corresponding to slow crack growth along the interface. The pattern is obtained by transmission of light through the PMMA side of the quasistatically loaded specimen. The slight asymmetry of the pattern reveals the existence of a small Mode-II component of the complex stress intensity factor. The object of this study, reported by Tippur and Rosakis [88], was to investigate quasistatic crack initiation and growth criteria under a variety of far field loading condition.

Figure 10.50 shows a series of high-speed photographs corresponding to dynamic crack growth along the bimaterial interface. The specimen was impact loaded on the aluminum side. Tippur and Rosakis [88] report crack growth velocities of the order of 80–90% of the shear wave speed of PMMA, a fact that suggest that the process is highly *dynamic*. Measured crack-tip velocity histories also show high acceleration regions, a fact that suggests that the process is also highly *transient*. (For discussion of transient effects, see Sec. B.5). The purpose of this continuing investigation is the study of dynamic fracture criteria in bimaterial interfaces. Points of interest include the investigation of the dependence of dynamic energy release rate on crack-tip velocity and phase angle $\Psi = \tan^{-1}(K_{II}/K_I)$.

B.7 Conclusions (CGS)

The main points discussed in this section are summarized as follows.

1. A shearing interferometric technique (CGS) bearing strong resemblance to optical caustics (both sensitive to gradients of stress), is presented as a viable alternative to current methods in the experimental study of dynamic crack propagation. CGS is a full field technique that can be used in a reflection mode for opaque materials, and can also be used in a transmission mode for optically *isotropic* transparent materials. Important advantages of this technique over other experimental methods used in dynamic fracture are related to the fact that CGS is a full field method and also that it has *variable sensitivity*. Its potential as a tool of investigating dynamic fracture problems in opaque solids is also of significance.
2. Results from dynamic crack propagation in PMMA and AISI 4340 steel specimens show that interpretation of experimental data on the basis of near-tip K_I^d dominance could lead to substantial errors in the measurement of the dynamic stress intensity factor. These are due to both the existence of a near-tip three-dimensional region as well as the existence of higher-order transient effects in the two-dimensional plane stress region surrounding the 3D zone.
3. It is further shown that a consistent interpretation of experimental data obtained from the two-dimensional region is possible using a higher-order analytical description of the transient crack-tip fields.

4. Potential new uses of the technique are discussed. These include the investigation of mixed-mode dynamic fracture problems as well as problems related to dynamic crack initiation and growth in bimaterial interfaces and composite structures.

Acknowledgments

This chapter summarizes work performed over a span of 15 years at Brown University and at Caltech by my research colleagues and myself. This work investigates the accuracy and suitability of optical techniques applied to the investigation of fracture problems. Particular attention is paid to dynamic fracture studies. Here I would like to acknowledge the very important contributions of my collaborators throughout this period. In particular, special thanks are due to my Ph.D. advisors, Professors J. Duffy and L.B. Freund at Brown University for introducing me to the subject of dynamic fracture mechanics. For later years I would like to acknowledge the help and contributions of faculty colleagues and past members of my research team at Caltech. These include Professors W.G. Knauss and G. Ravichandran of Caltech, K. Ravi Chandar of the University of Houston, A.T. Zehnder of Cornell University, R. Narasimhan of the Indian Institute of Science, Bangalore, S. Krishnaswamy of Northwestern University, and H. Tippur of Auburn University as well as my current graduate students, J. Lambros, J. Mason, C. Liu, and H. Bruck. Finally I would like to acknowledge with special emphasis the sustained encouragement cooperation and motivation provided Professor L.B. Freund through these years.

The work performed at Caltech has been almost exclusively supported by two funding agencies. First, I would like to acknowledge the continuous support of the Office of Naval Research through ONR Grant No. N00014-90-J-1340 (Dr. Y. Rajapaske, Program Monitor). Also the support of the National Science Foundation through the Presidential Young Investigator Award (Grant No. MSM-84-51204) is gratefully acknowledged. Finally, I am thankful for the support provided by Dr. M. Kanninen of the Southwest Research Institute through a subcontract for the academic year 1987–1988.

References

1. Manogg, P., "Anwendung der Schattenoptik zur Untersuchung des Zerreissvorgangs von Platten," Dissertation, Freiburg, Germany (1964).

2. Manogg, P., "Schattenoptische Messung der spezifischen Bruchenergie wahrend des Bruchvorgangs bei Plexiglas," in *Proceedings of the International Conference on the Physics of Non-Crystalline Solids*, Delft, The Netherlands (1964), pp. 481–490.

3. Theocaris, P.S., "Local Yielding Around a Crack Tip in Plexiglass," *J. Appl. Mech.* Vol. 37, 409–415 (1970).

4. Theocaris, P.S. and Ioakimides, N., "Some Properties of Generalized Epicycloids Applied to Fracture Mechanics," *J. Appl. Mech.* Vol. 22, 876–890 (1971).

5. Theocaris, P.S., "Reflected Shadow Method for the Study of Constrained Zones in Cracked Plates," *Appl. Opt.* Vol. 10, 2240–2247 (1971).

6. Theocaris, P.S. and Gdoutos, E., "An Optical Method for Determining Opening-Mode and Edge Sliding-Mode Stress-Intensity Factors," *J. Appl. Mech.* Vol. 39, 91–97 (1972).

7. Theocaris, P.S., "Elastic Stress Intensity Factors Evaluated by Caustics," *Mechanics of Fracture*, Vol. VII, edited by G.C. Sih, (Sijthoff and Noordhoff, Roc Alphen aan den Rijn, The Netherlands (1981).

8. Theocaris, P.S. and Stassinakis, C.A., "Experimental Solution of the Problem of a Curvilinear Crack in Bonded Dissimilar Materials," *Int. J. Fract.* Vol. 13, 13–26 (1977).

9. Theocaris, P.S., "The Reflected Caustic Method for the Evaluation of Mode III Stress Intensity Factors," *Int. J. Mech. Sci.* Vol. 23, 105–117 (1981).

10. Theocaris, P.S. and Gdoutos, E.E., "The Modified Dugdale-Barenblatt Model Adapted to Various Fracture Configurations in Metals," *Int. J. Fract.* Vol. 19, 549–564 (1974).

11. Katsamanis, F., Raftopoulos, D., and Theocaris, P.S., "The Dependence of Crack Velocity on the Critical Stress in Fracture," *Exp. Mech.* Vol. 17, 128–132 (1977).

12. Kalthoff, J.F., Beiniert, J., and Winkler, S., "Analysis of Fast Running and Arresting Cracks by the Shadow-Optical Method of Caustics," in *Int. Union Th. and App. Mech. (IUTAM) Symposium on Optical Methods Mech. Solids*, University of Poitiers, France, Sept. 10–14, 1979, edited by A. Lagarde (Sijthoff-Noordhoff, Alphen aan den Rijn, The Netherlands, 1980), pp. 497–508.

13. Beinert, J. and Kalthoff, J.F., "Experimental Determination of Dynamic Stress Intensity Factors by Shadow Patterns," *Mechanics of Fracture*, Vol. 7 of *Experimental Fracture Mechanics*, edited by G.C. Sih (Martinus Nijhoff Publishers, Hingham, MA, 1981), pp. 280–330.

14. Kalthoff, J.F., "Stress Intensity Factor Determination by Caustics," in *Proceedings of the International Conference on Experimental Stress Analysis*, organized by Japan Society of Mechanical Engineers (JSME) and American Society for Experimental Stress Analysis (SESA), Honolulu-Maui, Hawaii, May 23–29, (1982), Bethel, CT. pp. 1119–1126.

15. Kalthoff, J.F., Bohme, W., and Winkler, S., "Analysis of Impact Fracture Phenomena by Means of the Shadow Optical Method of Caustics," in *Proceedings of the 7th International Conference on Exp. Stress Analysis* organized by SESA, Haifa, Israel, 23–27, (1982), pp. 148–160.

16. Kalthoff, J.F., "On Some Current Problems in Experimental Fracture Dynamics," in *Workshop on Dynamic Fracture*, edited by W.G. Knauss, A.J. Rosakis, and K. Ravi-Chandar, California Institute of Technology, Pasadena, CA, Feb. 17–18, (1983), pp. 11–35.

17. Beinert, J. and Kalthoff, J.F., "Experimental Determination of Dynamic Stress Intensity Factors by Shadow Patterns," *Mechanics of Fracture*, Vol. VII, edited by G.C. Sih (Sijthoff and Noordhoff, Alphen aan den Rijn, The Netherlands (1981).

18. Kalthoff, J.F. "Shadow Optical Methods of Caustics," in *Handbook on Experimental Mechanics*, edited by A.S. Kobayashi, (1987) McGraw Hill Publishers, N.Y., N.Y. Chap. 9, pp. 430–498.

19. Rossmanith, H.P., "Method of Caustics for Static Plane Elasticity Problems," *J. Elast.*, Vol. 12, 193–200 (1982).

20. Rossmanith, H.P., "General Mode-I Caustic Evaluation for Optically Anisotropic Materials," *Ing. Arch.* Vol. 50, 73–83 (1981).

21. Rossmanith, H.P., "Method of Caustics for Mixed-Mode Crack Loading with Higher Order Term Effects," *Eng. Fract. Mech.* Vol. 13, 991–1000 (1980).

22. Rossmanith, H.P., "Determination of Stress Intensity Factors by the Dynamic Method of Caustics for Optically Isotropic Materials," *Ing. Arch.* Vol. 48, 363–381 (1979).

23. Rossmanith, H.P., "Influence of Geometrical Imperfections in the Method of Caustics," *Eng. Fract. Mech.*, Vol. 18, 903–908 (1983).

24. Rossmanith, H.P., "The Caustic Approach to Rayleigh-Waves and their Interaction with Surfact Irregularities," *Opt. Lasers Eng.* Special Issue on Caustics (A.J. Rosakis, Guest Editor) Vol. 14, no. 2 (1990).

25. Zhang, Y. and Ravi-Chandar, K. "Application of the Method of Caustics under Mixed-Mode Loading in Elasto-Plastic Materials," *Opt. Lasers Eng.*, Special Issue on the Optical Method of Caustics (A.J. Rosakis, Guest Editor), Vol. 14, 71–83 (1991).

26. Ravi-Chandar, K. and Knauss, W.G., "On the Characterization of the Transient Stress Fields Near the Tip of a Crack," *J. Appl. Mech.* Vol. 54, 72–78 (1987).

27. Rosakis, A.J., "Determination of Stress Intensity Factors at an Arched Crack Tip by the Method of Caustics," *Strain* Vol. 15, 79–97 (1979).

28. Rosakis, A.J., "Analysis of the Optical Method of Caustics for Dynamic Crack Propagation," *Eng. Fract. Mech.* Vol. 13, 331–347 (1980).

29. Rosakis, A.J., "Experimental Determination of Fracture Initiation and Dynamic Crack Propagation Resistance of Structural Steels by Optical Method of Caustics," Ph.D. thesis, Brown University, June (1982).

30. Rosakis, A.J. and Freund, L.B., "Optical Measuring of the Plastic Strain Concentration at a Tip in a Ductile Steel Plate," *J. Eng. Mater. Tech.* Vol. 104, 115–125 (1982).

31. Rosakis, A.J., Ma, C.C., and Freund, L.B., "Analysis of the Optical Shadow Spot Method for a Tensile Crack in a Power-Law Hardening Material," *J. Appl. Mech.* Vol. 50, 777–782.

32. Rosakis, A.J., Duffy, J., and Freund, L.B., "The Determination of the Dynamic Fracture Toughness of AISI 4340 Steel by the Shadow Spot Method," *J. Mech. Phys. Solids* Vol. 34, No. 4, 443–460 (1984).

33. Rosakis, A.J. and Zehnder, A.T., "On the Method of Caustics: An Exact Analysis Based on Geometrical Optics," *J. Elasticity* Vol. 4, 347–367 (1985).

34. Rosakis, A.J. and Ravi-Chandar, K., "On the Crack Tip Stress State: An Experimental Evaluation of Three-Dimensional Effects," *Int. J. Solids Struct.* Vol. 22, No. 2, 121–134 (1986).

35. Zehnder, A.T. and Rosakis, A.J., "Dynamic Fracture Initiation and Propagation in 4340 Steel Under Impact Loading," *Int. J. Fract.* Vol. 43, 271–285 (1990).

36. Krishnaswamy, S. and Rosakis, A.J., "On the Extent of Dominance of Asymptotic Elastodynamic Crack-Tip Fields; Part I: An Experimental Study Using Bifocal Caustics," *J. Appl. Mech.* Vol. 58, No. 1, 87–94 (1990).

37. Krishnaswamy, S., Rosakis, A.J., and Ravichandran, G., "On the Extent of Dominance of Asymptotic Elastodynamic Crack-Tip Fields; Part II: A Numerical Investigation of

Three-Dimensional and Transient Effects," *J. Appl. Mech.* Vol. 58, No. 1, 95–103 (1991).

38. Rosakis, A.J., Krishnaswamy, S., and Tippur, H.V., "On the Application of the Optical Method of Caustics to the Investigation of Transient Elastodynamic Crack Problems: Limitations of the Classical Interpretation," *J. Opt. Lasers Eng.* Special issue on Caustics (A.J. Rosakis, Guest Editor), Vol. 13, 183–210 (1990).

39. *J. Opt. Lasers Eng.* Special Issue on Caustics (A.J. Rosakis, Guest Editor), Vol. 13 (1990).

40. Kamath, S.M. and Kim, K.S., "Coherent-Light Shadow Spot of a Crack Under Mode-I Loading: Theory and Experiment," *Exp. Mech.* Vol. 26, no. 4, 386–393 (1986).

41. Rosakis, A.J., Zehnder, A.T., and Narasimhan, R., "Caustics by Reflection and their Application to Dynamic and Elastic-Plastic Fracture Mechanics," *Opt. Laser Eng.* Vol. 27, No. 8, 596–610 (1988).

42. Narasimhan, R. and Rosakis, A.J., "Three-Dimensional Effects Near a Crack Tip in a Ductile Three Point Bend Specimen, Part I: Numerical Investigations," *J. Appl. Mech.* Vol. 57, 607–617 (1990).

43. Freund, L.B. and Clifton, R.J., "On the Uniqueness of Plane Elasto-Dynamic Solutions for Running Cracks," *J. Elastic.* Vol. 4, 293–299 (1974).

44. Freund, L.B., *Dynamic Fracture Mechanics* (Cambridge University Press, Cambridge, MA, 1990).

45. Smith, R.H. and Freund, L.B., "Three-Dimensional Finite Element Analysis of Steady Elastodynamic Crack Growth in a Plate,"*J. Opt. Lasers Eng.* Special Issue on the Optical Method of Caustics (A.J. Rosakis, Guest Editor) Vol. 14, no. 2, pp 81–101 (1990).

46. Freund, L.B. and Rosakis, A.J., "The Structure of the Near Tip Field Solution During Transient Elastodynamic Crack Growth," *J. Mech. Phy. Solids*, Vol. 40, no. 3, pp 699–719, 1992.

47. Rosakis, A.J., Liu, C., and Freund, L.B., "A Note on the Asymptotic Stress Field of a Non-Uniformly Propagating Dynamic Crack," *Int. J. Fract.* Vol. 50, R39–R45 (1991); California Institute of Technology GALCIT Report No. SM90-27 (1990).

48. Krishnaswamy, S., Tippur, H.V., and Rosakis, A.J., "Measurement of Transient Crack Tip Deformation Fields Using the Method of Coherent Gradient Sensing," *J. Mech. Phys. Solids.* Vol. 40, No. 2, 339ff. (1992); California Institute of Technology GALCIT Report No. SM 90-1.

49. Ma, C.C. and Freund, L.B., "The Extent of the Stress Intensity Factor Field During Crack Growth Under Dynamic Loading Conditions," *ASME J. Appl. Mech.* Vol. 53, 303–310 (1986).

50. Ma, C.C., "The Influence of Singular Field Dominance on the Caustic Method," *Opt. Lasers Eng.*, Special Issue on the Optical Method of Caustics, (A.J. Rosakis, Guest Editor), Vol. 13, no. 3–4, pp. 279–304 (1990).

51. Nigam, H. and Shukla, A., "Comparison of the Techniques of Transmitted Caustics and Photoelasticity as Applied to Fracture," *Exper. Mech.* Vol. 28, 123–133 (1988).

52. Dally, J.W., Fourney, W.G., and Irwin, G.R., "On the Uniqueness of K_{ID} – å Relation," *Int. J. Fract.* Vol. 27, 159–168 (1985).

53. Chona, R., Irwin, G.R., and Sanford, R.J., "Influence of Specimen Size and Shape on the Singularity-Dominated Zone," in *Fracture Mechanics: 14th Symposium-Volume I:*

Theory and Analysis, ASTM STP 791, edited by J.C. Lewis and G. Sines (American Society for Testing and Materials, Philadelphia, PA, 1983), pp. 1-3–1-23.

54. Sanford, R.J., and Chona, R., "Photoelastic Calibration of the Short-Bar Chevron-Notched Specimen," in *Chevron Notched Specimens: Testing and Stress Analysis* ASTM STP 855, edited by J.H. Underwood, S.W. Freiman, and F.I. Baratta (American Society for Testing and Materials, Philadelphia, PA, 1984), pp. 81–97.

55. Chona, R. and Sanford, R.J., "Analyzing Crack-Tip Isochromatic Fringe Patterns," in *Proceedings of the VI International Congress of Exper. Mech.*, June 6–10 (1988), pp. 751–760. Society for Exp. Mech. (SEM), Bethel, CT.

56. Shukla, A. and Chona, R., "The Stress Field Surrounding a Rapidly Propagating Curving Crack," in *Fracture Mechanics, 18th Symposium, ASTM STP 945*, edited by D.T. Read and R.P. Reed (American Society for Testing and Materials, Philadelphia, PA, 1988), pp. 86–99.

57. Liu, C., Rosakis, A.J., and Freund, L.B., "The Interpretation of Optical Caustics in the Presence of Non-Uniform Crack Tip Motion Histories: A Study Based on a Higher Order Transient Crack Tip Expansion," in press.

58. Hutchinson, J.W., "Singular Behavior at the End of a Tensile Crack," *J. Mech. Phys. Solids* Vol. 16, 13–31 (1968).

59. Rice, J.R. and Rosengren, G.F., "Plane Strain Deformation Near a Crack Tip in Power Law Hardening Materials," *J. Mech. Phys. Solids* Vol. 16, 1–12 (1968).

60. Shih, C.F., "Elastic-Plastic Analysis of Combined Mode Crack Problems," Ph.D. thesis, Harvard University (1973).

61. Marchand, A., Freund, L.B., Ma, C.C., and Duffy, J., "Use of the Shadow Spot Method in Evaluating *J* for Ductile Steels," Brown University Technical Report No. ONR 0597/1, MRLE-160 (1981).

62. Narasimhan, R. and Rosakis, A.J., "Numerical Study of Stationary Plane Stress Cracks in Elastic-Plastic, Power Hardening Solids," *J. Mech. Phys. Solids* Vol. 36, 77–117 (1988).

63. Zehnder, A.T., Rosakis, A.J., and Narasimhan, R., "Measurement of the J Integral with Caustics: An Experimental and Numerical Investigation," *ASTM-STP* 995, Special Volume on Non-linear Fracture Mechanics, pp 318–339 (1989) American Society for Testing and Materials (ASTM) Philadelphia, PA.

64. Judy, R.W. and Sanford, R.J., "Correlation of Optical Caustic Behavior with Fracture Properties of High Strength Steels," ASTM STP 995, in *Nonlinear Fracture Mechanics, Proceedings of the Third International Symposium on Nonlinear Fracture Mechanics*, Knoxville, Tenn., Oct. 6–8 (1986).

65. Zehnder, A.T. and Rosakis, A.J., "Three Dimensional Effects Near a Crack Tip in Ductile Three Point Bend Specimen, Part II: An Experimental Investigation using Interferometry and Caustics," *J. Appl. Mech.* Vol. 57, 618–626 (1990).

66. Zehnder, A.J., Rosakis, A.J., and Krishnaswamy, S., "Dynamic Measurement of the J-Integral in Ductile Metals: Comparison of Experimental and Numerical Techniques," *Int. J. Fract.*, Special Issue on Non-linear Fracture Mechanics (W.G. Knauss and A.J. Rosakis, Guest Editors), Vol. 42, No. 3, 209–230 (1990); *Proceedings of the Int. Union Theor. and App. Mech. (IUTAM) Symposium on Recent Advances on Non-linear Fracture Mechanics*, Caltech, March 14–16 (1988).

67. Chiang, F.P., in *Manual of Exper. Stress Analysis Tech.*, Chapter 6, edited by A. S. Kobayashi, SESA 3rd ed. (1978) Soc. Exp. Mech., Bethel, CT.

68. Glat, I. and Kafri, O., "Moire Deflectectmetry-Ray Tracing Interferometry," *Opt. Lasers Eng.* Vol. 8, 277–320 (1988).

69. Chiang, F.P. and Juang, R.M., "Laser Speckle Interferometry for Plate Bending Problems," *J. Appl. Opt.* Vol. 15, 2199–2204 (1976).

70. Patorski, K., "Conjugate Lateral Shear Interferometry and Its Implications," *J. Opt. Soc. Am.* Vol. A.3, 1862–1868 (1986).

71. Hung, Y.Y. and Durelli, A.J., "Simultaneous Measurement of Three Displacement Derivatives Using a Multiple Image-Shearing Interferometric Camera," *J. Strain Anal.* Vol. 14, No. 3, 81–88 (1979).

72. Chao, Y.J., Sutton, M.A., and Taylor, C.E., "Slope Measurement Using Multiplexed Diffraction Gratings as Shearing Conigratings in Interferometry," *Eng. Fract. Mech.* Vol. 23 No. 12, 370–378 (1984).

73. Sanford, R.J. and Dally, J.W., "A General Method for Determining Mixed-Mode Stress Intensity Factors from Isochromatic Fringe Patterns," *Eng. Fract. Mech.* Vol 11, 621–633 (1979).

74. Burger, C.P., "Photoelasticity" in *Handbook on Experimental Mechanics*, edited by A.S. Kobayashi, Chapter 5, pp. 162–281 (1987 McGraw Hill Publishers, N.Y., N.Y.).

75. Chiang, F.P. and Hareesh, T.V. "Three-Dimensional Crack Tip Deformation: An Experimental Study and Comparison to HRR Field," *Int. J. Fract.* Vol. 36, 243–257 (1988).

76. Kang, B.S.J., Kobayashi, A.S., and Post, D., "Stable Crack Growth in Aluminum Tensile Specimens," *Exper. Mech.* Vol. 27, No. 3, 243–245 (1987).

77. Kafri, O., "Noncoherent Method for Mapping Phase Objects," *Opt. Lett.* Vol. 5, 555–557 (1980).

78. Glatt, I. and Kafri, O., "Moire Deflectometry-Ray Tracing Interferometry," *Opt. Lasers Eng.* Vol. 8, 277–320 (1988).

79. Tippur, H.V., Krishnaswamy, S., and Rosakis, A.J., "A Coherent Gradient Sensor for Crack Tip Deformation Measurements: Analysis and Experimental Results," *Int. J. Fract.* Vol. 48, No. 1, 193–204 (1990).

80. Tippur, H.V., Krishnaswamy, S., and Rosakis, A.J., "Optical Mapping of Crack Tip Deformations Using the Method of Transmission and Reflection Coherent Gradient Sensing: A Study of Crack-Tip K-Dominance," Caltech Report No. SM89-11 (1989) *Int. J. Fract.*

81. Kobayashi, T. and Dally, J.W., "Crack Arrest Methodology and Applications," *ASTM STP 711*, (American Society for Testing and Materials, Philadelphia, PA, 1980), pp. 189–210.

82. Takahashi, K. and Arakawa, K., "Dependence of Crack Acceleration on the Dynamic Stress-Intensity Factor in Polymers," *Exper. Mech.* Vol. 27, No. 2, 195–200 (1987).

83. Chona, R., Irwin, G.R., and Sanford, R.J., "The Influence of a Specimen Size and Shape on the Singularity-Dominated Zone," in *Proceedings of the 14th National Symposium on Fracture Mechanics*, ASTM STP 791, (American Society for Testing and Materials, Philadelphia, PA, 1983), pp. 13–123.

84. Dally, J.W., Agarwal, R.K., and Sanford, R.J., "A Study of Hysteresis in the $K_{ID} - \dot{a}$ Relation," *Exper. Mech.* Vol. 30, no. 2, 177–183 (1990).

85. Mason, J.J., Lambros, J., and Rosakis, A.J., "On the Use of a Coherent Gradient Sensor in Dynamic Mixed-Mode Fracture Mechanics Experiments," *J. Mech. Phys. Solids*

Vol. 40, No. 3, 641–661 (1992); California Institute of Technology GALCIT Report No. SM 90-21 (1990).

86. Lee, Y.J. and Freund, L.B., "Fracture Initiation due to Asymmetric Loading of and Edge Cracked Plate," *J. Appl. Mech.* Vol. 57, 104–111 (1990).

87. Lee, Y.J. and Freund, L.B., private communication.

88. Tippur, H. and Rosakis, A.J., "Quasistatic and Dynamic Crack Growth Along Bimaterial Interfaces: A Note on Crack Tip Field Measurements Using Coherent Gradient Sensing," *J. Exper. Mech.* Vol. 31, No. 3, 243–251 (1991); California Institute of Technology GALCIT Report No. SM 90-18 (1990).